University of Cape Town
Faculty of Science
Department of Mathematics and Applied Mathematics

Chaotic behavior and energy polarisation in flatband lattice models

by

Su Ho Cheong
(CHNSUH001)

Supervisor: Associate Professor Haris Skokos
Co-supervisor: Dr Arnold Ngapasare

02/10/2023

University of Cape Town

The copyright of this thesis vests in the author. No quotation from it or information derived from it is to be published without full acknowledgement of the source. The thesis is to be used for private study or non-commercial research purposes only.

Published by the University of Cape Town (UCT) in terms of the non-exclusive license granted to UCT by the author.

University of Cape Town

Abstract

Flatbands (FBs) in lattice systems correspond to dispersionless energy bands created through what is called destructive interference, a phenomenon caused by the existence of lattice symmetries, resulting in compactly localised wave functions to just a few lattice sites. The existence of FBs in materials entails high sensitivity to the initial conditions of the system, especially with regard to disorder and nonlinearity. In this study, we numerically investigate the wave packet dynamics and chaotic behaviour of a simple tight-binding system exhibiting FBs, the so-called stub lattice model. Initially we show the existence of a FB and of two dispersive frequency bands for this model and identify three different dynamical regimes, namely the weak chaos, strong chaos, and self trapping regimes. Using symplectic integration techniques, we evolve in time, t, initially localised wave packets for these regimes and quantify their spreading through the computation of the wave packets second moment, m_2, while the extent of localisation is characterised using the wave packets participation number. We show that, for both the weak and strong chaos regimes, the spreading of wave packets, which is characterised by a power law increases of m_2 (respectively $\propto t^{0.33}$ and $\propto t^{0.5}$), is a chaotic process whose maximum Lyapunov exponent respectively decreases $\propto t^{-0.25}$ and $\propto t^{-0.3}$. By decreasing the system's disorder strength we alter the width of the bandgap, something which does not appear to affect the spreading dynamics in the weak chaos regime, while our results do not lead to clear conclusions in the case of strong chaos. Furthermore, we find that particular disorder configurations which preserve the FB do not alter the wave packet spreading dynamics for the weak chaos regime. Finally, we observe that the wave packets norm distributions at the subsites of the stub lattice unit cells reach equilibrium if the evolution time is sufficiently long.

Acknowledgments

I would first like to acknowledge Assoc. Prof. Haris Skokos and express my deepest gratitude for allowing me to obtain my MSc degree under his supervision. I want to thank him and co-supervisor Dr Arnold Ngapasare for their valuable input, time, guidance, and support throughout the duration of my MSc studies. I would like to also acknowledge and thank members of the Nonlinear Dynamics and Chaos Group (Dr Malcolm Hillebrand, Henok Moges, Sané Erasmus, Jean-Jacq du Plessis, Sebastian Zimper, and Dylan Theron) for their useful discussions as well as their valuable comments on the thesis. I want to thank the members of Laboratoire d'Acoustique de l'Université du Mans (LAUM), namely Prof. Olivier Richoux, Dr Georgios Theocharis, and Dr Vassos Achilleos for their scientific input and discussions. Additionally, I would also like to express my gratitude towards the Centre for High-Performance Computing (CHPC) facility for providing high-performance computing clusters for numerical computations. Finally, I want to thank the Education, Training and Development Practices Sector Education and Training Authority (ETDP SETA), National Research Foundation (NRF), and University of Cape Town Faculty of Science postgraduate scholarship for funding my studies.

List of abbreviations

AL: Anderson localisation

CHPC: Centre for High Performance Computing

CLS: compact localised states

DNLS: discrete nonlinear Schrödinger equation

DDNLS: disordered discrete nonlinear Schrödinger equation

dof: degrees of freedom

DVD: deviation vector distribution

EOM: equations of motion

FB: flatband

KG: Klein-Gordon

LCE: Lyapunov characteristic exponent

LHS: left hand side

LOWESS: locally weighted scatterplot smoothing

mLE: maximum Lyapunov exponent

RHS: right hand side

SI: symplectic integrators

1D: one-dimensional

Contents

Chapter 1

Introduction

Nonlinear lattices and their dynamics have been the focus of many research studies over the past three decades [1, 2, 3, 4, 5, 6, 7, 8, 9, 10]. For the bulk of these studies, fundamental lattice models such as the discrete Klein-Gordon (KG) model and the discrete nonlinear Schrödinger equation (DNLS) have been used to study various wave phenomena (see e.g., [11, 12, 13, 14, 15]). Despite the widespread use of these two lattices, the search for new frontiers to demonstrate interesting energy transport characteristics has been going on for decades and the so-called flatband (FB) networks have proved to be a viable option. FBs are dispersionless energy bands that arise from the so-called compact localised states (CLS) based on destructive interference and lattice symmetry. These FB networks are characterised by the co-existence of at least one flat and one dispersive band [16]. The lattice symmetry results in wave functions being compactly localised to a few number of lattice sites. Other forms of localised structures can be obtained using lattice models in condensed matter physics, where the eigenstates are localised due to disorder. This type of localisation is now a well-established phenomenon called Anderson localisation (AL) [17]. Other localised structures typically found on the edges of lattices gave rise to what is now known as topological waves [18, 19]. The first publications on FBs appeared in 1986 [20] and later studies expanded upon this idea in 1991 [21], to show that lattices of a certain type can have a high susceptibility to magnetism in their ground state if the lowest band structure is a FB. A couple of years later the same properties of magnetism related to FBs appeared in different lattices shown in the work done by Tasaki [22]. Soon after the first publications on FBs, many studies appeared in the literature on this topic (see e.g., [23, 24, 25, 26, 27, 28]), until the end of the last century, before the strong research interest began to wane. The past decade, however, has seen a strong revival of the research

community's interest in FBs, as evidenced by the numerous studies which have appeared in the literature (see e.g., [29, 30, 31, 32, 33]).

During the last decade, there has been a sustained interest on the topic of FBs, and tight-binding model-based configurations [34, 35, 36, 37] and mechanical lattices [38] have proved to be excellent testbeds to study wave-physics. Recently, experimental observations of FBs have been reported in optical [39] and photonic lattices [40, 41] as well as in electronic systems such as superconducting wire networks and nano-engineered atomic lattices on metallic surfaces [42, 43]. Other applications of FB models have been in photonic systems, specifically on the concept of slow light [44], which happens when light moves through a medium, a phenomenon which has applications in telecommunications and time-dependent systems that use optical signals.

FB lattices are known for their high sensitivity to initial conditions and parameters (as discussed in Sec. 2.4 of [45]), a property which results in the corresponding Hamiltonians being extremely sensitive as well. It is exactly this sensitivity that makes FBs rare in nature. The search for materials with FB properties is an important and attractive research field. Quite often such materials are manufactured [32, 46]. The sensitivity of these systems can result in quick changes in their properties. For example, the introduction of disorder can trigger the systems sensitivity, since the presence of disorder is inevitable in experimental setups involving FBs. Disorder can be introduced to materials during the manufacturing process of FB materials possibly due to defects in the materials themselves. Several works have reported the effects of different perturbations, such as disorder and nonlinearity, on FB lattices. For example, the effect of disorder has been studied in [47, 48] which showed that the presence of disorder will disrupt the destructive interference, which causes CLS, and thus the FB is destroyed. The effect of external fields was considered in [49] which showed that FBs are partially preserved in an external direct current field. Furthermore, the effect of nonlinearity was investigated in [50, 51] which showed that the destructive interference could be preserved using Kerr nonlinearity. It is worth noting that there also exist perturbations which keep the FB intact [52]. A detangling procedure of CLS from the dispersive part of the lattice allows one to preserve the FB even in the presence of disorder [45, 53]. As fabrication technology advances in many ways and there is an increase in the precision and accuracy that comes along with these advances, the study of FB systems is a very compelling topic of study.

On the topic of FB systems, a fundamental question concerns the structural stability of CLS when subjected to perturbations such as disorder. To address this question, a statistical analysis of the localisation characteristics of FB lattices

with onsite disorder was performed in [52]. Additionally, the interplay between nonlinearity and disorder was also explored in [54], as well as in lattices exhibiting FBs such as the so-called diamond lattice [40], stub lattice [53] and the pyrochlore ladder [16] as shown by the schematics in Fig. 1.1.

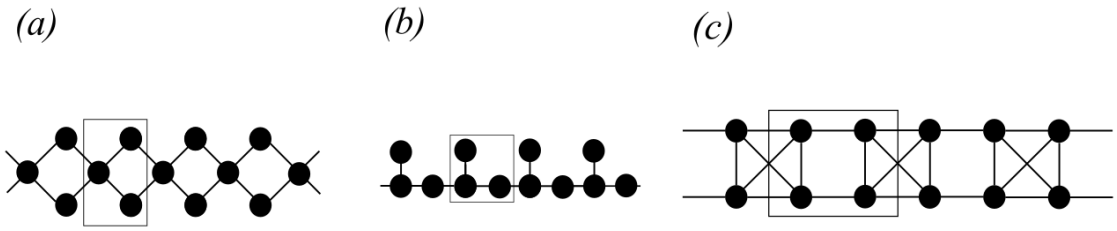

Figure 1.1: A schematic diagram of the lattice structures exhibiting FBs (a) diamond lattice, (b) stub lattice, (c) pyrochlore ladder. The box in each figure represents the unit cell of the lattice.

There is still, however, a lack of comprehensive studies in the literature that investigate the energy transport, chaotic behaviour, and energy polarisation of initially localised excitations in disordered and nonlinear FB networks. Recent review articles on the topic of FB lattices can be found in [45, 55, 56].

The objective of this thesis is to study the stub lattice model, which is one of the simplest lattice structure capable of supporting FBs based on a tight-binding approximation. We use this model for a detailed numerical examination of the impact of nonlinearity and disorder on the FB properties. More specifically, in this thesis we investigate the wave propagation, chaotic behavior, and energy polarisation of the stub lattice model across various energy spreading regimes of the system for a range of model parameters, trying to establish possible correlations between chaoticity, disorder, and nonlinearity. The results obtained from this work provide valuable insights into the stability and resilience of CLS when subjected to the combined influences of disorder and nonlinearity.

The thesis is organised as follows. In Chap. 2, we introduce the theoretical framework related to this study, also providing a basic literature review of some of the reported findings on the thesis topic. In Chap. 3, we describe in detail the stub lattice model and provide the procedure we adopt to determine the different wave packet spreading regimes and their boundaries. In Chap. 4, we then introduce the numerical techniques used in this study, as well as perform a brief overview of chaos indicators, mainly emphasising the ones which are implemented in our study. Code optimisation and related issues, are also discussed in Chap. 4. Then, in Chap. 5 our

numerical results are presented. Finally, in Chap. 6, we summarise our results and provide the conclusions of our study.

Chapter 2

Theory and background

In this chapter, we give the theoretical framework and perform a concise literature review of the topics and concepts relevant to our study. Specifically, in Sec. 2.1 the notion of dynamical systems is discussed. After that, in Sec. 2.2, we give an overview of Hamiltonian systems. Thereafter, the notion of chaos and associated concepts are covered in Sec. 2.3. In Sec. 2.4, we discuss the notion of lattice models emphasising disordered lattices. Finally, in Sec. 2.5, the concept of FBs and how they are generated is discussed.

2.1 Dynamical systems

We begin our work by providing an overview of the subject matter that will be important for our study. With this in mind, we start by recalling what dynamical system are. The material discussed in this section closely follows the presentation done in Chap. 3 of [57] and Chap. 1 of [58].

Dynamical systems are mathematical models developed to study the time evolution of real-life systems, aiming to provide descriptions of the system's change. An example of such a dynamical system is encountered in astrophysics in the study of galaxies and the movement of bodies in phase space [59]. Typically, dynamical systems can be categorised into two types, namely, (a) linear dynamical systems whose time evolution is described by a set of linear equations and (b) nonlinear dynamical systems which normally have some nonlinear terms in the evolution equations. Linear dynamical systems often have explicit general solutions which make them fairly simple to solve. Nonlinear dynamical systems, on the other hand, are generally impossible to solve using analytical means and those that can be solved analytically

correspond to special cases and are exceptionally rare. Because of this, the time evolution of nonlinear systems is obtained by using various numerical techniques.

Dynamical systems can be described by ordinary differential equations or partial differential equations having the general form

$$\dot{\mathbf{x}} = \mathbf{f}(\mathbf{x}, t), \tag{2.1}$$

where t is the variable representing time, $\dot{\mathbf{x}}$ is the time derivative of the vector of d-dependent variables $\mathbf{x} \in \mathbb{R}^d$, where d represents the number of dimensions and $\mathbf{f}$ is the vector field with $\mathbf{f} : \mathbb{R}^d \to \mathbb{R}^d$. The unique solution (or flow) of $\mathbf{f}$ is $\phi(\mathbf{x}, t)$, where for a point $\mathbf{x}_0 \in \mathcal{E}$ where $\mathcal{E}$ is an open subset of $\mathbb{R}^d$, the flow $\phi(\mathbf{x}_0, 0)$ passes through that point at $t = 0$. The flow satisfies two conditions. Firstly, $\phi(\mathbf{x}_0, 0) = \mathbf{x}_0$ and secondly, $\phi(\mathbf{x}, t + \tau) = \phi(\phi(\mathbf{x}, \tau), t)$ for all $\mathbf{x} \in \mathcal{E}$. These two conditions state that the flow, $\phi(\mathbf{x}_0, t)$, defines a trajectory associated to a certain initial condition $\mathbf{x}_0$, and describes how point $\mathbf{x}$ moves with respect to t.

In general, $\phi(\mathbf{x}, t)$ satisfies the following equation

$$\mathbf{f}(\mathbf{x}, \tau) = \frac{d}{dt}\phi(\mathbf{x}, t)|_{t=\tau}. \tag{2.2}$$

The interval of existence of the point $\mathbf{x}_0 \in \mathcal{E}$ of $\phi(\mathbf{x}_0, t)$ is given by $I(\mathbf{x}_0) = (-\infty, \infty)$. Therefore, $\mathbf{f}$ is a vector field and the dynamical system is described by the solutions of differential equations defined by $\mathbf{f}$. Conversely, $\phi(\mathbf{x}_0, t) \in \mathcal{E}$ if and only if $\mathbf{x}_0 \in \mathcal{E}$ and the interval of existence $I(\mathbf{x}_0)$ of $\phi(\mathbf{x}_0, t)$ is $(-\infty, \infty)$. Obviously, when working with physical systems, the vector fields are determined by the laws governing the system that we study. Instead of starting from a particular dynamical flow and deriving the vector field of the system, we can obtain the vector field based on the underlying laws and physics. We can determine whether or not a vector field will form a dynamical system by checking that solutions to a set of differential equations are unique. The uniqueness theorem states that two flows cannot cross each other at a particular time t such that $\phi(\mathbf{x}_i, t) \neq \phi(\mathbf{x}_j, t)$. Lastly, when the vector field $\mathbf{f}$ is explicitly dependent on time t, the system is called a non-autonomous system. If the vector field $\mathbf{f}$ is independent on time t, then the system is called an autonomous system.

2.2 Hamiltonian mechanics

In our study, we consider a particular type of dynamical system which is called a Hamiltonian system. However, before looking at Hamiltonian systems and their particular properties, we start by giving a brief overview of Newtonian mechanics. Before the idea of Hamiltonian systems was conceived and during the time Isaac Newton was building his theoretical understanding of the motions of objects in space, mechanics in general were thought of in terms of mass, forces, and speed. This approach was useful at the time as these quantities and their effects were directly observable and tangible. However, as more complex problems emerged, such as the three-body problem initially conceived by Euler, the use of Newtonian mechanics became insufficient in understanding and describing the physical world, as some problems did not have a closed-form solution. An effort was made to use transformations between different coordinate systems to obtain one which allows the simplest possible description of the studied dynamical system. Joseph-Louis Lagrange was one of the leading researchers in this development.

In Newtonian mechanics, the equation of motion of a particle is given by

$$\ddot{\mathbf{x}} = \mathbf{F}, \tag{2.3}$$

where $\mathbf{x}$ is the position vector, $\ddot{\mathbf{x}} \equiv \frac{d^2\mathbf{x}}{dt^2} \equiv \partial_t^2 \mathbf{x}$ is the second derivative with respect to time of $\mathbf{x}$, and $\mathbf{F}$ is the applied force. The total energy of the system, E, is an integral of motion in a conservative system and can be split into a kinetic part, K, and a potential part, V, where $E = K + V$, with $K = \frac{1}{2}m\dot{\mathbf{x}}^2$ (m is the mass of the particle) and V satisfying $\mathbf{F} = -\nabla V$. Another way of writing these equations of motion (EOM) is using the so-called Lagrangian formulation.

The Lagrangian formulation describes the dynamics of a system with N degrees of freedom (dof) (a degree of freedom refers to an independent generalised coordinate) using a set of generalised position coordinates, q_n, where $n = 1, 2, \ldots, N$, and the generalised position rate of change over time coordinates, $\dot{q}_n = dq_n/dt$. The Lagrange function, $\mathcal{L}$, takes the form (see e.g., in Chap. 1 of [60] and Chap. 3 of [61])

$$\mathcal{L}(q_1, \ldots, q_N, \dot{q_1}, \ldots, \dot{q_N}, t) = \mathcal{L}(\mathbf{q}, \dot{\mathbf{q}}, t) = K(\mathbf{q}, \dot{\mathbf{q}}, t) - V(\mathbf{q}, t), \tag{2.4}$$

where $\mathbf{q} = (q_1, \ldots, q_N)$ and $\dot{\mathbf{q}} = (\dot{q_1}, \ldots, \dot{q_N})$ and (2.4) describes a system in N-dof and would be a system with $2N$ different variables. $K(\mathbf{q}, \dot{\mathbf{q}}, t)$ and $V(\mathbf{q}, t)$ are respectively the kinetic energy and potential energy. We consider for a set of

functions $\mathbf{q}(t)$, $\mathbf{q}(t_1) = \mathbf{q}_1$, and $\mathbf{q}(t_2) = \mathbf{q}_2$. The Hamilton's action can be defined as follows

$$S = \int_{t_1}^{t_2} \mathcal{L}(\mathbf{q}, \dot{\mathbf{q}}, t) dt. \tag{2.5}$$

By utilising the calculus of variations (covered in [62]) we can determine the value of the action integral. This computation yields the Lagrangian EOM for a conservative system, also known as the Euler-Lagrange equations,

$$\frac{d}{dt}\frac{\partial \mathcal{L}}{\partial \dot{\mathbf{q}}} - \frac{\partial \mathcal{L}}{\partial \mathbf{q}} = 0. \tag{2.6}$$

Another way to describe a dynamical system is by following the so-called Hamiltonian formulation. The Hamiltonian formulation characterises a system by using the generalised position coordinates, $\mathbf{q}$, and the related generalised momenta coordinates, $\mathbf{p} = (p_1, \ldots, p_N)$. Considering that $\mathcal{L}(q_1, \ldots, q_N, \dot{q_1}, \ldots, \dot{q_N}) = \mathcal{L}(\mathbf{q}, \dot{\mathbf{q}})$, the transformation from the set $(\mathbf{q}, \dot{\mathbf{q}})$ to the set $(\mathbf{q}, \mathbf{p})$ is achieved via a Legendre transformation (see Chap. 2 of [60]) and defines the phase space. The system's phase space is all the possible states of the system determined by $\mathbf{q}$ and $\mathbf{p}$. The Hamiltonian function is defined as

$$H(\mathbf{q}, \mathbf{p}) = \sum_{n=1}^{N} [p_n \cdot \dot{q_n}] - \mathcal{L}(\mathbf{q}, \dot{\mathbf{q}}), \tag{2.7}$$

where $\dot{\mathbf{q}}$ is found from $\mathbf{p} = \frac{\partial \mathcal{L}}{\partial \dot{\mathbf{q}}}$. Using the Lagrange equation (2.6) we get the Hamilton's equations

$$\begin{aligned} \dot{\mathbf{q}} &= \frac{\partial H}{\partial \mathbf{p}}, \\ \dot{\mathbf{p}} &= -\frac{\partial H}{\partial \mathbf{q}}. \end{aligned} \tag{2.8}$$

The set of equations (2.8) constitutes a system of first order differential equations for the time evolution of position and momenta coordinates of the system. If the Hamiltonian (2.7) does not explicitly depend on time, then its value, which is commonly refered to as the system's energy, remains constant.

An important property of Hamiltonian systems is the symplectic nature of their flows. Suppose $\mathbb{M}(\mathbf{x})$ is a map where,

$$\mathbf{x}_{i+1} = \mathbb{M}(\mathbf{x}_i), \quad i = 0, 1, \ldots, \tag{2.9}$$

we define $\mathbb{M}$ to be symplectic if

$$D\mathbb{M}^T J_{2N} D\mathbb{M} = J_{2N}, \quad J_{2N} = \begin{pmatrix} \mathbf{0}_N & \mathbb{I}_N \\ -\mathbb{I}_N & \mathbf{0}_N \end{pmatrix}, \tag{2.10}$$

where D is the differential operator, $D\mathbb{M}$ is a Jacobian defined as

$$D\mathbb{M} = \begin{pmatrix} \frac{\partial \mathbb{M}_1}{\partial x_1} & \cdots & \frac{\partial \mathbb{M}_1}{\partial x_N} \\ \cdots & \ddots & \cdots \\ \frac{\partial \mathbb{M}_N}{\partial x_1} & \cdots & \frac{\partial \mathbb{M}_N}{\partial x_N} \end{pmatrix}, \tag{2.11}$$

$D\mathbb{M}^T$ is the transpose of that Jacobian, $\mathbb{I}_N$ is the $N \times N$ identity matrix and $\mathbf{0}_N$ is the zero matrix of size $N \times N$. Because of the symplectic nature of Hamiltonian systems, the flow, ϕ, preserves the phase space volume. This result is the so-called Liouville's Theorem (see [61]). This property of Hamiltonian systems results in the development of a set of specific integration methods which keeps the system's energy error bounded. These integration methods, which are called symplectic integrators (SI), will be used for numerical simulations and are further explained in Chap. 4.

2.3 Chaos

Poincaré's work during the late 1800s (see [63]) provided a qualitative approach to dynamical problems that contributed to the foundations for modern studies in chaos theory. Instead of looking for exact positions of planets at all times, he alternatively developed a geometric approach to planetary questions. This approach provided the basis for the subject of dynamics, and although not explicitly studying chaos, he laid the ground work for chaos theory. The invention and accessibility of high-speed computers during the 1950s marked a significant turning point in the field of dynamics, leading to the development of a deeper understanding of nonlinear systems. This continuous development of new computational problem solving techniques culminated in Lorenz's work in 1963. In his research, Lorenz tried to model the convection rolls in the atmosphere in order to understand its unpredictable nature [64]. Lorenz discovered that the outcomes generated by his equations did not reach a state of equilibrium or periodicity; instead, they displayed irregular, non-repeating oscillations. Additionally, even minor variations in the initial conditions of his simulations resulted in vastly different behaviors.

Chaotic systems are dynamical systems which at first glance appear to have random

processes and states, however, they are deterministic systems that are governed by underlying laws. Suppose V is a set and $f : V \to V$ a map on this set. f is chaotic on V if it has the following three properties [65]:

1. f has sensitive dependence on initial conditions.
2. f is topologically transitive.
3. periodic orbits are dense in V.

The most common and recognised way of describing chaotic systems is by condition 1, f having sensitive dependence on initial conditions means that any change in f's initial condition, no matter how small, will result in a completely different outcome, given enough time. Small perturbations to the original initial condition, in systems that are not chaotic, will result in extremely similar outcomes over a very long period of time. Condition 2 states that if we have two separate non-empty regions on our set V, then if f passes through one of the non-empty regions it will eventually pass through the other. Condition 3 states that for every infinitesimally small region in V, a periodic orbit, which is an unique solution for a dynamical system where the orbit repeats itself in time, can be found.

The issue of chaos along with various chaos detection techniques will be further discussed in Chap. 4 of this work.

2.4 Normal modes and disorder in lattices

Before beginning to understand the notion of disordered lattices, we firstly discuss the idea of normal modes in a classical lattice setup before looking at lattices defined by the tight-binding approximation. Much of the work done in this section follows from the steps found in Chap. 2 of [66] and Chap. 3 of [67]. We can first consider an one-dimensional (1D) system with N particles arranged next to each other. The particles in the 1D system are numbered $n = 1, \ldots, N$ where N is a positive integer. The particles can freely undergo small oscillations described by displacements $\mathbf{x}_{n,j}$ around their equilibrium positions $\mathbf{r}_{n,j}$, where $j = 1, 2, 3$ (in this thesis we consider just one spatial dimension), the number of dof in which a particle can displace translationally in cartesian coordinates. We describe the total oscillating potential energy, V, as a Taylor expansion about the equilibrium position (see equation (2.1)

of [66])

$$V = V_0 + \sum_{n}^{N}\sum_{j}^{3} \frac{\partial V}{\partial \mathbf{x}_{n,j}}\mathbf{x}_{n,j} + \frac{1}{2}\sum_{n,n'}^{N}\sum_{j,j'}^{3} \mathbf{x}_{n,j}\frac{\partial^2 V}{\partial \mathbf{x}_{n,j}\partial \mathbf{x}_{n',j'}}\mathbf{x}_{n',j'} + \dots \ . \tag{2.12}$$

The dynamics will be unchanged by the constant term V_0. The first order force constant, $\frac{\partial V}{\partial \mathbf{x}_{n,j}}$, can be disregarded as the oscillations about the equilibrium position will not change V to the first order. The second order force constant term will, therefore, be the dominating term in the Taylor expansion and with these assumptions, the total energy of the system can be written as a sum of the kinetic and potential energy terms

$$E = \frac{1}{2}\sum_{n}^{N}\sum_{j}^{3} m_n \dot{\mathbf{x}}_{n,j}^2 + \frac{1}{2}\sum_{n,n'}^{N}\sum_{j,j'}^{3} \mathbf{x}_{n,j}\frac{\partial^2 V}{\partial \mathbf{x}_{n,j}\partial \mathbf{x}_{n',j'}}\mathbf{x}_{n',j'}. \tag{2.13}$$

Using the following coefficients

$$\begin{aligned} s_{n,j} &= m_n^{1/2}\mathbf{x}_{n,j}, \\ W_{n,j,n',j'} &= (m_n m_{n'})^{-1/2} V_{n,j,n',j'}, \end{aligned} \tag{2.14}$$

where $V_{n,j,n',j'}$ is the second order force constant $\frac{\partial^2 V}{\partial \mathbf{x}_{n,j}\partial \mathbf{x}_{n',j'}}$, and m_n is the mass of the particle n, the expression (2.13) can be written as

$$E = \frac{1}{2}\sum_{n}^{N}\sum_{j}^{3} \dot{s}_{n,j}^2 + \frac{1}{2}\sum_{n,n'}^{N}\sum_{j,j'}^{3} W_{n,j,n',j'} s_{n,j} s_{n',j'}. \tag{2.15}$$

Using (2.15), we obtain the classical EOM for lattice dynamics

$$\ddot{s}_{n,j} + \sum_{n',j'} W_{n,j,n'j'} s_{n',j'} = 0. \tag{2.16}$$

Following the steps found in Chap. 2 of [66], in order to convert from cartesian coordinates to normal coordinates, the solutions to (2.16) for the normal vibrations of the system will form an unitary matrix allowing us to make the conversion. This change is useful as any arbitrary motion in a system can be represented using a linear combination of all the normal coordinates in a system. We obtain the EOM (2.16) in normal coordinates, g_ν, where ν is an index for the modes,

$$\ddot{g_\nu} + \omega_\nu^2 g_\nu = 0, \tag{2.17}$$

where ω_ν represents the frequency of the νth mode.

The model analysed above represents a simple 1D system. In general, for the case of an oscillating system, the normal mode, ν, describes how the system's individual elements move relative to each other at a particular frequency ω_ν.

2.4.1 Tight-binding model

Solids by definition are collections of tightly-bound atoms which are arranged in regular patterns forming lattice structures. The electrons from these tightly-bound atoms are freely moving about and between the lattice environment and the movement of freely roaming electrons determine many properties of the solid. As we will be working with lattice models throughout the work, it is important to establish a way in which to represent the model in a simple yet representative manner. For lattices, the tight-binding approximation provides a good description of the system as a whole. In the tight-binding approximation, the electrons are not free to roam between the lattice environment but are restricted to particular discrete atom sites with only a small probability to hop to neighbouring sites. These electrons are said to be tightly-bounded to a lattice site and can be represented by their wave functions. Since the wave function is present at discrete sites on the lattice, this allows the wave function to be identified by the index of the site it is residing at. The overlapping of wave functions with neighbouring sites are negligible in the tight-binding approximation. Much of the discussion in this section follows from the work done in Chap. 2 of [45].

Let us now consider a 1D lattice of size N, where the sites are arranged in a line and the distance between sites are consistently the same throughout the lattice. Because in the tight-binding approximation, the wave functions overlapping between neighbouring sites is negligible, we can consider the basis state vectors as

$$|n\rangle = \begin{pmatrix} \vdots \\ 0 \\ 1 \\ 0 \\ \vdots \end{pmatrix}, \quad \langle n| = \begin{pmatrix} \dots & 0 & 1 & 0 & \dots \end{pmatrix}, \tag{2.18}$$

where the nth element of the basis state vectors is 1, and represents an electron that is tightly-bounded to the nth discrete site of the lattice. $\langle \cdot | \cdot \rangle$ and $|\cdot\rangle\langle\cdot|$ are the

so-called Bra-Ket and Ket-Bra notations, used to denote the inner and outer products of vectors for quantum states, respectively. Furthermore, $\langle n|m\rangle = \delta_{n,m}$, where $\delta_{n,m}$ is the usual Kronecker delta function and represents the fact that we have an orthonormal set of basis state vectors and $\sum_n^N |n\rangle\langle n| = 1$. Note that we would not be able to make this assumption if there was an overlapping of wave functions between sites i.e., hoppings are not negligible.

The Hamiltonian that describes the system when the electron remains at its original site without any hopping between neighbouring sites is

$$H_0 = E_0 \sum_n^N |n\rangle\langle n|, \tag{2.19}$$

where H_0 is the Hamiltonian and E_0 is the energy of the eigenstates for the solution to the Hamiltonian.

Next, we consider the Hamiltonian for the time-independent Schrödinger equation, for a transitionally invariant lattice of size N which can be expressed as

$$H|\psi\rangle = E|\psi\rangle. \tag{2.20}$$

Here H denotes an $N \times N$ matrix which describes the Hamiltonian of the lattice and $|\psi\rangle$ is the state vector. The state vector can be written as a linear combination of the basis state vectors $|n\rangle$, and the wave function, ψ_n, at the site n such that

$$|\psi\rangle = \sum_n \psi_n |n\rangle. \tag{2.21}$$

A way of describing the ability of electrons to hop from one discrete site n to another m can be done in the following way

$$T_{n,m} = \langle n|H|m\rangle, \tag{2.22}$$

where $T_{n,m}$ is the matrix defining the interactions between site n and m. Because wave functions are localised to each site, this hopping of electrons is the only way transport can occur. A consideration one needs to make for electron hopping, is that the electrons are more likely to hop to close neighbouring sites than those sites which are further away from it. With this in mind, the final form of the H in (2.20) can be written as

$$H = \sum_n \epsilon_0 |n\rangle\langle n| - \sum_{n,m} T_{n,m} |n\rangle\langle m|, \tag{2.23}$$

which takes into account the electron hopping to neighbouring sites and ϵ_0 is the onsite energy. The distance that the electron can hop can be determined by m. If only nearest neighbour hopping is considered, the sites $n+1$ and $n-1$ can be destinations for electrons that hop from site n. The m will sum from sites $n-1$ to $n+1$ excluding site n which will mean that the Hamiltonian for nearest neighbour hopping becomes

$$H = \sum_n \epsilon_0 |n\rangle\langle n| - T \sum_n (|n\rangle\langle n+1| + |n+1\rangle\langle n|), \tag{2.24}$$

where T is the hopping parameter. Using (2.23) and (2.21) and substituting into (2.20), we obtain

$$\epsilon_0 \psi_n - \sum_{n,m} T_{n,m} \psi_n = E\psi_n, \tag{2.25}$$

which is an eigenvalue problem for a general tight-binding model with hoppings probability from site n to m determined by $T_{n,m}$. In our studies, we are considering nearest neighbour hopping and therefore the eigenvalue problem will be as follows

$$\epsilon_0 \psi_n - T(\psi_{n+1} + \psi_{n-1}) = E\psi_n, \tag{2.26}$$

which uses (2.24) [instead of (2.23)], and (2.21), both of which are substituted into (2.20).

Bloch's theorem [68] states that the solution to the Schrödinger's equation found in (2.20), can be written as a product of two factors. Firstly, a plane wave factor which represents the free electron behaviour and secondly, a periodic function which represents the influence of the lattice potential at each site. Consider the nearest neighbour hopping eigenvalue problem found in (2.26), whose solution can be written as

$$\psi_n = \frac{1}{\sqrt{N}} \sum_q u(q) e^{-iqn}, \tag{2.27}$$

where $\frac{1}{\sqrt{N}}$ is the normalisation factor, $u(q)$ is the periodic function, known as the Bloch function, which captures the periodicity of the lattice potential, e^{-iqn} is the plane wave factor, and q represents the wave number which characterises the momentum of an electron. Substituting (2.27) into (2.26) and simplifying, we obtain

$$E = \epsilon_0 - 2T\cos q. \tag{2.28}$$

The solution of (2.28), which is solved for any value q, will form a band structure (a range of energy levels that an electron can take) where q will have an associated

energy $E(q)$. The band structure gives us the dispersion relation of the system which describes the relationship between the energy of the eigenstates and the wave number.

2.4.2 Anderson localisation

Disordered dynamical systems with multiple dofs have been very useful as mathematical models for real-world physical phenomena as they can mimic the heterogeneity and diversity which is ubiquitous in nature. In his seminal work, P.W. Anderson predicted the absence of wave packet diffusion in disordered electronic systems [17] and is an example of how disorder can dramatically alter the behavior of wave propagation which has led to significant advancements in our understanding of wave packet spreading.

We now discuss the notion of AL with respect to tight-binding based models. We introduce randomness, by taking onsite energies ϵ_n from an uniform probability distribution, i.e., $\epsilon_n \in [-W/2, W/2]$, with W being the disorder strength. If no disorder is present in the system, an electron can move around freely, however, with disorder, the dynamics of how the electron behaves will fundamentally change and the electron would be Anderson localised. P.W. Anderson's findings on the localisation of electrons represented as wave functions earned him a Nobel prize in 1977. The concept of AL is much more general and can be applied to a large variety of systems, including light waves [69], acoustic waves [70], microwaves [71] and condensed matter [6].

At first, it was challenging to observe AL directly in matter due to the unavoidable interaction between atoms, but as experimental methods improved, researchers have been able to get direct observations of AL [5, 72, 73]. The topic of AL has been comprehensively studied in both numerical and theoretical contexts [54, 74, 75, 76]. Additionally, direct observation of the localisation of light was achieved in [77]. Further experiments included the use of 1D photonic lattices [72] and ultra-cold atoms [73]. These experiments have allowed for researchers to study the interplay between the nonlinear terms in the modeled system (nonlinearity) and disorder to complement numerical investigations [74, 78, 79, 80]. Several works have demonstrated that nonlinearity destroys localisation. Specifically, nonlinearity caused subdiffusive spreading to occur in two distinct regimes. Research, such as that presented in [81, 82], showed that this spreading induced by nonlinearity was a chaotic process.

Consider the Hamiltonian for the tight-binding approximation for the Anderson model [17, 83] below

$$H = \sum_n \epsilon_n |\psi_n|^2 - (\psi_{n+1}\psi_n^* + \psi_{n+1}^*\psi_n), \tag{2.29}$$

where ψ_n and ψ_n^* denote the wave function and its complex conjugate at the nth unit cell, respectively. Using (2.29) and the fact that the EOM for (2.29) are obtained through $d\psi_n/dt = \partial H/\partial(i\psi_n^*)$, the EOM for the Anderson model are

$$i\dot{\psi}_n = \epsilon_n\psi_n - (\psi_{n+1} + \psi_{n-1}), \tag{2.30}$$

where $\psi_n = U_n e^{-i\omega t}$ is the solution of the linear wave equation at site n for a lattice size of N, U_n is the amplitude of the wave at a particular site n, and ω is the frequency.

Substituting the solution of the linear wave equations into the EOM for the Anderson model, we obtain the time-independent equations described as

$$\omega U_n = \epsilon_n U_n - (U_{n+1} + U_{n-1}). \tag{2.31}$$

The above time-independent equations are written as an eigenvalue problem

$$\omega \mathbb{I}\boldsymbol{U} = \boldsymbol{A}\boldsymbol{U}, \tag{2.32}$$

where $\boldsymbol{U} = (U_1, U_2, \ldots, U_N)$,

$$\boldsymbol{A} = \begin{pmatrix} \epsilon_1 & -1 & 0 & \cdots & 0 & 0 \\ -1 & \epsilon_2 & -1 & \cdots & 0 & 0 \\ 0 & -1 & \epsilon_3 & \cdots & 0 & 0 \\ \vdots & \vdots & \vdots & \ddots & \vdots & \vdots \\ 0 & 0 & 0 & \cdots & \epsilon_{N-1} & -1 \\ 0 & 0 & 0 & \cdots & -1 & \epsilon_N \end{pmatrix}, \tag{2.33}$$

and $\mathbb{I}$ is the $N \times N$ identity matrix. We solve the eigenvalue problem (2.32) to find its eigenvectors and eigenvalues by diagonalising matrix $\boldsymbol{A}$. The former represents the profile or eigenstates for a mode, ν, and the latter represents its associated eigenfrequency or energy. Solving the above linear eigenvalue problem by diagonalising the matrix $\boldsymbol{A}$ without disorder ($\epsilon_n = 0$), all modes will be spatially extended spanning the length of the lattice size, N. Figs. 2.1 (a) and (b) show the profile of modes $\nu = 1$ and $\nu = 200$ for a homogeneous lattice, i.e., $W = 0$.

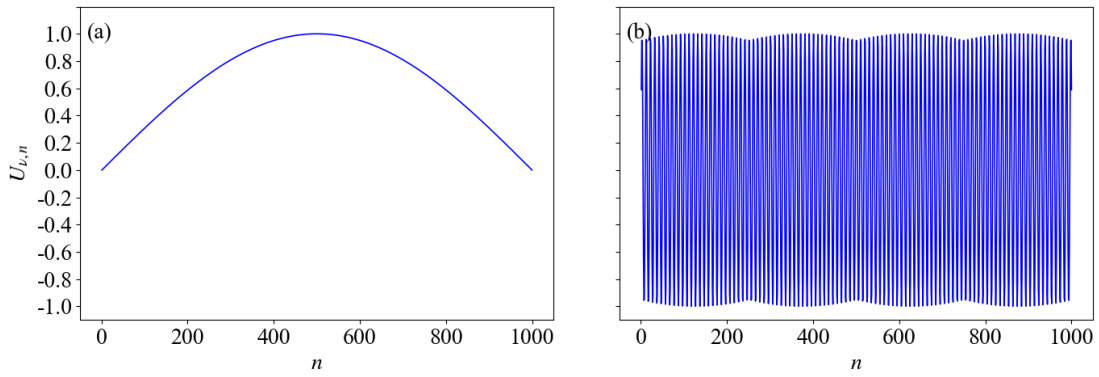

Figure 2.1: Typical mode profiles for the homogeneous lattice ($W = 0$) of the Anderson model (2.29), with a lattice size of $N = 1000$. The mode index is denoted by ν and the eigenfrequencies of the lattice are sorted in ascending order. (a) $\nu = 1$, (b) $\nu = 200$.

Introducing disorder to the system ($W > 0$), we observe that the modes become localised to only a few lattice sites instead of the entire lattice in Figs. 2.2 (a) and (b).

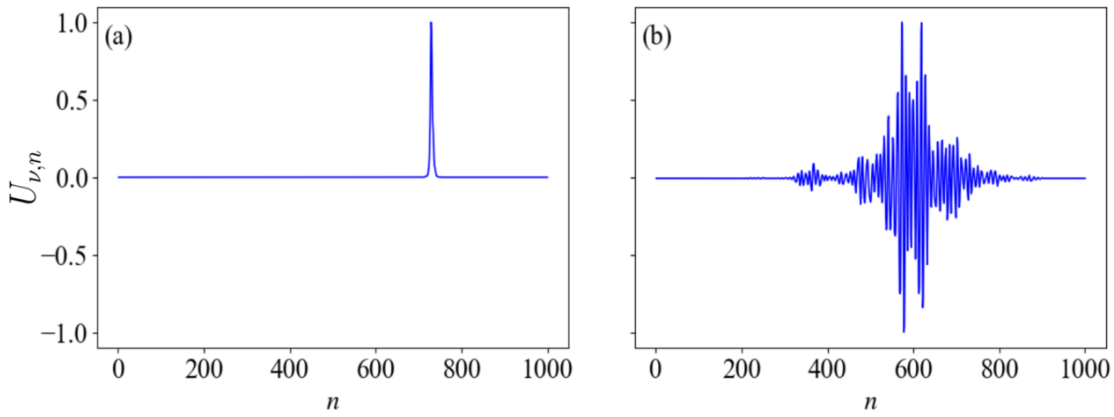

Figure 2.2: Plot similar to Fig. 2.1 with (a) $\nu = 1$, (b) $\nu = 200$ but for $W = 1$.

In the presence of disorder, as seen in Figs. 2.2 (a) and (b), the modes show an exponential decay which is described by $|U_{\nu,n}| \propto e^{-\frac{1}{\xi(\omega_\nu)}}$. For disorder strength $W \leq 4$, the $\xi(\omega_\nu)$ is given by $\xi(\omega_\nu) \approx \frac{24(4-\omega_\nu)}{W^2}$ and is called the localisation length [17, 84]. Several numerical techniques can be used to calculate this localisation

length such as the random matrix theory and the transfer matrix method [84]. Two more quantities that are commonly used to determine the level of localisation of the modes are the so-called localisation volume [85], which characterises the spatial region occupied by mode ν and is defined as the number of lattice sites for which the amplitude of the mode is not exponentially small. The localisation volume of the νth mode is computed as

$$V_\nu = \sqrt{12 m_2^{(\nu)}} + 1, \tag{2.34}$$

where $m_2^{(\nu)} = \sum_n (n - \bar{n}_\nu)^2 |U_{\nu,n}|^2$ is the so-called second moment of a mode, and $\bar{n}_\nu$ is the modes centre defined as $\bar{n}_\nu = \sum_n n |U_{\nu,n}|^2$. Another commonly used localisation quantifier is the participation number [85], which describes the number of modes that makes the greatest contribution to the spatial distribution. The participation number of the νth mode is computed as

$$P_\nu = \frac{1}{\sum_n |U_{\nu,n}|^4}. \tag{2.35}$$

2.5 Flatbands and compact localised states

Flatbands refer to frequency bands with no dispersion ($\omega(q) = \textit{constant value}$, such as that shown in Fig. 2.3) and FB networks consist of at least one dispersive band and one FB and are generated from CLS. For instance, when considering a system with isolated sites, such that hoppings between neighbouring sites are non-existent, the electrons, described by wave functions, will not be able to move between sites and the whole system will have one energy value which will be represented by a dispersionless band (a constant value). When we consider a system where isolated sites are moved closer together, wave functions can hop between sites and the dispersionless band of the system vanishes. However, an interesting question arises when sites are not isolated and whether we still keep FBs or constant dispersive bands. The appearance of isolated sites is due to the lattice symmetry. In symmetric lattices, the wave functions hopping from one site to another results in destructive interference as wave functions with identical amplitudes and opposite phases cancel each other out. The destructive interference result in the wave function being present in only a finite region of the lattice and zero elsewhere. These localised states play a crucial role in making the overall effect of hoppings between lattice sites vanish, creating the illusion that the sites are isolated. In certain cases, given any disorder strength, there will exist no dispersive bands that will be flat due to the fact that disorder in the system will disrupt the destructive interferences. The stub lattice model is one such

lattice which possesses these interesting properties and we study it to understand not just the interplay of disorder and nonlinearity but also the effect of the CLS on the dynamics. We discuss the pertinent issues of the nonlinear stub lattice model in Chap. 3.

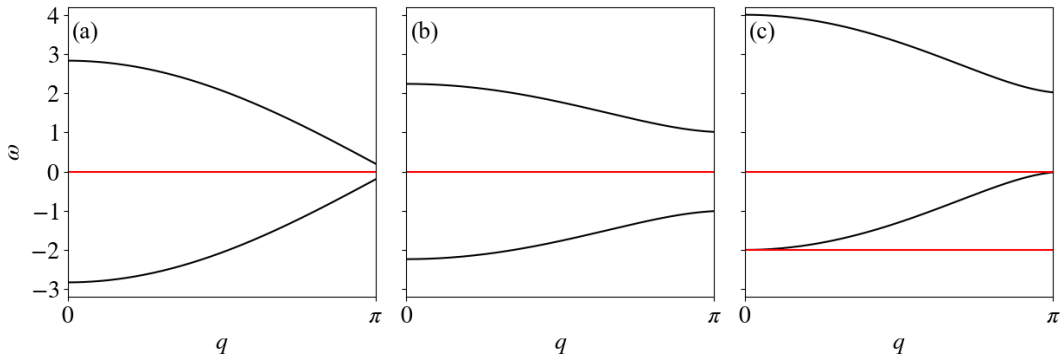

Figure 2.3: Dispersion relations of tight-binding based lattice models depicted in Fig. 1.1 showing FBs (red lines) for (a) diamond chain, (b) stub and (c) pyrochlore ladder lattice, with $\omega(q)$ representing the frequency. The lattice schematics for (a), (b) and (c) can be found in Fig. 1.1.

Chapter 3

Model and expected dynamical regimes

In this chapter we introduce the tight-binding stub lattice model, which is one of the simplest lattice structures exhibiting FBs. This chapter is organised as follows. In Sec. 3.1, we give a general introduction to the stub lattice model, providing details of its governing Hamiltonian and what makes the model unique. We demonstrate the presence of the FB in the stub lattice model dispersion relation as well as look at how disorder will affect the FB properties. Thereafter, in Sec. 3.2, we explore and define the different spreading regimes of an initially localised wave packet in the stub lattice model.

3.1 The stub lattice model

Now we discuss the model that will be the main focus of this investigation. The stub lattice model exhibits FBs in its dispersion relation and the lattice structure of the model can be described by the schematic in Fig. 3.1. We consider a lattice of size N, where each unit cell or site n contains three subsites labeled A, B and C. These subsites have connections in the form of inter- and intra-unit cell hoppings, where subsite A of the nth unit cell has hoppings to subsite B and C of unit cell n and subsite B of unit cell $n-1$. Subsite B of the nth unit cell has hoppings to subsite A of unit cell n and $n+1$. Finally, subsite C of the nth unit cell has hoppings to subsite A of unit cell n. The hoppings between subsites are indicated as solid lines in Fig. 3.1.

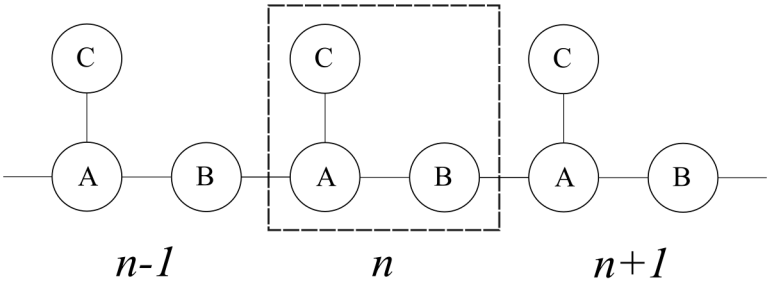

Figure 3.1: A schematic diagram of the stub lattice model. The unit cell, indexed n, contains three components (circles) denoted A, B and C. The solid lines connecting the components represents the intra- and inter-unit cell hoppings.

Following from the schematic in Fig. 3.1, we derive the Hamiltonian for the 1D, nonlinear, disordered and discrete stub lattice model using a tight-binding nearest neighbour hopping approximation, which is given by adding onsite energies and nonlinear terms to each of the subsites in an unit cell. The resulting Hamiltonian is

$$\begin{aligned} H = &\sum_{n=1}^{N} \epsilon_n^{(A)} \left|\psi_n^{(A)}\right|^2 + \frac{\beta}{2}\left|\psi_n^{(A)}\right|^4 + \epsilon_n^{(B)}\left|\psi_n^{(B)}\right|^2 + \frac{\beta}{2}\left|\psi_n^{(B)}\right|^4 + \epsilon_n^{(C)}\left|\psi_n^{(C)}\right|^2 \\ &+ \frac{\beta}{2}\left|\psi_n^{(C)}\right|^4 - (\psi_n^{(C)*}\psi_n^{(A)} + \psi_n^{(C)}\psi_n^{(A)*}) - (\psi_n^{(A)*}\psi_n^{(B)} + \psi_n^{(A)}\psi_n^{(B)*}) \\ &- (\psi_{n+1}^{(A)*}\psi_n^{(B)} + \psi_{n+1}^{(A)}\psi_n^{(B)*}), \end{aligned} \tag{3.1}$$

where the Hamiltonian contains the wave function, $\psi_n^{(K)}$, for every subsite of an unit cell n, where K denotes the subsites A, B and C, as well as the onsite energy terms, $\epsilon_n^{(A)}$, $\epsilon_n^{(B)}$ and $\epsilon_n^{(C)}$, and the positive number representing the nonlinearity strength, β. The onsite energy terms are independently chosen from an uniform distribution $[-W/2, W/2]$, where W represents the disorder strength. The wave function is given by, $\psi_n^{(K)} = U_n^{(K)} \exp(-i\omega t)$ where ω is the frequency at the Kth subsite at the nth unit cell. $\psi_n^{(K)*}$ is the complex conjugate of $\psi_n^{(K)}$, and $U_n^{(K)}$ describes the spatial profile (amplitude) of the wave, while t is the time, and i is the imaginary unit.

Firstly, we consider the linear case, i.e., $\beta = 0$, by substituting the wave function into the EOM for the stub lattice model generated by

$$\dot{\psi}_n^{(K)} = \frac{\partial H}{\partial\left(i\psi_n^{(K)*}\right)}, \tag{3.2}$$

to obtain the time-independent equations [52]

$$\begin{aligned}
\omega U_n^{(A)} &= \epsilon_n^{(A)} U_n^{(A)} - U_{n-1}^{(B)} - U_n^{(B)} - U_n^{(C)}, \\
\omega U_n^{(B)} &= \epsilon_n^{(B)} U_n^{(B)} - U_n^{(A)} - U_{n+1}^{(A)}, \\
\omega U_n^{(C)} &= \epsilon_n^{(C)} U_n^{(C)} - U_n^{(A)}.
\end{aligned} \tag{3.3}$$

Initially, we consider an infinite homogeneous lattice ($\epsilon_l^{(K)} = 0$) of infinite length without any disorder present in the system. The dispersion relation for this case can be obtained by expressing ω as an eigenvalue of the matrix [16]

$$\boldsymbol{E} = \begin{pmatrix} 0 & 1 + e^{-iq} & 1 \\ 1 + e^{iq} & 0 & 0 \\ 1 & 0 & 0 \end{pmatrix}, \tag{3.4}$$

where q represents the wave number. Solving the eigenvalue problem gives us three dispersion relations, described by $\omega = 0$ and $\omega = \pm\sqrt{3 + 2\cos q}$. The FB is described by $\omega = 0$ and the two dispersive bands are described by $\omega = \pm\sqrt{3 + 2\cos q}$ as shown in Fig. 3.2. Note that the FB and dispersive bands are separated by band gaps of size $\alpha = 1$ indicated as the grey region in Fig. 3.2. This gap is taken between the FB ($\omega = 0$) and the maximum propagating frequency of the lower dispersive band ($\omega = -\sqrt{3 + 2\cos q}$), as well as the minimum propagating frequency of the upper dispersive band ($\omega = +\sqrt{3 + 2\cos q}$).

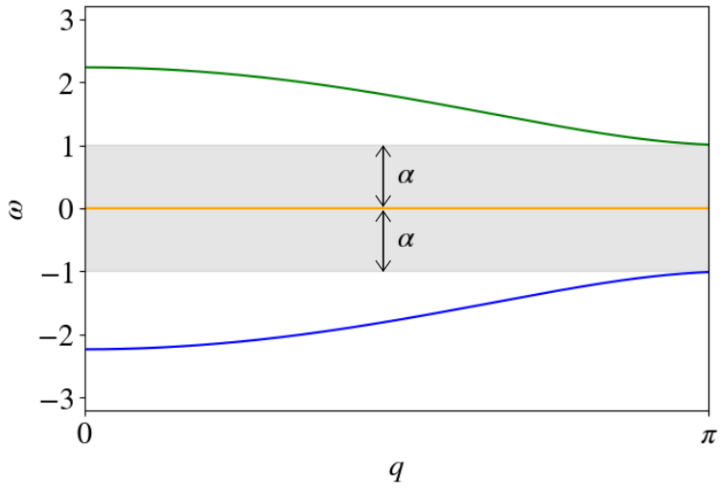

Figure 3.2: Stub lattice model (3.1) dispersion relation ($\beta = 0$, linear case). There exist three distinct bands, one flat (orange) and two dispersive (green and blue) bands, $\omega = 0$ and $\omega = \pm\sqrt{3 + 2\cos q}$ respectively. The band gap between the maximum propagating frequency of the lower dispersive band and the flatband (also the same as the difference between the minimum propagating frequency of the upper dispersive band and flatband) is $\alpha = 1$ which is indicated as the grey region.

For the stub lattice model there exist three subsites for each unit cell, so the number of modes is $3N$ for a lattice size of N. Solving (3.3) numerically as an eigenvalue problem for a lattice size $N = 1000$, will produce eigenvectors and eigenvalues. The $3N$ eigenvectors produced will characterise the profile (amplitude) of eigenstates for a mode, ν, and the $3N$ eigenvalues produced represent the mode's associated frequency. Following the methodology used when solving the Anderson model in Sec. 2.4.2, we present the profiles of modes $\nu = 1, 1500$, and 2500 for the linear ordered stub lattice model in Fig. 3.3.

We observe in Figs. 3.3 (a) and (c), the mode $\nu = 1$ on the lower dispersive band (blue band in Fig. 3.2), and the mode $\nu = 2500$ on the upper dispersive band (green band in Fig. 3.2) respectively. In both Figs. 3.3 (a) and (c), there are 3 separate profiles for each ν, represented using the colours of orange, blue, and green, where these profiles each span the length of the lattice size, $N = 1000$. The three profiles in Figs. 3.3 (a) and (c) are normalised such that for each dof, the maximum or minimum amplitude is either $U_{\nu,n} = 1$ or $U_{\nu,n} = -1$. For Fig. 3.3 (b), $\nu = 1500$, on the FB (orange band in Fig. 3.2) shows no amplitude and remains flat, represented

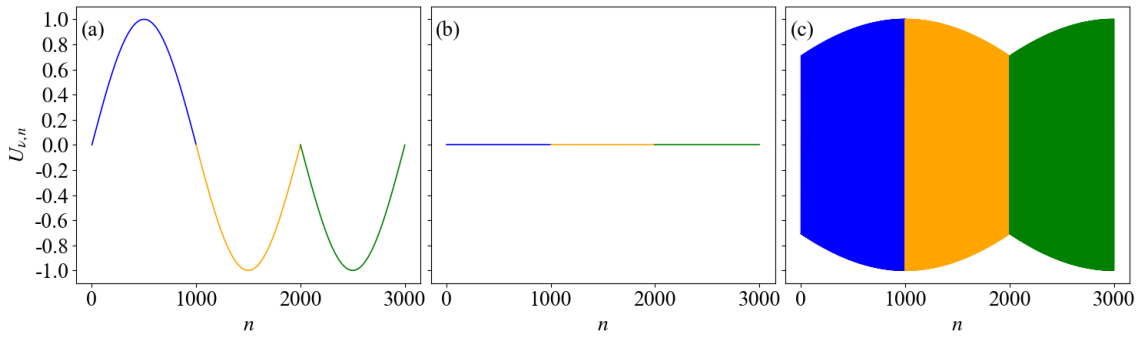

Figure 3.3: The profile of modes in the linear ordered stub lattice model, with a lattice size of $N = 1000$. The disorder strength used was $W = 0$ and the eigenfrequencies of the model were sorted in ascending order (a) $\nu = 1$, (b) $\nu = 1500$, (c) $\nu = 2500$.

by the fact that the amplitudes of the 3 separate profiles are all at $U_{\nu,n} = 0$.

Let us now discuss the effect of disorder on the linear stub lattice model. In particular, we introduce disorder on the onsite energies $\epsilon_n^{(K)}$ at each subsite A, B, and C in (3.3) from a randomly chosen uniform distribution, $\epsilon_n^{(K)} \in [-W/2, W/2]$, where W is the disorder strength. We again solve the eigenvalue problem (3.3) for a variety of disorder strengths ranging from $W = 0.5$ to $W = 2.5$ for a lattice of size $N = 1000$. In order to obtain statistically reliable results, we average our findings for each W value over 50 disorder realisations. A single disorder realisation is simply an independent computation where the values chosen for $\epsilon_n^{(K)}$ are kept constant during the numerical evolution of the system. The addition of disorder to the finite stub lattice model alters the piece-wise frequency spectra as seen in Fig. 3.4. In particular, the introduction of disorder results to the destruction of the FB in Fig. 3.2 as a range of ω values, which are above and below $\omega = 0$, emerge. This is due to the fact that disorder disrupts the destructive interference that gives rise to the CLS and the formation of FBs [52]. More specifically, the growth of the disorder strength W increases the range of ω values that each of the three bands in Fig. 3.2 occupy and consequently the FB becomes less flat as its eigenfrequencies fill the band gap.

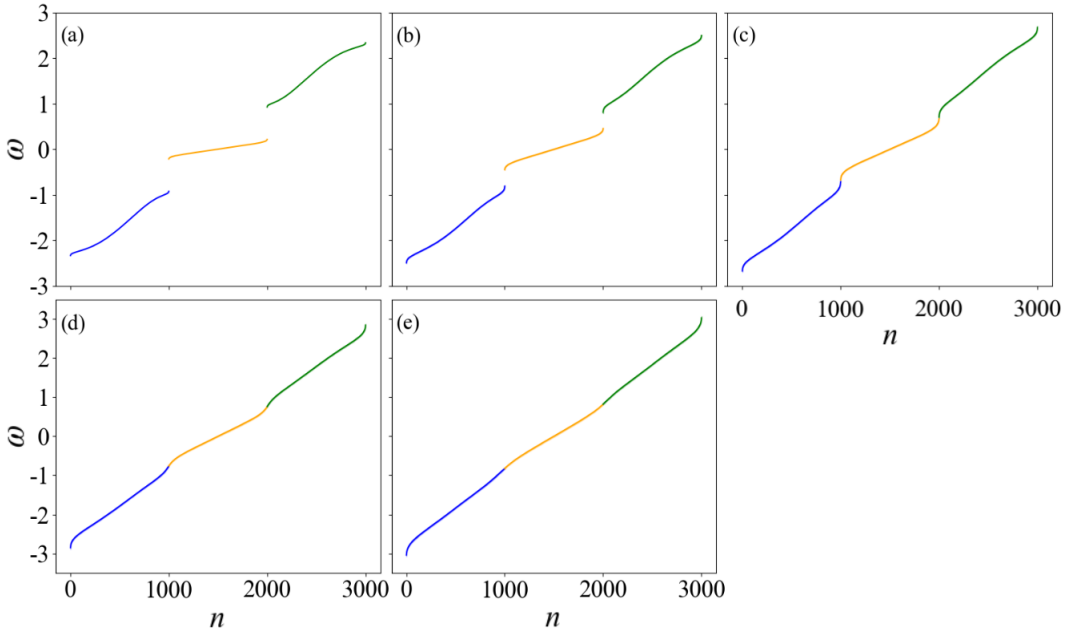

Figure 3.4: (a) Average frequency spectra over 50 disorder realisations for a disordered stub lattice of size $N = 1000$ and disorder strength $W = 0.5$. (b)-(e) Similar to (a) but for $W = 1.0$, $W = 1.5$, $W = 2.0$, and $W = 2.5$, respectively. Error-bars denoting one standard deviation from the average frequency values are too small to be noticeable.

From the results of Fig. 3.4, we see that the increase of W eventually leads to the disappearance of the band gap seen in Fig. 3.2, as the space in between the different bands in the dispersion relation is filled up by eigenfrequency values. As W increases, there is a critical W value where the width of the band gap vanishes (i.e. $\alpha = 0$) and the piece-wise frequency spectra practically becomes continuous. Numerically, we find this critical W value to be $W \approx 1.58$.

The spectrum width Δ [86, 87] is defined as $\Delta = |\omega_{max} - \omega_{min}|$ with ω_{max} and ω_{min} being the maximum and minimum ω value respectively of the spectra seen in Fig. 3.4. Since, in the linear disordered case, we chose $\epsilon_n^{(K)}$ values from a uniform distribution in the interval $[-W/2, W/2]$, ω_{min} and ω_{max} are obtained by finding the eigenvalues of matrix (3.4), with onsite energy values on the main diagonal of the matrix (3.4) which are either $-\frac{W}{2}$ or $\frac{W}{2}$. Solving these particular eigenvalue

problems with the minimum and maximum onsite energies we obtain

$$\omega_{min} = -W/2 - \sqrt{5}, \tag{3.5}$$

and

$$\omega_{max} = W/2 + \sqrt{5}. \tag{3.6}$$

which means that $\Delta = W + 2\sqrt{5}$. We note that Δ does not account for the gaps that may be present for low W values.

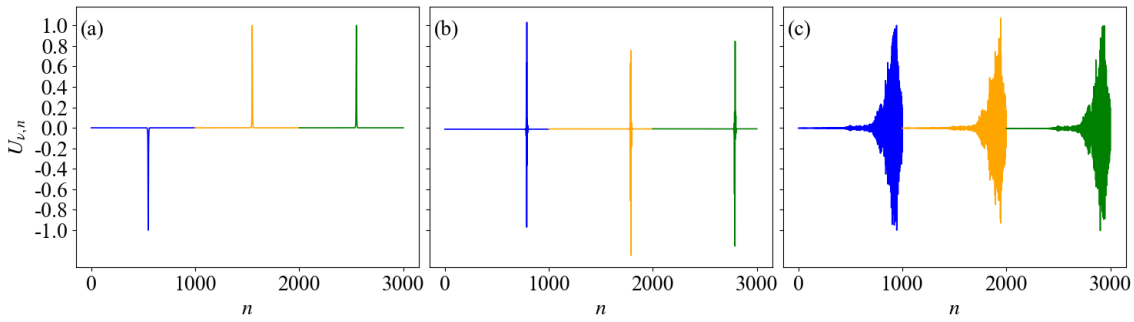

Figure 3.5: Plots similar to Fig. 3.3 with (a) $\nu = 1$, (b) $\nu = 1500$, (c) $\nu = 2500$ but for $W = 0.4$

We recall that for the Anderson model (see Fig. 2.2), the introduction of disorder induces localisation of the modes. In Fig. 3.5, we show the profiles of three modes, namely the ones for $\nu = 1$, $\nu = 1500$, and $\nu = 2500$ for $W = 0.4$ and for lattice size of $N = 1000$. Unlike the representative cases of the ordered system seen in Fig. 3.3, where all the modes were extended, Fig. 3.5 shows profiles of localised modes.

3.1.1 Preserving the flatband in the presence of disorder

As seen in Fig. 3.4, any disorder strength $W > 0$, disrupts the FB as ω does not keep a constant value in it. Therefore, a natural question that can be asked is if there is a way of preserving the FB such that $\omega = 0$ even when $W > 0$. As was previously mentioned in Chap. 1, FBs are formed from CLS which are created through destructive interference and lattice symmetry. However, when disorder is introduced to the onsite energies, the destructive interference is disrupted leading

to the disappearance of CLS. Consequently, the flatness of the FB is no longer preserved as seen in Fig. 3.4. However, by placing symmetric onsite energies in a particular manner, the destructive interference can be maintained and the CLS remain intact allowing the preservation of FBs [53]. For the stub lattice model, the CLS are created by the proper manipulation of subsites B and C (see Fig. 3 in [52]) such that their onsite energies have the same amplitude but opposite signs. In our study, we preserve the FB by setting the onsite energies as $\epsilon_n^{(B)} = \epsilon_n^{(C)} = 0$ and $\epsilon_n^{(A)}$ randomly chosen in the interval $\epsilon_n^{(A)} \in [-W/2, W/2]$. The resulting frequency spectra for various values of W are seen in the panels of Fig. 3.6.

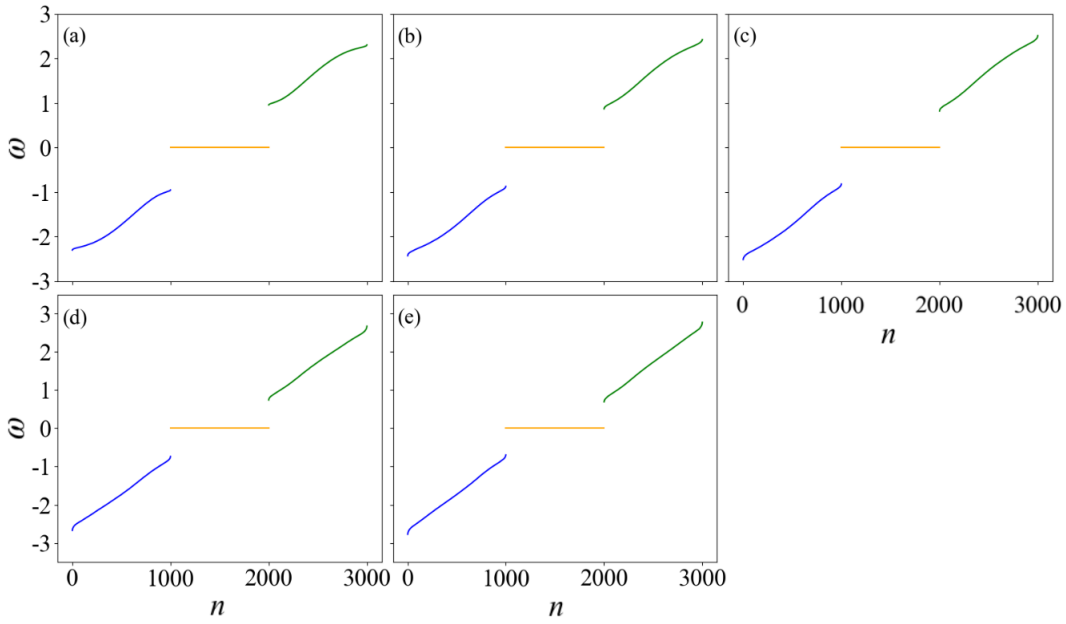

Figure 3.6: (a) Average frequency spectra over 50 disorder realisations for a disordered stub lattice and parameters such that the flatband is preserved, $\epsilon_n^{(B)} = \epsilon_n^{(C)} = 0$, of size $N = 1000$ and disorder strength $W = 0.5$. (b)-(e) Similar to (a) but for $W = 1.0$, $W = 1.5$, $W = 2.0$, and $W = 2.5$, respectively. Error-bars denoting one standard deviation from the average frequency values are too small to be noticeable.

By comparing Fig. 3.4 and Fig. 3.6, whose corresponding panels refer to the same W value, we see that the FB is preserved and represented by a constant $\omega = 0$ value when disorder is introduced only in the A subsite.

3.2 Expected dynamical regimes

In the presence of disorder, the profiles of the modes are localised to just a few lattice sites due to AL. The localisation volume [see also (2.34)] can be used to measure the extent of mode localisation, taking into account the three frequency bands that exist in the stub lattice model (see the differently colored bands in Fig. 3.4). The localisation volume of the νth mode for the stub lattice model is computed as

$$V = \max\left(V_\nu^{(i)}\right) = \max\left(\sqrt{12 m_2^{(\nu,i)}} + 1\right), \quad i = 1, 2, 3, \tag{3.7}$$

where $m_2^{(\nu,i)} = \sum_n^N (n - \bar{n}_\nu)^2 |U_{\nu,n}^{(i)}|^2$ is the second moment of the amplitude profile of the νth mode in the ith frequency band, while $\bar{n}_\nu = \sum_n n |U_{\nu,n}^{(i)}|^2$ is the average position of the mode distribution's centre. The index i identifies the spectrum band which corresponds to mode ν when all the computed frequencies are sorted in increasing value. Each frequency spectrum band has a total of N modes such that $i = 1$ would refer to the frequency spectrum of the lowest N frequency values (lower dispersive band, colored in blue, in Fig 3.2), $i = 2$ refers to the frequency spectrum of the intermediate N frequency values (FB, colored in orange, in Fig 3.2), and finally, $i = 3$ refers to the frequency spectrum of the highest N frequency values (upper dispersive band, colored in green, in Fig 3.2).

As discussed in Chap. 2, the participation number can be computed [see also (2.35)] to measure the extent of localisation. Once again we need to take into account the three separate frequency bands of the stub lattice model, so that the participation number for the νth mode can be computed as

$$P = \max\left(P_\nu^{(i)}\right) = \max\left(\frac{1}{\sum_n^N |U_\nu^{(i)}|^4}\right) \quad i = 1, 2, 3. \tag{3.8}$$

We find averaged, over 50 disorder realisations, results for V (3.7) and P (3.8) in order to obtain statistically sound conclusions denoting the related quantities as $\langle V \rangle$ and $\langle P \rangle$ respectively. The obtained results are shown as solid curves in Fig. 3.7. We also compute $\langle P_\nu^{(i)} \rangle$ and $\langle V_\nu^{(i)} \rangle$ (see dotted curves in Fig. 3.7), i.e., respectively the participation number and localisation volume of the modes for each of the three frequency branches separately against disorder strength W. For very weak disorder ($W \lesssim 1.4$), the $\langle P_\nu^{(2)} \rangle$ and $\langle V_\nu^{(2)} \rangle$ values of modes taken from the intermediate N frequency values (represented by the dotted lines (*iv*) and (*iii*) respectively in Fig. 3.7), remain practically constant, which is in agreement with some of the reported works [53]. However, for $W \gtrsim 1.4$, $\langle P_\nu^{(2)} \rangle$ and $\langle V_\nu^{(2)} \rangle$ show

a dependency on W, decreasing with increasing W. The $\langle P_\nu^{(1)} \rangle$ and $\langle V_\nu^{(1)} \rangle$ values of modes taken from the lowest N frequency values shows a decreasing slope when $W \lesssim 1.4$ indicated in Fig. 3.7 by the dotted curves $(viii)$ and (vii) respectively. Particularly, the $\langle V_\nu^{(1)} \rangle$ shows a decreasing slope of $\langle V \rangle \approx \dfrac{70}{W^2}$ in this weak disorder region indicated by the black dashed line in Fig. 3.7. A similar behaviour is seen in the $\langle P_\nu^{(3)} \rangle$ and $\langle V_\nu^{(3)} \rangle$ values of modes taken from the highest N frequency values which shows a decreasing slope when $W \lesssim 1.4$ indicated in Fig. 3.7 by the dotted curves (vi) and (v) respectively with $\langle V_\nu^{(3)} \rangle$ showing a decreasing slope of $\langle V \rangle \approx \dfrac{70}{W^2}$. In Fig. 3.7, the solid curves of (i) and (ii) are respectively the $\langle V \rangle$ and $\langle P \rangle$ values obtained as the maximum $\langle V_\nu^{(i)} \rangle$ and $\langle P_\nu^{(i)} \rangle$ value of the three frequency branches at a particular W value.

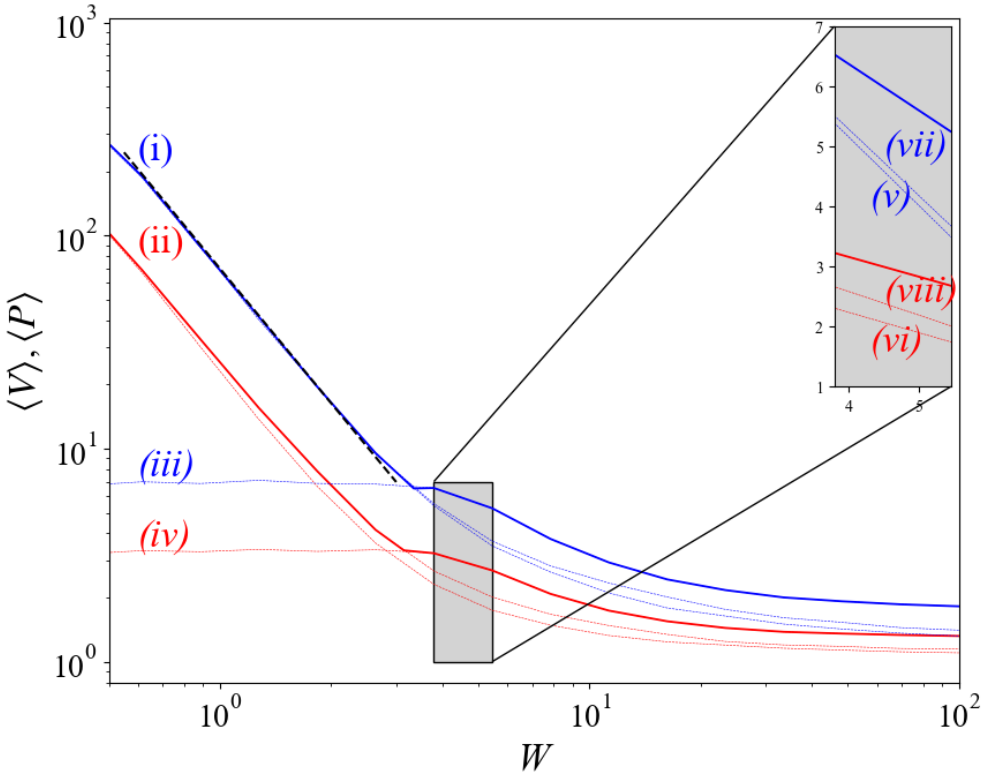

Figure 3.7: Numerical estimations of the maximum $\langle V \rangle$ (3.7) (solid blue line) and $\langle P \rangle$ (3.8) (solid red line) for disorder strength W, averaged over 50 disorder realisations. The dotted lines denote $\langle V_\nu^{(i)} \rangle$ (3.7) and $\langle P_\nu^{(i)} \rangle$ (3.8) for each of the three frequency bands of N values when the mode frequencies are sorted in increasing value. (i) and (ii) respectively corresponds to the maximum $\langle V_\nu^{(i)} \rangle$ and $\langle P_\nu^{(i)} \rangle$ values of the three frequency branches. (iii) and (iv) represents $\langle V_\nu^{(2)} \rangle$ and $\langle P_\nu^{(2)} \rangle$ values of modes taken from the intermediate N frequency values respectively. (vii) and $(viii)$ represents $\langle V_\nu^{(1)} \rangle$ and $\langle P_\nu^{(1)} \rangle$ values of modes taken from the lowest N frequency values respectively. (v) and (vi) represents $\langle V_\nu^{(3)} \rangle$ and $\langle P_\nu^{(3)} \rangle$ values of modes taken from the highest N frequency values respectively. The black dashed line corresponds to a function proportional to $70/W^2$.

As discussed in Sec. 3.1, all eigenfrequencies are found within a bounded interval of width Δ. Each mode has a localisation volume, $V_\nu^{(i)}$, and the average frequency spacing of all modes is $d \approx \dfrac{\Delta}{\langle V \rangle}$, where $\langle V \rangle = \max\left(\langle V_\nu^{(i)} \rangle\right)$. In the absence of nonlinearity in a disordered setup, energy will not spread due to the localised nature of

the modes. On the other hand, the presence of nonlinearity results in mode interaction which allows energy to spread [78, 79]. The nonlinearity will induce frequency shifts given by $\delta \approx \beta s$ [88], where s is the average energy norm at each unit cell. For high energies, this frequency shift will be larger than the frequency spectrum width, $\beta s > \Delta$, and therefore an excited mode will be set out of resonance with respect to the non-excited neighbouring ones. The general condition for determining the boundary in the systems parameter space of the self trapping regime was found to be $\delta = \Delta - 2\epsilon_n$ [88], with ϵ_n being the onsite energy value at the initially excited sites, approximated by $\epsilon_n \approx \frac{W}{2}$ [79]. For relatively small frequency shifts, where the energy is relatively low, we have $\beta s < \Delta$, and consequently the self trapping condition is not fulfilled and initially localised wave packets will spread. Within this relatively low energy there exist two spreading behaviours. Firstly, for large enough energies, each mode can strongly interact with other modes when the size of the frequency shift is greater than the average frequency spacing, i.e, $\delta > d$. This case is called the strong chaos regime [88, 83]. Secondly, if the size of the frequency shift is smaller than the average frequency spacing ($\delta < d$), modes will weakly interact resulting to a slower energy spreading. This dynamical behaviour is named the weak chaos regime [88, 83]. We adopt a similar approach to the one used in [79] for determining the boundaries in the stub lattice parameter space of the various dynamical regimes. In order to determine the boundaries between the strong and weak chaos, the value of the estimated localisation volume, $\langle V \rangle = 70/W^2$ (see Fig. 3.7), is used. The boundary for the self trapping regime is found using $\delta = \Delta - 2\epsilon_n$, where $\Delta = W + 2\sqrt{5}$ and $\epsilon_n \approx \frac{W}{2}$ such that the functional form of the self trapping boundary is $\delta = 2\sqrt{5}$ and is seen as the horizontal black dashed line in Fig. 3.8. The boundary between the weak ($\delta \approx \beta s < d$) and strong ($\delta \approx \beta s > d$) chaos regimes is determined using $d \approx \dfrac{\Delta}{\langle V \rangle}$ such that the functional form of the boundaries between weak and strong chaos is $\delta = \frac{W^2(W+2\sqrt{5})}{70}$ and is seen as the curved black dashed line in Fig. 3.8. According to [74, 75], for a single site initial excitation, the strong chaos regime does not appear and therefore we expect to observe only the self trapping regime: $\delta > \Delta$ and weak chaos regime: $\delta < \Delta$.

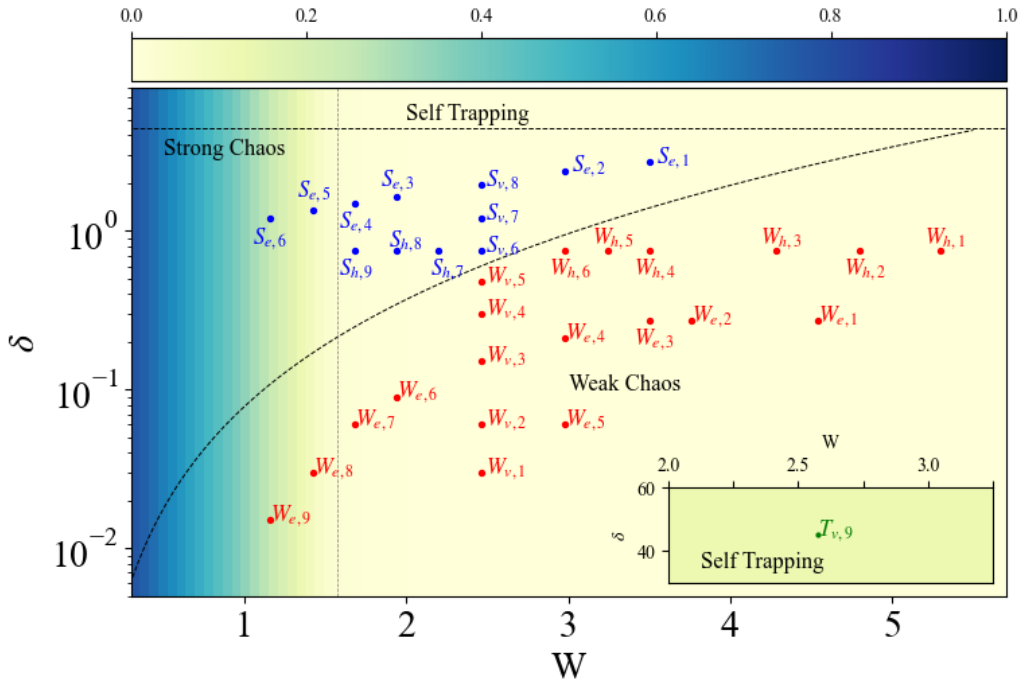

Figure 3.8: Estimated spreading regimes for the stub lattice model demarcated by the dashed black curves. The colour bar indicates the size α of the frequency gap, while the vertical dashed line at $W = 1.58$ indicates the disorder strength at which the gap start to appear as W decreases. The initial parameters in the weak ($W_{.,.}$) and strong ($S_{.,.}$) chaotic regimes are indicated as red and blue respectively while a self trapping initial condition is indicated in green. *Vertical*, *Horizontal*, and *Elsewhere* set of initial conditions are labeled with a subscript v, h, and e, respectively.

The location of the weak chaos, strong chaos, and self trapping regimes in the stub lattice parameter space (δ,W), when non single site excitations are considered, are seen in Fig. 3.8. Fig. 3.8 is very important for the study of the system we carry out in Chap. 5 as it allows us to choose β and W values to study the wave packet dynamics in different dynamical regimes. Fig. 3.8 shows the parameter space (δ,W) of the stub lattice model with the placement of the expected three dynamical regimes: weak chaos (below the curved black dashed line), strong chaos (between the curved black dashed line and the horizontal black dashed line) and self trapping

(above the horizontal black dashed line). The colour bar indicates the size α of the frequency gap, while the vertical dashed line at $W = 1.58$ indicates the disorder strength at which the gap start to appear as W decreases. The position of several system set up belonging to the weak chaos (red points), strong chaos (blue points) and self trapping (inset, green point) regimes studied in detail in Chap. 5 are also given and are respectively denoted by $W_{\cdot,\cdot}$, $S_{\cdot,\cdot}$ and $T_{\cdot,\cdot}$. The first subscript in each point correspond to the words vertical (v), horizontal (h) and elsewhere (e), whose meaning is explained in Chap. 5, while the second subscript is just a counter of the various cases. However, before we present our numerical results, we first discuss the numerical integration and chaos detection techniques we use in our work in Chap. 4.

Chapter 4

Numerical approaches

In this chapter, we present the different numerical techniques implemented in our study, expanding the discussions on SI and chaos briefly mentioned in Chap. 2. In addition, we consider practical issues related to our numerical simulations like optimisation, time efficiency and implementation aspects of our computer codes. The structure of this chapter is as follows. In Sec. 4.1, we cover the idea of numerical integration using SI. Thereafter, in Sec. 4.2, the notion of variational equations for Hamiltonian systems is defined. After that, in Sec. 4.3, we extend our discussion from Sec. 2.3 on chaos detection techniques. Then, in Sec. 4.4, we derive the EOM and variational equations for the stub lattice model. In Sec. 4.5, we present how we selected the most suitable symplectic integrator for our purposes, emphasising considerations on computational speed and accuracy.

4.1 Numerical integration using symplectic integrators

Following the discussion on Hamiltonian mechanics of Sec. 2.2, and recalling that one of the properties of Hamiltonian systems is the symplectic nature of their flow, we will focus our attention on a class of integration schemes for Hamiltonian systems called SI which are designed in order to preserve the symplectic nature of Hamiltonian flow [89]. However, before doing that, we will describe in some detail the general idea of numerical integration. Certain systems, such as nonlinear Hamiltonian models, cannot be solved using analytical methods and, therefore, approximate solutions of their evolution equations are obtained using numerical integration techniques. Thus, the solution of the EOM of continuous time, t, systems are approximated by

discretising t as $t_k = t_0 + k\tau$, where t_k is a discrete time, t_0 is the initial time of the systems evolution, τ is a fixed integration time step, and k is a non-negative integer including zero. Then, the numerical integration scheme approximates the actual solution of the EOM at the discretised times, t_k. Examples of commonly used numerical integration techniques are the well-known Runga-Kutta methods (see [90]), which nevertheless have some shortcoming which make them inappropriate for the purposes of our work. These issues are related to their numerical accuracy over long integration times and to the computational time which may be needed, and will be discussed in more detail below.

Because the solutions of the evolution equations of Hamiltonian systems are approximated by the use of numerical integration schemes, there will always be a small error between the exact solution and the one given by the numerical integrator. In order to make sure that our approximate solutions are accurate enough, we use the fact that the total energy of the Hamiltonian should be conserved. The relative energy error, H_r, is given by

$$H_r(t_k) = \left| \frac{H(0) - H(t_k)}{H(0)} \right|, \tag{4.1}$$

with $H(0)$ representing the initial energy value at $t = 0$ and $H(t_k)$ is the numerically computed energy at the integration time t_k. For non-SI, the relative energy error grows linearly as the time of the numerical computation increases [91]. If long time simulations of a system are needed, smaller integration time steps will be necessary to keep the relative energy error low, which means that longer CPU times will be required to keep H_r below a chosen upper bound. Due to the accumulation of error when using non-SI methods, the numerical simulations performed in this study were done using a symplectic integration method, as SI, always keep the relative energy error bounded by some upper limit, as well as make the computations more time efficient (see [92]).

The EOM for a Hamiltonian, H, can be written as

$$\frac{d\mathbf{X}}{dt} = \{H, \mathbf{X}\} = \mathcal{L}_H \mathbf{X} \implies \mathbf{X}(\tau) = e^{\tau \mathcal{L}_H} \mathbf{X}_0, \tag{4.2}$$

where $\mathbf{X} = (\mathbf{q}, \mathbf{p})$ is the vector containing the generalised position and momenta coordinates, $\{\cdot, \cdot\}$ is the Poisson bracket, $e^{\tau \mathcal{L}_H} \mathbf{X}_0$ denotes the solution of the EOM with $\mathbf{X}_0 = \mathbf{X}(0)$ being the vector at the initial time $t = 0$ and τ is the integration

time step. Finally, $\mathcal{L}_H = \{H, \cdot\}$ is the differential operator defined as

$$\mathcal{L}_H f = \sum_{n=1}^{N} \left(\frac{\partial H}{\partial q_n} \frac{\partial f}{\partial p_n} - \frac{\partial H}{\partial p_n} \frac{\partial f}{\partial q_n} \right). \tag{4.3}$$

The most common way of constructing SI is by splitting the Hamiltonian function into the sum of two integrable parts, $H = \mathcal{A} + \mathcal{B}$, where $\mathcal{A}$ and $\mathcal{B}$ could for example represent the kinetic and potential energy terms, respectively, if they are both integrable. In that case, $H(\mathbf{q}, \mathbf{p})$, can be written as $H(\mathbf{q}, \mathbf{p}) = \mathcal{A}(\mathbf{p}) + \mathcal{B}(\mathbf{q})$, where $\mathcal{A}$ and $\mathcal{B}$ are explicitly independent only on $\mathbf{q}$ and $\mathbf{p}$ respectively. Then a symplectic scheme for integrating the EOM (4.2) consists of approximating the operator $e^{\tau L_H}$ by

$$e^{\tau \mathcal{L}_H} = e^{\tau(\mathcal{L}_\mathcal{A} + \mathcal{L}_\mathcal{B})} = \Pi_{i=1}^{j} e^{c_i \tau \mathcal{L}_\mathcal{A}} e^{d_i \tau \mathcal{L}_\mathcal{B}} + \mathcal{O}(t^{P+1}), \tag{4.4}$$

where P is an integer (called the order of the integrator) and $i = 1, \ldots, j$. The appropriate values of constants c_i and d_i can be numerically found [93]. These constants will differ according to the symplectic integrator used. So, given a set of initial conditions $\mathbf{X}_0$, the dynamics of a Hamiltonian system over an integration time step τ are approximated by a series of successive actions of the operators $e^{c_i \tau \mathcal{L}_\mathcal{A}}$ and $e^{d_i \tau \mathcal{L}_\mathcal{B}}$

$$\mathbf{X}(\tau) = \Pi_{i=1}^{j} e^{c_i \tau \mathcal{L}_\mathcal{A}} e^{d_i \tau \mathcal{L}_\mathcal{B}} \mathbf{X}_0. \tag{4.5}$$

Repeated applications of (4.5), where $\mathbf{X}(\tau)$ becomes $\mathbf{X}_0$ for the successive integration time step will approximate the evolution of the system.

4.2 Variational equations for Hamiltonian systems

A way of investigating the chaotic behaviour of a dynamical systems is to take from the position of a point in phase space, $\mathbf{X}$, an infinitesimally small perturbation, $\delta\mathbf{X}$, and check how $\delta\mathbf{X}$ evolves over time. The small perturbation is essentially a vector describing the distance between two points in the same phase space and is called a deviation vector. A deviation vector, $\mathbf{w}(t)$, for an N-dimensional Hamiltonian system where $H(\mathbf{q}, \mathbf{p}) = \mathcal{A}(\mathbf{p}) + \mathcal{B}(\mathbf{q})$, is given as

$$\mathbf{w}(t) = \delta\mathbf{X}(t) = (\delta q_1(t), \ldots, \delta q_N(t), \delta p_1(t), \ldots, \delta p_N(t)). \tag{4.6}$$

In order to describe how the deviation vector, $\mathbf{w}(t)$, will evolve over a period of the integration time, the set of the so-called variational equations need to be integrated [94, 95, 96]. The evolution of the deviation vector is governed by

$$\dot{\mathbf{w}}(t) = A(t)\mathbf{w}(t), \tag{4.7}$$

where

$$A(t) = \begin{pmatrix} \mathbf{0}_N & D^2\mathcal{A}(\mathbf{p})_{i,j} \cdot \mathbb{I}_N \\ -D^2\mathcal{B}(\mathbf{q})_{i,j} \cdot \mathbb{I}_N & \mathbf{0}_N \end{pmatrix}, \tag{4.8}$$

where $\mathbb{I}_N$ is the $N \times N$ identity matrix, $\mathbf{0}_N$ is the zero matrix of size $N \times N$, $D^2\mathcal{A}(\mathbf{p})_{i,j}$ and $D^2\mathcal{B}(\mathbf{q})_{i,j}$ are the Hessian matrices of the terms $\mathcal{A}$ and $\mathcal{B}$ evaluated at points $\mathbf{p}(t)$ and $\mathbf{q}(t)$, respectively,

$$\begin{aligned} D^2\mathcal{A}(\mathbf{p}(t))_{i,j} &= \frac{\partial^2 \mathcal{A}}{\partial p_i \partial p_j}\Big|_{\mathbf{p}(t)} \quad , i,j = 1,2,\ldots,N, \\ D^2\mathcal{B}(\mathbf{q}(t))_{i,j} &= \frac{\partial^2 \mathcal{B}}{\partial q_i \partial q_j}\Big|_{\mathbf{q}(t)} \quad , i,j = 1,2,\ldots,N, \end{aligned} \tag{4.9}$$

and $D = \left[\frac{\partial}{\partial q_1} \; \frac{\partial}{\partial q_2} \cdots \frac{\partial}{\partial q_N} \; \frac{\partial}{\partial p_1} \; \frac{\partial}{\partial p_2} \cdots \frac{\partial}{\partial p_N}\right]^T$, where $(^T)$ denotes the transpose of the matrix. For a separable Hamiltonian system of the form $H(\mathbf{q},\mathbf{p}) = \mathcal{A}(\mathbf{p}) + \mathcal{B}(\mathbf{q})$, the evolution of the variational equations can be written as

$$\begin{aligned} \delta\dot{\mathbf{q}} &= D^2\mathcal{A}(\mathbf{p})\delta\mathbf{p}, \\ \delta\dot{\mathbf{p}} &= -D^2\mathcal{B}(\mathbf{q})\delta\mathbf{q}. \end{aligned} \tag{4.10}$$

4.3 Chaos indicators

Let us now focus on using the most recognisable property of chaos, i.e., the sensitive dependence on initial conditions, to determine the chaoticity of orbits in the phase space of a dynamical system. There are two main approaches to accomplish that. The first way is to make a local study of particular orbits and the second way is to characterise the global chaoticity of the phase space [95, 96]. For both approaches, it is important to have a chaos indicator, i.e., a way to measure how chaotic an orbit is. The study of the chaoticity can be done through the use of the so-called Lyapunov characteristic exponents (LCEs) (see e.g. [94, 97, 98]) and in particular, by estimating the maximum Lyapunov exponent (mLE). Looking at solely the evolution of an individual trajectory in phase space is not enough to categorise the chaotic behaviour of that orbit, but we need to estimate its mLE, which measures the rate of growth of a small perturbation to the considered trajectory. A method for computing the LCEs is to consider a small spherical region in phase space around a point. As time evolves, the point follows a trajectory and the small region is stretched into an ellipsoid. The ellipsoid has N principal axes which are the line segments from the centre of the ellipsoid on the axes of symmetry. Then,

the LCEs are determined using the lengths of these principal axes of the system.

The spectrum of LCEs (i.e., the set of all LCEs) is given as [94, 96, 99]

$$\Lambda_i = \lim_{t\to\infty} \frac{1}{t} \ln \lambda_i(t) \quad i = 1, 2, \ldots, N, \tag{4.11}$$

where λ_i are appropriate quantities obtained by solving the variational equations (4.7) and obtaining $\mathbf{w}(t) = Y(t)\mathbf{w}(0)$. Here $Y(t)$ is the so-called fundamental matrix of solutions and $\mathbf{w}$ is the deviation vector. The fundamental matrix of solutions is usually decomposed as $Y(t) = Q(t)R(t)$ where $Q(t)$ is an orthogonal $N \times N$ matrix and $R(t)$ is an upper-triangular matrix whose diagonal elements are real positive numbers. The decomposition from $R(t)$ allows one to compute the spectrum of Lyapunov exponents [94, 96, 99], Λ_i, with $i = 1, \ldots, N$. The largest exponent Λ_1 is also called the mLE. The computation of the mLE can be achieved by taking a point in the phase space of a dynamical system with a set of initial conditions, $\mathbf{X}(0)$, and an initial deviation vector $\mathbf{w}(0)$ and evolving both the orbit and the deviation vector respectively using the systems EOM (2.8) and variational equations (4.10). Then, the mLE is therefore defined as

$$\Lambda_1 = \lim_{t\to\infty} \ln \frac{1}{t} \frac{||\mathbf{w}(t)||}{||\mathbf{w}(0)||}, \tag{4.12}$$

where $\mathbf{w}(t)$ is the deviation vector at a specific time, t, $\mathbf{w}(0)$ is the initial deviation vector at $t = 0$, and $||\cdot||$ denotes the usual Euclidian norm. If $\Lambda_1 > 0$, the orbit is chaotic, because the length of the perturbations grows exponentially fast. On the other hand, the perturbations of a regular orbit will not grow exponentially and, therefore, Λ_1 approaches zero in time approximately following an evolution of the form $\Lambda_1 \propto t^{-1}$.

4.4 Stub lattice model equations of motion and variational equations

Now we can obtain the Hamiltonian EOM as well as the variational equations for the stub lattice model. To do that, we first express Hamiltonian (3.1) in a form containing generalised position and momenta coordinates. The conversion is done by implementing the canonical transformation $\psi_n^{(K)} = (q_n^{(K)} + ip_n^{(K)})/\sqrt{2}$ and $\psi_n^{(K)*} =$

$(q_n^{(K)} - ip_n^{(K)})/\sqrt{2}$, and substituting into (3.1). We therefore obtain

$$\begin{aligned} H = &\sum_{n=1}^{N} \frac{\epsilon_n^{(A)}}{2}\left\{\left(q_n^{(A)}\right)^2 + \left(p_n^{(A)}\right)^2\right\} + \frac{\beta}{8}\left\{\left(q_n^{(A)}\right)^2 + \left(p_n^{(A)}\right)^2\right\}^2 + \frac{\epsilon_n^{(B)}}{2}\left\{\left(q_n^{(B)}\right)^2 + \left(p_n^{(B)}\right)^2\right\} \\ &+ \frac{\beta}{8}\left\{\left(q_n^{(B)}\right)^2 + \left(p_n^{(B)}\right)^2\right\}^2 + \frac{\epsilon_n^{(C)}}{2}\left\{\left(q_n^{(C)}\right)^2 + \left(p_n^{(C)}\right)^2\right\} + \frac{\beta}{8}\left\{\left(q_n^{(C)}\right)^2 + \left(p_n^{(C)}\right)^2\right\}^2 \\ &- \left(p_n^{(C)}p_n^{(A)} + q_n^{(C)}q_n^{(A)}\right) - \left(p_n^{(A)}p_n^{(B)} + q_n^{(A)}q_n^{(B)}\right) - \left(p_{n+1}^{(A)}p_n^{(B)} + q_{n+1}^{(A)}q_n^{(B)}\right), \end{aligned} \tag{4.13}$$

where N is the lattice size, $p_n^{(K)}$ is the generalised momenta value, and $q_n^{(K)}$ is the generalised position value at site n, where K denotes subsites A, B, and C. Following the discussion of Sec. 4.1, we note that in order to integrate the Hamiltonian system using a symplectic integrator, we split H into two separate Hamiltonian functions such that $H = \mathcal{A} + \mathcal{B}$ where

$$\begin{aligned} \mathcal{A} = &\sum_{n=1}^{N} \frac{\epsilon_n^{(A)}}{2}\left\{\left(q_n^{(A)}\right)^2 + \left(p_n^{(A)}\right)^2\right\} + \frac{\beta}{8}\left\{\left(q_n^{(A)}\right)^2 + \left(p_n^{(A)}\right)^2\right\}^2 + \frac{\epsilon_n^{(B)}}{2}\left\{\left(q_n^{(B)}\right)^2 + \left(p_n^{(B)}\right)^2\right\} \\ &+ \frac{\beta}{8}\left\{\left(q_n^{(B)}\right)^2 + \left(p_n^{(B)}\right)^2\right\}^2 + \frac{\epsilon_n^{(C)}}{2}\left\{\left(q_n^{(C)}\right)^2 + \left(p_n^{(C)}\right)^2\right\} + \frac{\beta}{8}\left\{\left(q_n^{(C)}\right)^2 + \left(p_n^{(C)}\right)^2\right\}^2, \\ \mathcal{B} = &\sum_{n=1}^{N} - \left(p_n^{(C)}p_n^{(A)} + q_n^{(C)}q_n^{(A)}\right) - \left(p_n^{(A)}p_n^{(B)} + q_n^{(A)}q_n^{(B)}\right) - \left(p_{n+1}^{(A)}p_n^{(B)} + q_{n+1}^{(A)}q_n^{(B)}\right). \end{aligned} \tag{4.14}$$

Hamiltonian function $\mathcal{A}$ is integrable, however, $\mathcal{B}$ is not integrable and its operator cannot be written explicitly. Therefore, the Hamiltonian function, $\mathcal{B}$, is further split into two parts $\mathcal{P}$ and $\mathcal{Q}$ such that $\mathcal{B} = \mathcal{P} + \mathcal{Q}$ [see [100, 101, 102, 103] for an example on how the three part splitting technique is used for the 1D disordered discrete nonlinear Schrödinger equation (DDNLS)] where

$$\begin{aligned} \mathcal{P} &= -\sum_{n}^{N}\left(p_n^{(A)}p_n^{(B)} + p_n^{(B)}p_n^{(C)} + p_{n+1}^{(B)}p_n^{(C)}\right), \\ \mathcal{Q} &= -\sum_{n}^{N}\left(q_n^{(A)}q_n^{(B)} + q_n^{(B)}q_n^{(C)} + q_{n+1}^{(B)}q_n^{(C)}\right). \end{aligned} \tag{4.15}$$

Since $\mathcal{P}$ and $\mathcal{Q}$ are both integrable, the associated EOM and variational equations are obtained analytically. We therefore can explicitly write the operators $e^{\tau L_{\mathcal{A}}}$, $e^{\tau L_{\mathcal{P}}}$, and $e^{\tau L_{\mathcal{Q}}}$ which will appear in an expression similar to (4.5). These operators are related to the Hamiltonian functions $\mathcal{A}$, $\mathcal{P}$, and $\mathcal{Q}$. The EOM and variational equations for Hamiltonian functions $\mathcal{A}$, $\mathcal{P}$, and $\mathcal{Q}$ are found using (2.8) and (4.10),

respectively. The operators propagate the set of initial conditions $(q_n^{(K)}, p_n^{(K)})$ and a set of initial deviation vectors $(\delta q_n^{(K)}, \delta p_n^{(K)})$ at time t to their final values $(q_n^{'(K)}, p_n^{'(K)})$ and $(\delta q_n^{'(K)}, \delta p_n^{'(K)})$ at time $t+\tau$, respectively. The stub lattice model has the following operator $e^{\tau L_{\mathcal{A}}}$ containing the evolution of the EOM, as well as of the related variational equations.

$$
e^{\tau L_{\mathcal{A}}} : \begin{cases} q_n^{(K)'} & = q_n^{(K)} \cos\left(\alpha_n^{(K)}\tau\right) + p_n^{(K)} \sin\left(\alpha_n^{(K)}\tau\right) \\ p_n^{(K)'} & = p_n^{(K)} \cos\left(\alpha_n^{(K)}\tau\right) - q_n^{(K)} \sin\left(\alpha_n^{(K)}\tau\right) \\ \delta q_n^{(K)'} & = \left(\frac{q_n^{(K)} \cos\left(\alpha_n^{(K)}\tau\right) + p_n^{(K)} \sin\left(\alpha_n^{(K)}\tau\right)}{2J_n^{(K)}} \right) \delta J_n^{(K)} + \\ & \quad \left(p_n^{(K)} \cos\left(\alpha_n^{(K)}\tau\right) - q_n^{(K)} \sin\left(\alpha_n^{(K)}\tau\right) \right) \times \\ & \quad \left(\beta \delta J_n^{(K)} \tau + \delta\alpha_n^{(K)} \right) \\ \delta p_n^{(K)'} & = \left(\frac{p_n^{(K)} \cos\left(\alpha_n^{(K)}\tau\right) - q_n^{(K)} \sin\left(\alpha_n^{(K)}\tau\right)}{2J_n^{(K)}} \right) \delta J_n^{(K)} - \\ & \quad \left(q_n^{(K)} \cos\left(\alpha_n^{(K)}\tau\right) + p_n^{(K)} \sin\left(\alpha_n^{(K)}\tau\right) \right) \times \\ & \quad \left(\beta \delta J_n^{(K)} \tau + \delta\alpha_n^{(K)} \right), \end{cases} \tag{4.16}
$$

when $J_n^{(K)} \neq 0$, i.e., $J_n^{(K)} = \frac{q_n^{(K)(2)} + p_n^{(K)(2)}}{2}$, $\delta J_n^{(K)} = q_n^{(K)} \delta q_n^{(K)} + p_n^{(K)} \delta p_n^{(K)}$ and $\alpha_n^{(K)} = \epsilon_n^{(K)} + \frac{\beta\left(q_n^{(K)(2)} + p_n^{(K)(2)}\right)}{2}$. On the other hand for the special case when $J_n^{(K)} = 0$ we get,

$$
e^{\tau L_{\mathcal{A}}} : \begin{cases} q_n^{(K)'} & = q_n^{(K)} \\ p_n^{(K)'} & = p_n^{(K)} \\ \delta q_n^{(K)'} & = \delta q_n^{(K)} \cos\left(\epsilon_n^{(K)}\tau\right) + \delta p_n^{(K)} \sin\left(\epsilon_n^{(K)}\tau\right) \\ \delta p_n^{(K)'} & = \delta p_n^{(K)} \cos\left(\epsilon_n^{(K)}\tau\right) - \delta q_n^{(K)} \sin\left(\epsilon_n^{(K)}\tau\right). \end{cases} \tag{4.17}
$$

In a similar way, operators $e^{\tau L_{\mathcal{P}}}$ and $e^{\tau L_{\mathcal{Q}}}$ are found to have the form

$$e^{\tau L_{\mathcal{P}}}: \begin{cases} q_n^{(C)\prime} &= q_n^{(C)} - \left(p_n^{(A)}\right)\tau \\ q_n^{(A)\prime} &= q_n^{(A)} - \left(p_n^{(C)} + p_{n-1}^{(B)} + p_n^{(B)}\right)\tau \\ q_n^{(B)\prime} &= q_n^{(C)} - \left(p_n^{(A)} + p_{n+1}^{(A)}\right)\tau \\ p_n^{(C)\prime} &= p_n^{(C)} \\ p_n^{(A)\prime} &= p_n^{(A)} \\ p_n^{(B)\prime} &= p_n^{(B)} \\ \delta q_n^{(C)\prime} &= \delta q_n^{(C)} - \left(\delta p_n^{(A)}\right)\tau \\ \delta q_n^{(A)\prime} &= \delta q_n^{(A)} - \left(\delta p_n^{(C)} + \delta p_{n-1}^{(B)} + \delta p_n^{(B)}\right)\tau \\ \delta q_n^{(B)\prime} &= \delta q_n^{(B)} - \left(\delta p_n^{(A)} + \delta p_{n+1}^{(A)}\right)\tau \\ \delta p_n^{(C)\prime} &= \delta p_n^{(C)} \\ \delta p_n^{(A)\prime} &= \delta p_n^{(A)} \\ \delta p_n^{(B)\prime} &= \delta p_n^{(B)}, \end{cases} \tag{4.18}$$

$$e^{\tau L_{\mathcal{Q}}}: \begin{cases} q_n^{(C)\prime} &= q_n^{(C)} \\ q_n^{(A)\prime} &= q_n^{(A)} \\ q_n^{(B)\prime} &= q_n^{(B)} \\ p_n^{(C)\prime} &= p_n^{(C)} + \left(q_n^{(A)}\right)\tau \\ p_n^{(A)\prime} &= p_n^{(A)} + \left(q_n^{(C)} + q_{n-1}^{(B)} + q_n^{(B)}\right)\tau \\ p_n^{(B)\prime} &= p_n^{(B)} + \left(q_n^{(A)} + q_{n+1}^{(A)}\right)\tau \\ \delta q_n^{(C)\prime} &= \delta q_n^{(C)} \\ \delta q_n^{(A)\prime} &= \delta q_n^{(A)} \\ \delta q_n^{(B)\prime} &= \delta q_n^{(B)} \\ \delta p_n^{(C)\prime} &= \delta p_n^{(C)} + \left(\delta q_n^{(A)}\right)\tau \\ \delta p_n^{(A)\prime} &= \delta p_n^{(A)} + \left(\delta q_n^{(C)} + \delta q_{n-1}^{(B)} + \delta q_n^{(B)}\right)\tau \\ \delta p_n^{(B)\prime} &= \delta p_n^{(B)} + \left(\delta q_n^{(A)} + \delta q_{n+1}^{(A)}\right)\tau. \end{cases} \tag{4.19}$$

Now that we have the tools to evolve the stub lattice model EOM (2.8), we can study the wave packet spreading dynamics. Nevertheless, before doing that, we have to find the best performing symplectic integrator for our system.

4.5 Numerical performance of symplectic integrators

In our study, we numerically integrate the stub lattice EOM (2.8) and variational equations (4.10) using the operators (4.16), (4.17), (4.18), (4.19) using a symplectic integration scheme. The final time, t_f, that would be ideal in order to understand the long time dynamics of the stub lattice model, is of the order $t_f = 10^6$ or $t_f = 10^7$ [82]. These integration times are considered fairly large especially when conducting numerical simulations such as ours which require averaging large numbers of realisations to get accurate statistics. Because of this, the choice of the symplectic integrator that is used in the numerical simulation is important as different SI have varying time performances depending on their order. Since we are numerically integrating the stub lattice model, the obtained solutions will be approximations of the real one, therefore, ideally the choice of the symplectic integration scheme that we will use in our computations should be both very accurate over the simulation time and require low CPU time. Based on these requirements, we compare below the performance of SI of second order (the order of a symplectic integrator refers to the accuracy with which it approximates the solution of a Hamiltonian system while preserving the symplectic structure of the system), in particular the schemes SBAB2 and SABA2, a symplectic integrator of fourth order, the so-called ABA864 integrator, and a symplectic integrator of sixth order which is denoted as, S6. The specific form of these SI are given below.

4.5.1 Symplectic integrators of order 2

We now describe some commonly used second order SI, i.e., the so-called SBAB2 and SABA2 schemes. When split into two integrable parts, SBAB2 is written as

$$\text{SBAB2}(\tau) = e^{d_1\tau L_{\mathcal{A}}} e^{c_2\tau L_{\mathcal{B}}} e^{d_2\tau L_{\mathcal{A}}} e^{c_2\tau L_{\mathcal{B}}} e^{d_1\tau L_{\mathcal{A}}}, \tag{4.20}$$

with coefficients $d_1 = 1/6$, $d_2 = 2/3$ and $c_2 = 1/2$ [104]. Since our operators $e^{\tau L_{\mathcal{A}}}$, $e^{\tau L_{\mathcal{P}}}$, and $e^{\tau L_{\mathcal{Q}}}$ (4.16), (4.17), (4.18), (4.19) are obtained by splitting H as $H = \mathcal{A}+\mathcal{B}$ and with $\mathcal{B} = \mathcal{P} + \mathcal{Q}$, when $e^{\tau L_{\mathcal{B}}}$ is encountered, the SBAB2 scheme is repeated but for operators $e^{\tau L_{\mathcal{P}}}$ and $e^{\tau L_{\mathcal{Q}}}$ such that

$$\begin{aligned}\text{SBAB2}(\tau) = {} & e^{d_1\tau L_{\mathcal{A}}} e^{d_1\cdot c_2\tau L_{\mathcal{P}}} e^{c_2\cdot c_2\tau L_{\mathcal{Q}}} e^{d_2\cdot c_2\tau L_{\mathcal{P}}} e^{c_2\cdot c_2\tau L_{\mathcal{Q}}} e^{d_1\cdot c_2\tau L_{\mathcal{P}}} e^{d_2\tau L_{\mathcal{A}}} e^{d_1\cdot c_2\tau L_{\mathcal{P}}} \\ & \times e^{c_2\cdot c_2\tau L_{\mathcal{Q}}} e^{d_2\cdot c_2\tau L_{\mathcal{P}}} e^{c_2\cdot c_2\tau L_{\mathcal{Q}}} e^{d_1\cdot c_2\tau L_{\mathcal{P}}} e^{d_1\tau L_{\mathcal{A}}},\end{aligned} \tag{4.21}$$

(For all the SI below, when $e^{\tau L_{\mathcal{B}}}$ is encountered, the respective scheme is repeated but for operators $e^{\tau L_{\mathcal{P}}}$ and $e^{\tau L_{\mathcal{Q}}}$ in the same manner as the SBAB2 (4.21) scheme).

The SABA2 integrator has the form

$$\mathrm{SABA2}(\tau) = e^{a_1\tau L_{\mathcal{A}}} e^{b_1\tau L_{\mathcal{B}}} e^{a_2\tau L_{\mathcal{A}}} e^{b_1\tau L_{\mathcal{B}}} e^{a_1\tau L_{\mathcal{A}}}, \tag{4.22}$$

with $a_1 = 1/2 - 1/2\sqrt{3}$, $a_2 = 2/\sqrt{3}$ and $b_1 = 1/2$ [104].

4.5.2 Symplectic integrator of order 4

The fourth order symplectic integrator, ABA864, for Hamiltonian systems which are split into two integrable parts is

$$\begin{aligned}\mathrm{ABA864}(\tau) = {} & e^{a_1\tau L_{\mathcal{A}}} e^{b_1\tau L_{\mathcal{B}}} e^{a_2\tau L_{\mathcal{A}}} e^{b_2\tau L_{\mathcal{B}}} e^{a_3\tau L_{\mathcal{A}}} e^{b_3\tau L_{\mathcal{B}}} \\ & \times e^{a_4\tau L_{\mathcal{A}}} e^{b_4\tau L_{\mathcal{B}}} e^{a_4\tau L_{\mathcal{A}}} e^{b_3\tau L_{\mathcal{B}}} \\ & \times e^{a_3\tau L_{\mathcal{A}}} e^{b_2\tau L_{\mathcal{B}}} e^{a_2\tau L_{\mathcal{A}}} e^{b_1\tau L_{\mathcal{B}}} e^{a_1\tau L_{\mathcal{A}}}.\end{aligned} \tag{4.23}$$

The values of the coefficients $a_1, a_2, a_3, a_4, b_1, b_2, b_3, b_4$ can be found in Table 3 of [105].

4.5.3 Symplectic integrators of order 6

The two-part split sixth order symplectic integrator S6, is given by

$$\mathrm{S6}(\tau) = \mathrm{S2}(w_3\tau)\mathrm{S2}(w_2\tau)\mathrm{S2}(w_1\tau)\mathrm{S2}(w_0\tau)\mathrm{S2}(w_1\tau)\mathrm{S2}(w_2\tau)\mathrm{S2}(w_3\tau), \tag{4.24}$$

where S2 is the SABA2 symplectic integrator (4.22) and the coefficients w_0, w_1, w_2, w_3 are taken from Table 1 of [93].

4.5.4 Computational time performances of symplectic integrators

In order to measure and compare the computational time taken by the SI in Sec. 4.5.1, Sec. 4.5.2 and Sec. 4.5.3, the numerical integration of the stub lattice EOM (2.8) and variational equations (4.10) is performed for a specific initial condition. The initial condition has the following parameters used for the computational runs which include setting the disorder strength to $W = 3.5$, the nonlinearity to $\beta = 0.09$, and final integration time to $t_f = 10^5$. The relative energy error (4.1) of (4.13) is checked at each time step, τ, such that $H_r(t_k) \lesssim 10^{-5}$, similarly to what was required in

[82]. In order to have statistically reliable results, all computational time outcome in this section are averaged values over 10 independent simulations. The numerical simulation, in our study, were performed using the FORTRAN90 coding language. We also note that all simulations were performed at the computer cluster of the Centre for High Performance Computing (CHPC) [106] of South Africa.

The CPU times, t_C, for SBAB2, SABA2, ABA864, and S6 are obtained for a variety of lattice sizes: $N = 500$, $N = 1000$, $N = 1500$, and $N = 2000$. These lattice sizes were chosen because the numerical simulations reported in Chap. 5 required a range of lattice sizes in the interval $N \in [500, 2200]$. The obtained results are shown in Fig. 4.1. For all 4 lattice sizes tested, the ABA864 symplectic integrator performed best as its t_C was the lowest in comparison to the other SI tested. For this reason, the ABA864 symplectic integrator is used for all the results presented in Chap. 5.

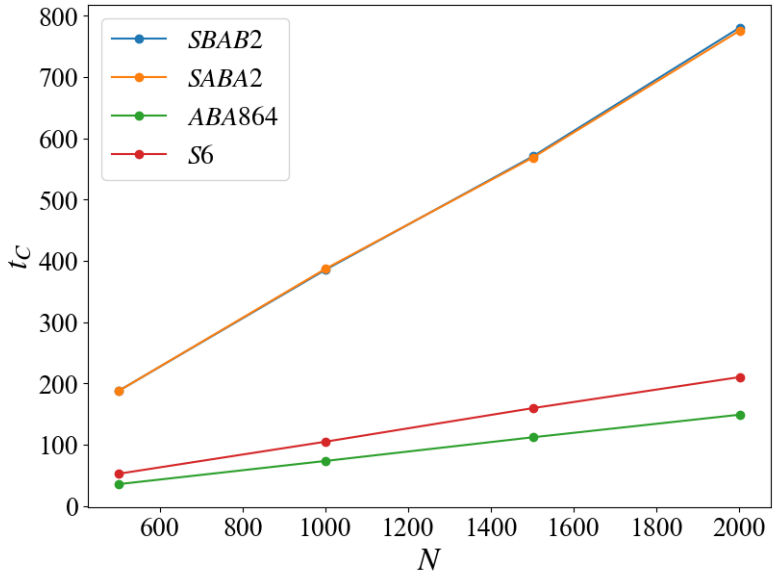

Figure 4.1: A comparison of CPU time, t_C, against lattice size, N, using integration schemes SBAB2 (blue line), SABA2 (orange line), ABA864 (green line), and S6 (red line) for the stub lattice EOM and variational equations. For each integration scheme, the computational time performance is plotted for various lattice sizes N using the following initial condition: final integration time $t_f = 10^5$, $W = 3.5$, and $\beta = 0.09$.

Chapter 5

Numerical investigation of the stub lattice dynamics

In this chapter, we present the outcomes of the numerical study of the stub lattice model. In Sec. 5.1, we introduce the remaining quantities we evaluate in our computations, also explaining how we set up our numerical simulations and providing additional details on these setups. Thereafter, in Sec. 5.2, we present results of wave packet spreading in the stub model lattice for some representative sets of parameter values for each one of the three expected dynamical regimes. Afterwards, in Sec. 5.3, we perform a holistic study of the system's parameter space and provide an overview of the interplay between nonlinearity and disorder on the wave packet dynamics. In this section, we also discuss whether the presence of a band gap affects the wave packet dynamics. Then, in Sec. 5.4, we provide results on whether preserving or destroying the FB affects wave packet dynamics. Finally, in Sec. 5.5, we study how the energy of the wave packet is distributed amongst the subsites of the stub lattice model during the wave packets evolution.

5.1 Computational techniques and model considerations

Let us first define the different quantities that are measured during our numerical simulations. We first note that the stub lattice Hamiltonian (4.13) expressed in generalised positions, $q_n^{(K)}$, and momenta, $p_n^{(K)}$, coordinates, with K denoting subsites

A, B, or C, conserves two quantities, the norm

$$S = \sum_{K} \sum_{n=1}^{N} \frac{1}{2} \left\{ \left(q_n^{(K)} \right)^2 + \left(p_n^{(K)} \right)^2 \right\}, \tag{5.1}$$

and the total energy itself, H (4.13). In our numerical computations, we also evaluate the normalised norm distribution

$$\xi_n = \sum_{K} \frac{\left(q_n^{(K)} \right)^2 + \left(p_n^{(K)} \right)^2}{2S}, \tag{5.2}$$

and the second moment

$$m_2 = \sum_{n=1}^{N} (n - \bar{n}) \xi_n, \tag{5.3}$$

of this distribution, which measures the extent of the wave packet's spreading, with $\bar{n} = \sum_{n=1}^{N} n \xi_n$ being the position of the wave packet's distribution centre. We also use the participation number, P, to measure the number of highly excited sites and to characterise the extent of localisation, which is given by the expression

$$P = \frac{1}{\sum_{n=1}^{N} \xi_n^2}. \tag{5.4}$$

In addition, we compute the finite-time mLE,

$$\Lambda = \frac{1}{t} \ln \frac{||\mathbf{w}(t)||}{||\mathbf{w}(0)||}, \tag{5.5}$$

by implementing the so-called tangent map method [94]. For all these computations, we integrate both the EOM and variational equations of the stub lattice model using the ABA864 [105] symplectic integrator discussed in Chap. 4. Additionally, we calculate the normalised deviation vector distribution (DVD)

$$\xi_n^D(t) = \sum_{K} \left\{ \frac{\left(\delta q_n^{(K)}(t) \right)^2 + \left(\delta p_n^{(K)}(t) \right)^2}{\sum_{n=1}^{N} \left[\left(\delta q_n^{(K)}(t) \right)^2 + \left(\delta p_n^{(K)}(t) \right)^2 \right]} \right\}. \tag{5.6}$$

The DVD can be used to identify where chaoticity is most intense in the wave packet [82]. Typical lattice sizes considered in our study range between $N = 500$ and $N = 2200$. For all our simulations, we set N such that the wave packet does not reach the extreme ends of the lattice for the whole duration of its evolution.

Since the Hamiltonian of the stub lattice model conserves both the norm (5.1) and energy (4.13), we chose integration time steps within the range $\tau \in [0.1, 0.25]$ in order to keep the relative energy error, H_r (4.1), below the threshold of 10^{-5}. In our study, we use fixed boundary conditions, i.e., $q_0^{(K)} = q_{N+1}^{(K)} = p_0^{(K)} = p_{N+1}^{(K)} = 0$. For each considered case, we obtain results averaged over 50 disorder realisations (the computed averaged quantities are indicated by angled brackets, $\langle \cdot \rangle$) with most of the simulations running up to a final integration time of $t_f = 10^7$ time units. Since multiple realisations are considered, the smoothing of the curves describing the time evolution of averaged results is carried out using the locally weighted scatterplot smoothing (LOWESS) method [107]. LOWESS is a method used in regression analysis that creates a smoothed curve through a set of scatter points. LOWESS is a non-parametric method of smooth curve fitting as it does not assume that the data fit some type of distribution. In our study, a typical computational run involves the initial excitation of a block of L lattice unit cells in the centre of a lattice of size N cells. This length of L is chosen such that it matches the localisation volume number ($70/W^2$ in Fig. 3.7) given a disorder strength W for the set of parameters corresponding in each studied case. At every unit cell of the initial block excitation, L, all generalised positions are set to zero, i.e., $q_n^{(K)} = 0$, and all momenta values are chosen in such a way that the total norm at each unit cell is equivalent to $s = 3$, with $p_n^{(K)}$ being randomly chosen between $p_n^{(K)} = +\sqrt{2}$ and $p_n^{(K)} = -\sqrt{2}$. Outside of the initial block excitation region, we set $p_n^{(K)} = q_n^{(K)} = 0$. From the systems parameter space in Fig. 3.8, we chose the parameters β and W in order to study particular cases in the different dynamical regimes while, $\epsilon_n^{(A)}$, $\epsilon_n^{(B)}$, and $\epsilon_n^{(C)}$ in (4.13) are chosen from a random uniform disorder distribution in the interval $[-W/2, W/2]$.

5.2 Representative cases of the different dynamical regimes

5.2.1 Weak chaos

Firstly, let us study the spreading dynamics in the so-called weak chaos regime by exciting L consecutive sites in the middle region of disordered and nonlinear stub lattice model (4.13). For this purposes, we choose the parameter values for our simulations, based on the location of the various regimes in Fig. 3.8. The systems parameter space, depicted in Fig. 3.8 (δ, W) are defined by two quantities, namely the nonlinearity, β which is related to δ, on the vertical axis and disorder strength, W itself, on the horizontal axis. Choosing a combination of β and W values allows

us to set up simulations at specific dynamical regimes. In that spirit, let us consider the following representative weak chaos case,

- $W_{v,2}$: $\beta = 0.02$, $W = 2.46$, $L = 12$,

and average results over 50 disorder realisations to obtain statistically valid results for, $\langle m_2 \rangle$ (5.3), $\langle P \rangle$ (5.4), and $\langle \Lambda \rangle$ (5.5). We present the smoothed values of the time evolution of these three quantities in log-log scale (Figs 5.1 (a), (c) and (e) respectively) so that we can easily estimate the rate of change of each quantity. For example, in the case of $\langle m_2 \rangle$, the rate of change

$$\Gamma_{m_2}(\log_{10} t) = \frac{d \log_{10} \langle m_2 \rangle}{d \log_{10} t}, \tag{5.7}$$

is obtained through a finite difference scheme [79] and the results are shown in Fig 5.1 (b). From this figure we see that asymptotically, a constant rate of change is reached, i.e., Γ_{m_2} tends to become constant implying the eventual validity of power law $\langle m_2 \rangle \propto t^{\Gamma_{m_2}}$. In a similar manner, we compute the rates of change for $\langle P \rangle$ [Fig. 5.1 (c)] and $\langle \Lambda \rangle$ [Fig. 5.1 (e)] and estimate the related power laws [Figs. 5.1 (d) and (f) respectively].

From the results for the weak chaos parameter set $W_{v,2}$ presented in Fig. 5.1, we deduce the existence of the spreading of the initially localised wave packet. This behaviour is reflected on the time evolution of $\langle m_2 \rangle$ in Fig. 5.1 (a), which grows in time especially from $t \gtrsim 10^4$. The spreading is categorised to be subdiffusive since $\Gamma_{m_2} \approx 0.33$ [82] in Fig. 5.1 (b), supporting the validity of the power law $\langle m_2 \rangle \propto t^{0.33}$. In Fig. 5.2 (a), we present the evolution of the norm distribution ξ_n (5.2) for the $W_{v,2}$ case, while in Fig. 5.2 (c), we show three snapshots in time of this distribution. We observe in Fig. 5.2 (a) that ξ_n spreads almost symmetrically around the L initially excited sites at the centre of the lattice, extending to approximately 75 lattice sites to the left and right of L at $t = 10^7$.

The number of highly excited sites also appears to be growing as shown by the time evolution of $\langle P \rangle$ in Fig. 5.1 (c). The rate of change tends to become $\Gamma_P \approx 0.1667$ [82] and is shown in Fig. 5.1 (d) and a power law of $\langle P \rangle \propto t^{0.1667}$ is shown to be eventually achieved in Fig. 5.1 (c). A large part of the norm distributions in Fig. 5.2 (a) is seen remaining close to the region where the initial excitation took place, something which is also seen in Fig. 5.2 (c), where the ξ_n distributions for $\log_{10} t = 3.54$ (black curve), $\log_{10} t = 5.96$ (magenta curve) and $\log_{10} t = 6.48$ (cyan curve), appear to be found close to the lattice centre. The white line in Fig. 5.2 (a), represent the mean position of the ξ_n distribution and is calculated as $\bar{\xi}_n = \sum_{n=1}^{N} n \xi_n$.

This mean position remains close to the lattice centre where the initial excitation took place.

We also study the chaoticity of the stub lattice model by computing Λ (5.5) and present the obtained results in Figs. 5.1 (e) and (f). There results indicate that eventually a power law decay $\langle \Lambda \rangle \propto t^{-0.25}$ (which was also observed in [82] for the DDNLS and KG models) seems to be valid. From the results of Fig. 5.2 (b) where the evolution of the related DVD is shown, we see that the distribution of ξ_n^D (5.6) remains quite localised near the region of initial excitation initially for $t \lesssim 10^4$ [$\bar{\xi}_n^D = \sum_{n=1}^N n \xi_n^D$, indicated by the white curve in Fig. 5.2 (b)] indicating localised chaos. As time evolves ($t \gtrsim 10^4$) the mean position of ξ_n^D [white curve in Fig. 5.2 (b)] fluctuates around the middle of the lattice, something which shows that chaos in the wave packet is somehow moving away from the centre of the lattice. These observations are similar to those found in [81, 82] for the 1D DDNLS and KG models. The fact that $\langle \Lambda \rangle$ decays with a power law $\langle \Lambda \rangle \propto t^{-0.25}$, denotes that there is a decrease in the strength of chaos in the system as time grows. As the wave packet spreads from an initial block excitation [Fig. 5.2 (a)], the system's total norm is shared among more lattice sites and dof, something which results in a decrease in the norm density of the excited sites. Therefore, the strength of the nonlinear terms in (4.13) will decrease, which will result in a decrease in the chaoticity of the whole system.

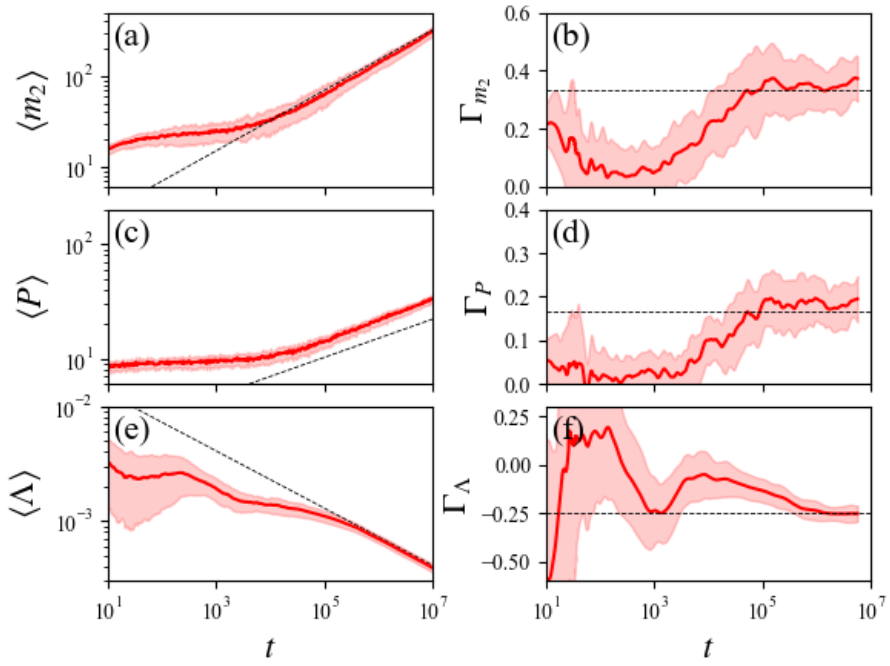

Figure 5.1: (a) Time evolution of $\langle m_2 \rangle$ (5.3) for the $W_{v,2}$ case seen in Fig. 3.8. The simulations are run up to a final time $t_f = 10^7$, and the obtained results are averaged over 50 disorder realisations and smoothed by the LOWESS algorithm. (b) Time evolution of Γ_{m_2} (5.7) estimated from the results of (a) through a finite difference scheme. (c)-(d) are similar to (a)-(b) but for $\langle P \rangle$ (5.4). (e)-(f) are similar to (a)-(b) but for $\langle \Lambda \rangle$ (5.5). The dashed lines indicate the slopes 0.33 in (a) and (b), 0.1667 in (c) and (d), -0.25 in (e) and (f), while the lightly shaded parts denote the statistical error quantified as one standard deviation in the computation of the average quantity.

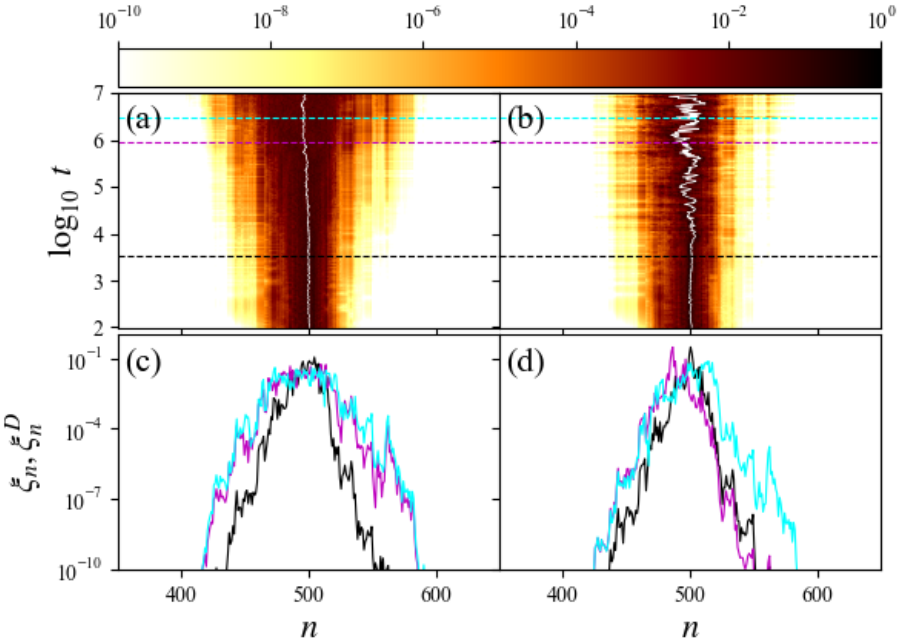

Figure 5.2: (a)-(b) Spatiotemporal evolution of the norm distribution ξ_n (5.2) and the DVD ξ_n^D (5.6), respectively for a simulation for one specific disorder realisation ran up to a final time $t_f = 10^7$ for the case $W_{v,2}$. (c)-(d) show snapshots of ξ_n and ξ_n^D, respectively, at $\log_{10} t = 3.54$ (black curve), $\log_{10} t = 5.96$ (magenta curve), and $\log_{10} t = 6.48$ (cyan curve) corresponding to the similarly coloured dashed horizontal lines in (a) and (b). The white curves in (a) and (b) represent the mean position of ξ_n and ξ_n^D, respectively.

5.2.2 Strong chaos

As a representative case for strong chaos, we consider the parameters in Fig. 3.8 defined as

- $S_{v,7}$: $\beta = 0.4$, $W = 2.46$, $L = 12$.

Figures. 5.3 (a) and (b) show the time evolution of $\langle m_2 \rangle$ (5.3) and the related rate of change Γ_{m_2} for the $S_{v,7}$ case. From Fig. 5.3 (b), we estimate the rate of change of $\langle m_2 \rangle$ to be $\Gamma_{m_2} \approx 0.5$ and the power law $\langle m_2 \rangle \propto t^{0.5}$ is satisfied in Fig. 5.3 (a). Figs. 5.3 (a) and (b) indicate that there is some faster spreading of the initial wave

packet for $S_{v,7}$ than $W_{v,2}$, as $\Gamma_{m_2} \approx 0.5$ in Fig. 5.3 (b) and is greater than $\Gamma_{m_2} \approx 0.33$ obtained in Fig. 5.1 (b). Fig. 5.4 (a) shows the evolution of the ξ_n (5.2) distribution for the $S_{v,7}$ case. In Fig. 5.4 (a), the ξ_n distribution spreads almost symmetrically around the L initially excited sites at the centre of the lattice. We observe that ξ_n in Fig. 5.4 (a) extends approximately 200 lattice sites to the left and right of L at $t = 10^7$.

Figures. 5.3 (c) and (d) show the time evolution of $\langle P \rangle$ (5.4) and the related rate of change Γ_P for the $S_{v,7}$ case. The number of highly excited sites appears to be growing as shown by the time evolution of $\langle P \rangle$ in Fig. 5.3 (c). The rate of change tends to become $\Gamma_P \approx 0.25$ and is shown in Fig. 5.3 (d) and a power law of $\langle P \rangle \propto t^{0.25}$ is shown to be eventually achieved in Fig. 5.3 (c). Comparing Figs. 5.3 (c) and (d) of the $S_{v,7}$ case to Figs. 5.1 (c) and (d) of the $W_{v,2}$ case, we find Γ_P to be higher in the former case. The higher Γ_P indicates that there are more highly excited sites in case $S_{v,7}$ than case $W_{v,2}$ as a result of the faster spreading of the wave packet in $S_{v,7}$. In Fig. 5.4 (a), the norm distribution extends further than in the case of $W_{v,2}$ in Fig. 5.2 (a), reaching 200 lattice sites to the left and right of L at $t = 10^7$ for $S_{v,7}$ instead of only 75 lattice sites to the left and right of L at $t = 10^7$ for $W_{v,2}$. The white line in Fig. 5.4 (a), however, representing the mean position of the ξ_n distribution for the $S_{v,7}$ case, still remains close to the lattice centre where the initial excitation took place like in the $W_{v,2}$ case.

Figures. 5.3 (e) and (f) show the time evolution of $\langle \Lambda \rangle$ (5.5) and the related rate of change Γ_Λ for the $S_{v,7}$ case. The rate of change in Fig. 5.3 (f) is estimated to be $\Gamma_\Lambda \approx -0.3$ and the power law $\langle \Lambda \rangle \propto t^{-0.3}$ in Fig. 5.3 (e) seems to be valid. Comparing the evolution of $\langle \Lambda \rangle$ for $S_{v,7}$ in Figs. 5.3 (e) and (f) to $W_{v,2}$ in Figs. 5.1 (e) and (f), we notice that the decrease in the rate of change of chaos is slower for $S_{v,7}$ than for $W_{v,2}$, indicated by the lower Γ_Λ in the former case, where in Fig. 5.3 (f) the rate of change $\Gamma_\Lambda \approx -0.3$ is satisfied whereas in Fig. 5.1 (f), the rate of change $\Gamma_\Lambda \approx -0.25$ is satisfied. Furthermore, similar to Fig. 5.2 (b), the mean position of ξ_n^D (5.6) [the white line in Fig. 5.4 (b)] initially shows localised chaos near the lattice centre for $t \lesssim 10^3$ but then fluctuates (for $t \gtrsim 10^3$) around the lattice centre showing that chaos in the wave packet is moving away from the centre of the lattice. In Fig. 5.4 (b) (for the $S_{v,7}$ case), the fluctuations start earlier at around $t \gtrsim 10^3$ and has greater variance compared to Fig. 5.2 (b) (for the $W_{v,2}$ case) whose fluctuations start at $t \gtrsim 10^4$.

In Figs. 5.3 (b) and (d), we notice that the rates of change Γ_{m_2} and Γ_P initially reach some maximum value at around $t \approx 10^3$, but as time increases, there is a gradual decrease in both rate of change values. The behaviour of the gradual decreasing rate of change values for Γ_{m_2} and Γ_P have been seen in [79, 86] for the

1D DDNLS and KG systems. The strong chaos is a transient regime and we observe a crossover from strong chaos to weak chaos for $\langle m_2 \rangle$ and $\langle P \rangle$ values [81, 82]. This crossover, however, cannot be observed in the evolution of $\langle \Lambda \rangle$ as shown in Fig. 5.3 (f) [81] where no clear indication of a change in Γ_Λ after $t \approx 10^3$. The reason why Γ_Λ does not show a transient behaviour is that the calculation of Λ contains the entire history of the evolution of the deviation vector (mainly influenced by the strong chaos behaviour), $\mathbf{w}(t)$, and, therefore, Λ is not impacted by slight changes in the dynamics.

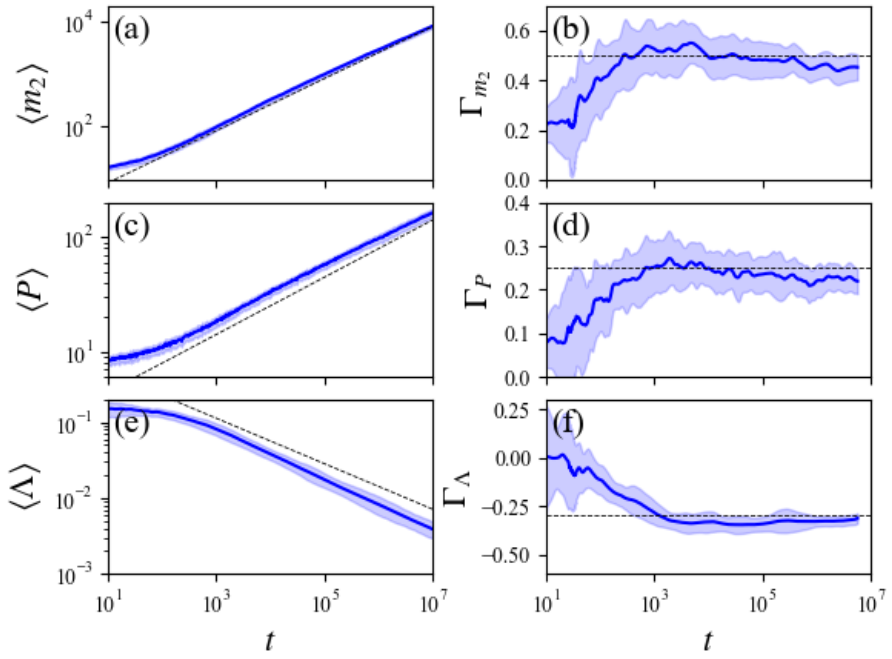

Figure 5.3: Similar to Fig. 5.1 but for the $S_{v,7}$ case. The dashed line indicate the value $\Gamma_{m_2} = 0.5$ in (a) and (b), $\Gamma_P = 0.25$ in (c) and (d) and $\Gamma_\Lambda = -0.3$ in (e) and (f).

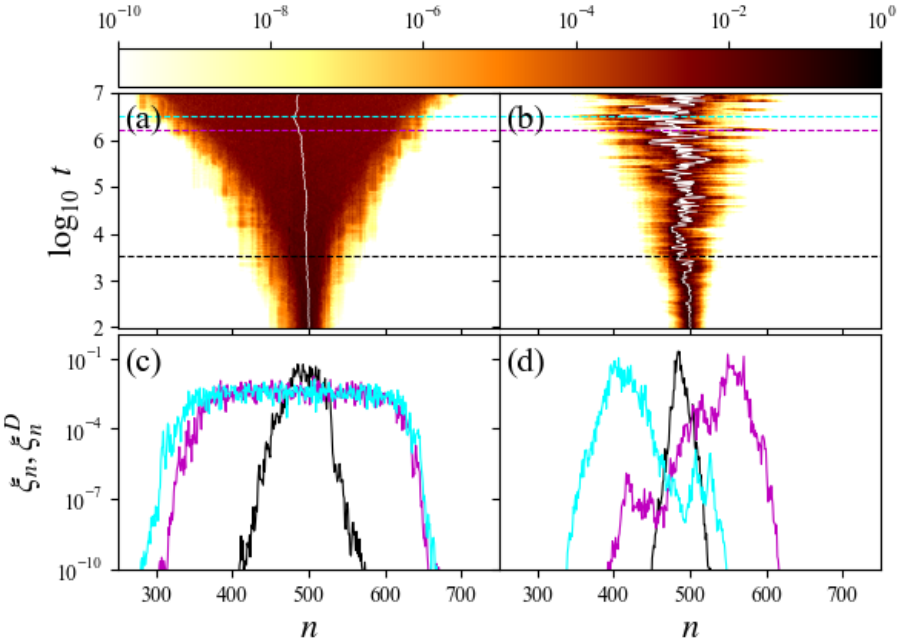

Figure 5.4: Similar to Fig. 5.2 but for the $S_{v,7}$ case. Snapshots in (c)-(d) are at the same times as in Figs. 5.2 (c) and (d).

5.2.3 Self trapping

As a representative case for the self trapping regime in Fig. 3.8, we consider the parameter set defined as

- $T_{v,9}$: $\beta = 15.0$, $W = 2.46$, $L = 1$.

The time evolution of $\langle m_2 \rangle$ (5.3) and the related rate of change Γ_{m_2} for the $T_{v,9}$ case are found in Figs. 5.5 (a) and (b) respectively. In Fig. 5.5 (a), $\langle m_2 \rangle$ evolves with a power law of $\langle m_2 \rangle \propto t^{0.33}$ [78]. In Fig. 5.6 (a), we show the evolution of the ξ_n (5.2) distribution for the self trapping regime defined by the $T_{v,9}$ case. The evolution of ξ_n distribution in Fig. 5.6 (a) and the snapshots of ξ_n in Fig. 5.6 (c) show that the wave packet remains localised around the excitation region.

The time evolution of $\langle P \rangle$ (5.4) and the related rate of change Γ_P for the $T_{v,9}$ case are found in Figs. 5.5 (c) and (d). A particular behaviour unique to the self trapping regime is the continuous localisation of the initial wave packet throughout

the entire duration of the numerical simulation [78]. Unlike the $S_{v,7}$ case in Fig. 5.3 (c) and the $W_{v,2}$ case in Fig. 5.1 (c), the time evolution of $\langle P \rangle$ in Fig. 5.5 (c) indicates no increase over the length of the integration time as $\Gamma_P \approx 0$. As $\langle P \rangle$ is a measure of how many sites are highly excited, since in the self trapping regime an initially localised wave packet will remain localised for the duration of the numerical simulation length, $\langle P \rangle$ will remain at its initial value which is the size of the initial excitation block L. Therefore, in Fig. 5.5 (c), $\langle P \rangle \approx 1$ up to $t = 10^7$.

The time evolution of $\langle \Lambda \rangle$ (5.5) and the related rate of change Γ_Λ for the $T_{v,9}$ case are found in Figs. 5.5 (e) and (f). In Fig. 5.5 (e), $\langle \Lambda \rangle$ decreases but there is no sign of following a particular well defined power law. The self trapping regime also has a characteristic property of having localised chaos which is shown by ξ_n^D (5.6) in Fig. 5.6 (b) and the snapshots [$\log_{10} t = 3.54$ (black curve), $\log_{10} t = 5.96$ (magenta curve) and $\log_{10} t = 6.48$ (cyan curve)] of ξ_n^D in Fig. 5.6 (d). In Figs. 5.6 (b) and (d), the centre of ξ_n and ξ_n^D (white lines) does not fluctuate even at larger times ($t \approx 10^7$).

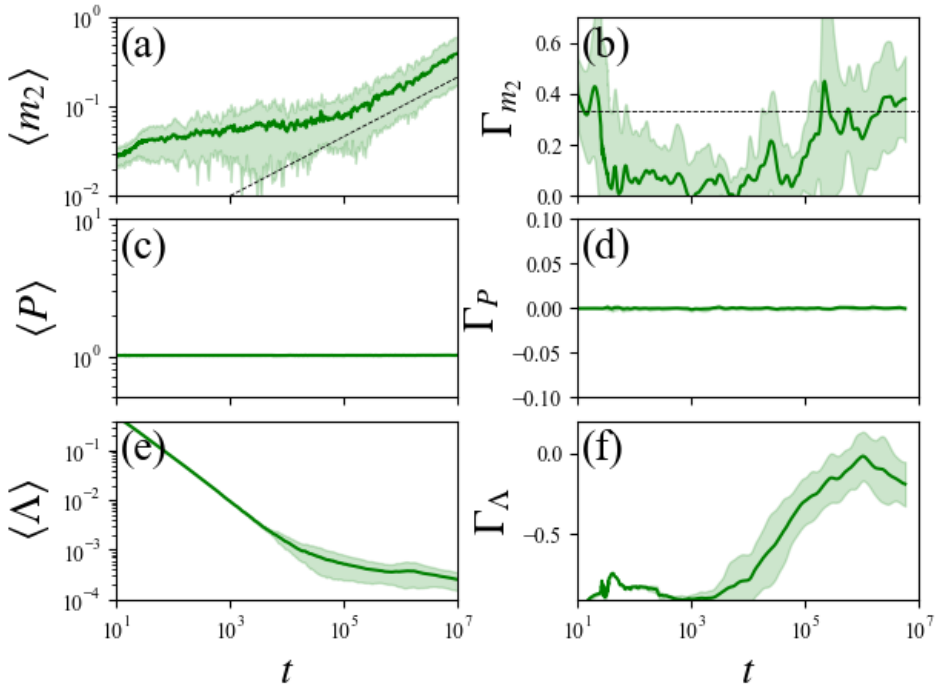

Figure 5.5: Similar to Fig. 5.2 but for the $T_{v,9}$ case. The dashed line indicate the value $\Gamma_{m_2} = 0.33$ in (a) and (b).

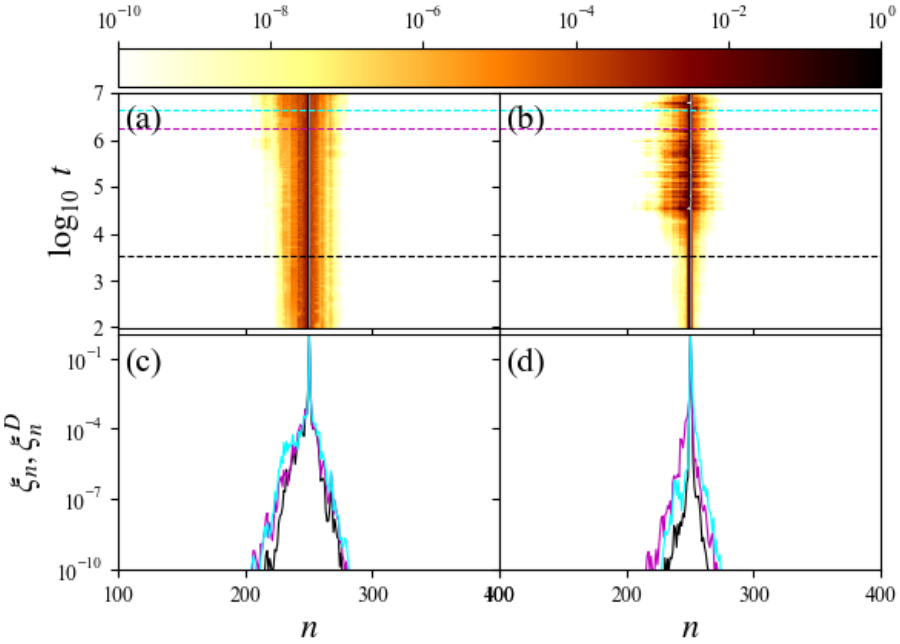

Figure 5.6: Similar to Fig. 5.2 but for the $T_{v,9}$ case. Snapshots in (c)-(d) are at the same times as in Figs. 5.2 (c) and (d).

5.3 Exploration of the system's parameter space

5.3.1 Transition between dynamical regimes

We now consider the wave packet dynamics for many different cases in the parameter space depicted in Fig. 3.8. For this purpose we select parameter sets in a systematic manner in order to understand how nonlinearity, β, and the disorder strength, W, affect the wave packet spreading. The analysis is done by either fixing β or W, and varying the other parameter. In our study, we move vertically through the parameter space of Fig. 3.8 by fixing W and, starting from a low β in the weak chaos regime, we then increase β until we are well inside the strong chaos regime. We also move horizontally through the parameter space, from the weak chaos regime to the strong chaos regime, by fixing β and decreasing W from a high value to a low value.

Let us first investigate the transition between different dynamical regimes by looking

at three sets of parameters which are vertically located in the parameter space of Fig. 3.8 by setting the disorder strength to $W = 2.46$:

- $W_{v,2}$: $\beta = 0.02$, $W = 2.46$, $L = 12$,
- $W_{v,3}$: $\beta = 0.05$, $W = 2.46$, $L = 12$,
- $S_{v,7}$: $\beta = 0.4$, $W = 2.46$, $L = 12$.

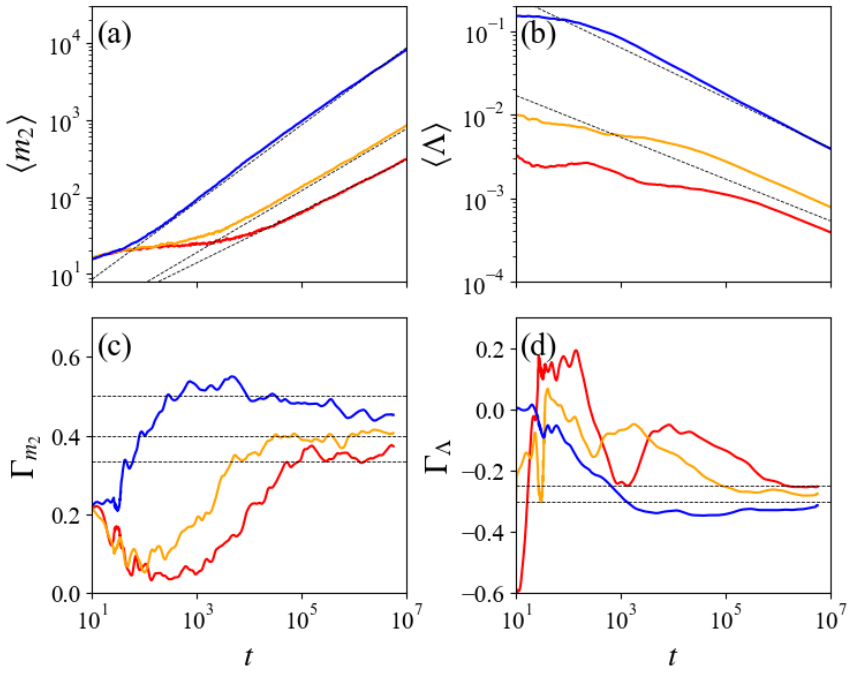

Figure 5.7: (a) Time evolution of $\langle m_2 \rangle$ (5.3) for three sets of parameters $S_{v,7}$ (blue curve), $W_{v,3}$ (orange curve), $W_{v,2}$ (red curve) (see Fig. 3.8). (b) the corresponding time evolution of $\langle \Lambda \rangle$ (5.5) for the same parameter sets given in (a). (c) Time evolution of computed slopes of the $\langle m_2 \rangle$ curves of (a) are in the range $0.33 \lesssim \Gamma_{m_2} \lesssim 0.5$ [top dashed line ($\Gamma_{m_2} \approx 0.5$), middle dashed line ($\Gamma_{m_2} \approx 0.4$), bottom dashed line ($\Gamma_{m_2} \approx 0.33$)]. (d) similar to (c) with the computed slopes of the $\langle \Lambda \rangle$ curves of (b) being in the range $-0.3 \lesssim \Gamma_\Lambda \lesssim -0.25$ [top dashed line ($\Gamma_\Lambda \approx -0.25$), bottom dashed line ($\Gamma_\Lambda \approx -0.3$)]. For these results, $W = 2.46$ and $\beta = 0.02$ for $W_{v,2}$, $\beta = 0.05$ for $W_{v,3}$, and $\beta = 0.4$ for $S_{v,7}$. The results obtained are averaged over 50 disorder realisations and smoothed by the LOWESS algorithm.

We discuss the results of Fig. 5.7 by starting with the parameter set $W_{v,2}$ (red curve in Fig. 5.7) ($W = 2.46$ and $\beta = 0.02$) which is located well inside the weak chaos regime of the parameter space (see Fig. 3.8). In Fig. 5.7 (a), we see that $\langle m_2 \rangle$ (5.3) grows, showing that the wave packet is spreading, in accordance to the discussion of Fig. 5.1 (a) and Fig. 5.2 (a). The wave packet spreading for $W_{v,2}$ follows well the power law $\langle m_2 \rangle \propto t^{0.33}$.

By increasing the nonlinearity to $\beta = 0.4$, we consider the strong chaos case $S_{v,7}$ (blue curve in Fig. 5.7) presented in Fig. 5.3 and discussed in detail in Sec. 5.2.2. For case $S_{v,7}$ we observe faster spreading compared to case $W_{v,2}$ [see Fig. 5.3 (a) and Fig. 5.4 (a)] and a power law $\langle m_2 \rangle \propto t^{0.5}$ is seen to be valid. The final set of parameters in the vertical series of the parameter space points considered here is $W_{v,3}$ (orange curve in Fig. 5.7), which corresponds to $\beta = 0.05$ and is located between points $W_{v,2}$ and $S_{v,7}$, in Fig. 3.8. In this case we again find a power law increase of $\langle m_2 \rangle$, which is characterised by an exponent $\Gamma_{m2} \approx 0.4$ (similarly to what was reported in [75, 108]) being between the values 0.33 and 0.5 respectively observed for cases $W_{v,2}$ and $S_{v,7}$. The time evolution of $\langle \Lambda \rangle$ (5.5) for the $W_{v,2}$, $W_{v,3}$, and $S_{v,7}$ cases follows again an almost power law decay [Fig. 5.7 (b)] with the exponent of the value $W_{v,3}$ case being between the exponents for $W_{v,2}$ and $S_{v,7}$ cases. It is already known that nonlinearity induces spreading [74, 109, 108]. The effect of nonlinearity is seen in Fig. 5.7 (c) where we observe that, in general, an increase in β leads to faster spreading, as shown by the increase of the Γ_{m_2} values as β grows. However, as time evolves, the $\langle m_2 \rangle$ of the strong chaos case, $S_{v,7}$, which has the highest β value of the three sets of parameters, increases faster, something which is reflected to the fact that this case has the largest Γ_{m_2} value among the considered cases. Since the second moment is a measure of the degree of wave packet spreading, Figs. 5.7 (a) and (c) show that as the value of β increases, the spreading of the wave packet becomes faster.

We next consider three other points horizontally located in the parameter space of Fig. 3.8 by fixing the nonlinearity strength to $\beta = 0.25$:

- $W_{h,1}$: $\beta = 0.25$, $W = 5.2$, $L = 3$,
- $W_{h,4}$: $\beta = 0.25$, $W = 3.5$, $L = 6$,
- $S_{h,7}$: $\beta = 0.25$, $W = 2.2$, $L = 15$,

and we conduct similar analyses to the one performed for cases $S_{v,7}$, $W_{v,3}$ and $W_{v,2}$. The outcomes of these studies are reported in Fig. 5.8.

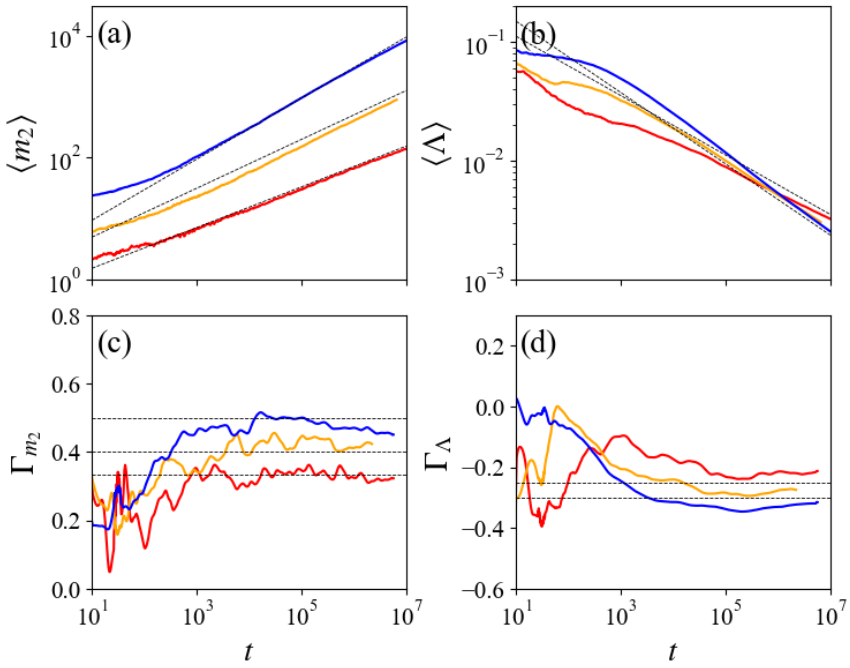

Figure 5.8: (a) Time evolution of $\langle m_2 \rangle$ (5.3) for three sets of parameters $S_{h,7}$ (blue curve), $W_{h,4}$ (orange curve), $W_{h,1}$ (red curve) (see Fig. 3.8). (b) the corresponding time evolution of $\langle \Lambda \rangle$ (5.5) for the same parameter sets given in (a). (c) Time evolution of computed slopes of the $\langle m_2 \rangle$ curves of (a) are in the range $0.33 \lesssim \Gamma_{m_2} \lesssim 0.5$ [top dashed line ($\Gamma_{m_2} \approx 0.5$), middle dashed line ($\Gamma_{m_2} \approx 0.4$), bottom dashed line ($\Gamma_{m_2} \approx 0.33$)]. (d) similar to (c) with the computed slopes of the $\langle \Lambda \rangle$ curves of (b) being in the range $-0.3 \lesssim \Gamma_\Lambda \lesssim -0.25$ [top dashed line ($\Gamma_\Lambda \approx -0.25$), bottom dashed line ($\Gamma_\Lambda \approx -0.3$)]. For these results, $\beta = 0.25$ and $W = 5.2$ for $W_{h,1}$, $W = 3.5$ for $W_{h,4}$, and $W = 2.2$ for $S_{h,7}$. The results obtained are averaged over 50 disorder realisations and smoothed by the LOWESS algorithm.

In Figs. 5.8 (a) and (c), the time evolution of $\langle m_2 \rangle$ (5.3) and the related slope Γ_{m_2} is respectively shown, while in Fig. 5.8 (b) and (d), the time evolution of $\langle \Lambda \rangle$ (5.5) and Γ_Λ is reported for these 3 cases. For the parameter case $W_{h,1}$ (red curve in Fig. 5.8), which has the highest W value ($W = 5.2$), we find that $\langle m_2 \rangle$ eventually follow a power law $\langle m_2 \rangle \propto t^{0.33}$ as shown in Figs. 5.8 (a) and (c), while $\langle \Lambda \rangle$ decreases as of $\langle \Lambda \rangle \propto t^{-0.25}$ [Figs. 5.8 (b) and (d)]. By considering the case $W_{h,1}$ from Fig. 3.8, we observe that this particular parameter set is well within the regime

of weak chaos and therefore behaves similarly to case $W_{v,2}$ discussed in Sec. 5.2.1. For a smaller W value, we get case $W_{h,4}$ (orange curve in Fig. 5.8) having $W = 3.5$. The $W_{h,4}$ point, is closer to the boundary between weak and strong chaos as seen in Fig. 3.8, and is located between points $W_{h,1}$ and $S_{h,7}$ (blue curve in Fig. 5.8). Therefore, we find a behaviour similar to that of case $W_{v,3}$ from the vertical series of cases. Indeed, looking at Figs. 5.8 (c) and (d) we observe that for $W_{h,4}$ case, the $\langle m_2 \rangle$ grows as $\langle m_2 \rangle \propto t^{0.4}$, and $\langle \Lambda \rangle$ exhibits a power law exponent between -0.25 and -0.3. Lowering further the value of W for the horizontal series of cases, we cross from the weak chaos regime to the strong chaos regime, obtaining the $S_{h,7}$ case ($W = 2.2$). In Figs. 5.8 (c) and (d), for $S_{h,7}$ case, the $\langle m_2 \rangle$ grows as $\langle m_2 \rangle \propto t^{0.5}$ and $\langle \Lambda \rangle$ exhibits a power law exponent of -0.3, similar to $S_{v,7}$ found along the vertical series of cases. The general trend is that higher β values induce faster spreading, while higher W values results in stronger localisation of the wave packets. This tendency to induce a localisation effect for a given disorder strength can be seen in the results for Figs. 5.8 (a) and (c). As the case with the lowest W value, $S_{h,7}$, yields the largest exponent for the power law growth of $\langle m_2 \rangle$, and therefore wave packets spread fastest in contrast to the $W_{h,1}$ case, which has the highest W value and consequently the slowest spreading rate.

In Fig. 5.9 (a), we consider cases denoted by the points from Fig. 3.8 and colour each respective point according to their Γ_{m_2} value. In Fig. 5.9 (b), the points are coloured according to their respective Γ_Λ value. In Fig. 5.9 (a), cases such as $W_{v,1}$, $W_{e,5}$, and $W_{e,1}$ show the lowest Γ_{m_2} value of $\Gamma_{m_2} \approx 0.33$ and therefore, the least amount of spreading. The norm distribution of these cases show that a relatively small number of sites are excited. This results to higher chaoticity strengths as they are quantified by $\langle \Lambda \rangle$ value. Fig. 5.9 (b) shows that cases $W_{v,1}$, $W_{e,5}$, and $W_{e,1}$ have $\Gamma_\Lambda \approx -0.25$, which is the highest amongst all cases studied. Transient dynamics which cross over from strong to weak chaos are depicted in Figs. 5.7 (a)-(d) and Figs. 5.8 (a)-(d). The cases which exhibit such transient phases $W_{e,6}$, $W_{e,4}$, and $W_{h,4}$ show $\Gamma_{m_2} \approx 0.4$ while in panel (b), they have $\Gamma_\Lambda \approx -0.275$. In the strong chaos regime, the set of cases, $S_{e,1}$, $S_{v,7}$, and $S_{h,8}$ in Figs. 5.9 (a) and (b) results to $\Gamma_{m_2} \approx 0.5$ and $\Gamma_\Lambda \approx -0.3$ respectively. As expected, the strong chaos regime cases display the largest amount of spreading, indicated by corresponding high Γ_{m_2} values, and the least degree of chaoticity decline, indicated by their low Γ_Λ values. In general, comparing Figs. 5.9 (a) and (b), we observe that there is a general correlation between Γ_{m2} and Γ_Λ values, so that the greater the Γ_{m_2} value of a case is, the lower the Γ_Λ value will be. Cases with a high β and low W display faster wave packet spreading than sets of parameters with low initial β and high W.

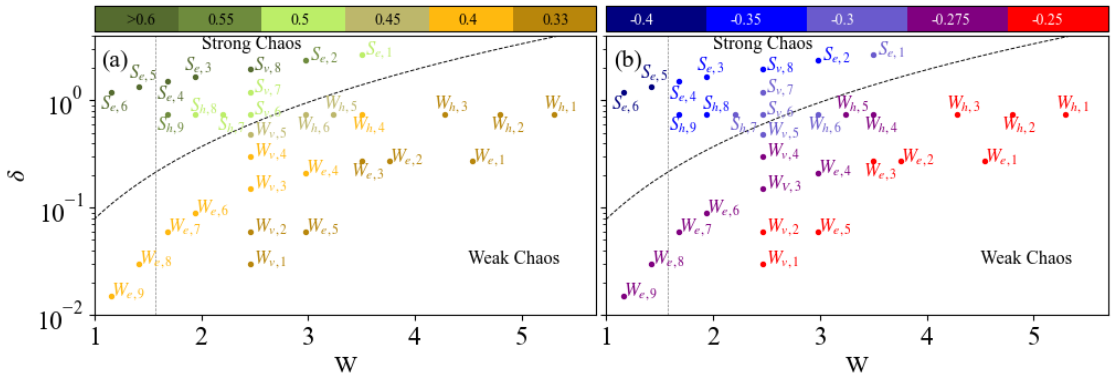

Figure 5.9: A summary of all the parameter sets considered and the respective computed power law exponents of (a) $\langle m_2 \rangle$ (5.3), and (b) $\langle \Lambda \rangle$ (5.5). For each set of parameters we obtain results by averaging our findings of 50 disorder realisations. In all cases the integration final time is $t_f = 10^7$. All points are colour coded according to their respective Γ_{m_2} and Γ_Λ value.

5.3.2 Frequency band gaps and dynamics

In Sec. 3.1 we showed that there exists a bandgap of width, α, in the dispersion relation of the stub lattice model when $W < 1.58$, while the evolution of the frequency spectra and the opening of gaps for decreasing W is shown in Fig. 3.4. Thus, it is interesting to check whether the value of α has an affect on wave packet dynamics of the system. In order to address this question, we consider four weak chaos cases, $W_{e,6}$, $W_{e,7}$, $W_{e,8}$, and $W_{e,9}$, and four strong chaos cases, $S_{e,3}$, $S_{e,4}$, $S_{e,5}$, and $S_{e,6}$ whose location in the systems parameter space can be seen in Fig. 3.8. Cases $W_{e,6}$ and $S_{e,3}$ have $W = 1.94$ and each subsequent cases has a slightly lower W value than the previous cases. As W decreases, we reach a point where it becomes $W < 1.58$, and thereby the system has three distinct frequency bands as discussed in the Chap. 3. In our study, the least computationally possible W value was $W = 1.16$ (Due to the limitations of the computational time available), which is well within the region where gaps are present in the frequency spectrum (Fig. 3.8). The cases considered for the weak chaos regime are:

- $W_{e,6}$: $\beta = 0.03$, $W = 1.94$, $L = 18$,
- $W_{e,7}$: $\beta = 0.02$, $W = 1.68$, $L = 24$,
- $W_{e,8}$: $\beta = 0.01$, $W = 1.42$, $L = 35$,

- $W_{e,9}$: $\beta = 0.005$, $W = 1.16$, $L = 53$,

while the strong chaos one:

- $S_{e,3}$: $\beta = 0.55$, $W = 1.94$, $L = 18$,
- $S_{e,4}$: $\beta = 0.5$, $W = 1.68$, $L = 24$,
- $S_{e,5}$: $\beta = 0.45$, $W = 1.42$, $L = 35$,
- $S_{e,6}$: $\beta = 0.4$, $W = 1.16$, $L = 53$.

Taking a look at Figs. 5.10 (a) and (c), which show the time evolution of $\langle m_2 \rangle$ (5.3) and Γ_{m_2}, for the weak chaos cases, $W_{e,6}$ (red curve in Fig. 5.10), $W_{e,7}$ (orange curve in Fig. 5.10), $W_{e,8}$ (green curve in Fig. 5.10), and $W_{e,9}$ (blue curve in Fig. 5.10), we understand that, the wave packets second moment eventually evolve following the power law $\langle m_2 \rangle \propto t^{0.4}$. A point to note in Fig. 5.10 (c) is that the dynamics of case $W_{e,9}$, which has the lowest W value among the studied cases, takes the longest time to reach this power law at $t \approx 10^7$. On the other hand, in the $W_{e,6}$ case, which has the highest W value, shows the power law of $\langle m_2 \rangle \propto t^{0.4}$ requires the least time ($t \approx 10^5$) to be established. Although the time it takes to reach the power law of $\langle m_2 \rangle \propto t^{0.4}$ varies between the weak chaos cases $W_{e,6}$, $W_{e,7}$, $W_{e,8}$, and $W_{e,9}$, the eventual outcome is the same for all studied cases, as seen in Fig. 5.10 (c). Moreover, there appears to be no difference between cases such as $W_{e,9}$ and $W_{e,8}$ which correspond to cases where the frequency spectra have gaps ($\alpha > 0$), and $W_{e,7}$ and $W_{e,6}$ for which no gap is present. From Figs. 5.10 (b) and (d), which show the evolution of $\langle \Lambda \rangle$ (5.5) for the $W_{e,6}$, $W_{e,7}$, $W_{e,8}$, and $W_{e,9}$ cases, we see that as we move from W values for which gaps are not present to W values for which a gap is formed, $\langle \Lambda \rangle$ always follows a power law decay ($\langle \Lambda \rangle \propto t^{-0.25}$). Once again the cases with the highest W value ($W_{e,9}$) requires the longest time to clearly establish the power law $\langle \Lambda \rangle \propto t^{-0.25}$. From the results of Fig. 5.10, we also conclude that the final power laws of $\langle m_2 \rangle$ and $\langle \Lambda \rangle$ don't differ much between cases $W_{e,6}$, $W_{e,7}$, $W_{e,8}$, and $W_{e,9}$ and that the presence of a gap does not affect the wave packet spreading of weak chaos cases with $W > 1.16$ up to a final time considered ($t_f = 10^7$).

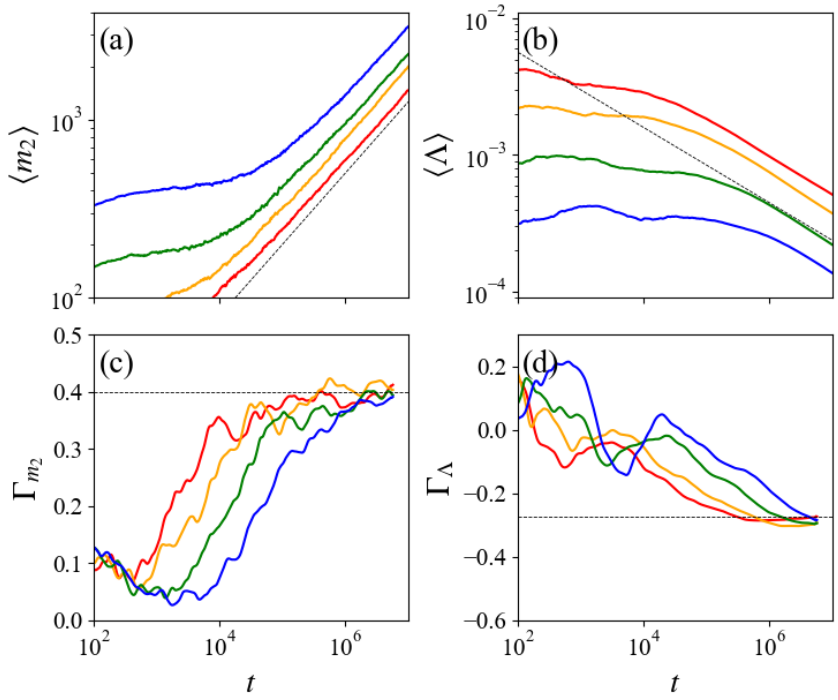

Figure 5.10: Similar to Fig. 5.7 but for cases $W_{e,6}$ (red curve), $W_{e,7}$ (orange curve), $W_{e,8}$ (green curve), and $W_{e,9}$ (blue curve). The exponents of $\langle m_2 \rangle$ (5.3) and $\langle \Lambda \rangle$ (5.5) are estimated to eventually be 0.4 and -0.25 respectively [see panels (c)-(d)].

The results for the cases $S_{e,3}$ (red curve in Fig. 5.11), $S_{e,4}$ (orange curve in Fig. 5.11), $S_{e,5}$ (green curve in Fig. 5.11), and $S_{e,6}$ (blue curve in Fig. 5.11) are presented in Fig. 5.11. In Fig. 5.11 (c), for the cases $S_{e,3}$, $S_{e,4}$, $S_{e,5}$, and $S_{e,6}$, Γ_{m_2} at $t_f = 10^7$ appears to be still decreasing when the final integration time is reached. The maximum Γ_{m_2} value is reached for the $S_{e,6}$ case, which has the lowest W value ($W = 1.16$), reaches $\Gamma_{m_2} \approx 0.7$. The maximum Γ_{m_2} value of $S_{e,3}$, which has the highest W value ($W = 1.94$), reaches $\Gamma_{m_2} \approx 0.6$. The cases $S_{e,4}$ and $S_{e,5}$ have maximum Γ_{m_2} values between $\Gamma_{m_2} \approx 0.7$ and $\Gamma_{m_2} \approx 0.6$. In Fig. 5.11 (d), a similar observation is noted for Γ_Λ, where the minimum Γ_Λ of the case $S_{e,6}$ reaches $\Gamma_\Lambda \approx -0.5$, while the minimum Γ_Λ of the case $S_{e,3}$ reaches $\Gamma_\Lambda \approx -0.4$. In the case of Fig. 5.11 (d), Γ_Λ for the four cases, appears to be still increasing when the final integration time is reached. Since these cases are in the region of greatest spreading in Fig. 3.8, given that the β value is high and the W value is low, these cases would

require more computational time to obtain a clear asymptotic behaviour for the time evolution of $\langle m_2 \rangle$ and $\langle \Lambda \rangle$. The cases of $S_{e,3}$ and $S_{e,4}$, which are strong chaos cases when band gaps are not present in the frequency spectrum, evolve in a similar manner to the cases $S_{e,5}$ and $S_{e,6}$, which are strong chaos cases when gaps are present in the frequency spectrum. In both Figs. 5.11 (c) and (d), the cases $S_{e,3}$, $S_{e,4}$, $S_{e,5}$, and $S_{e,6}$ all show a similar evolution shape as Γ_{m_2} and Γ_Λ reach some maximum Γ_{m_2} and minimum Γ_Λ value before decreasing and increasing, respectively. Although more computational time is required, the strong chaos results found in Fig. 5.11 indicate that the presence of the band gap appears to have no affect on the wave packet dynamics for strong chaos cases.

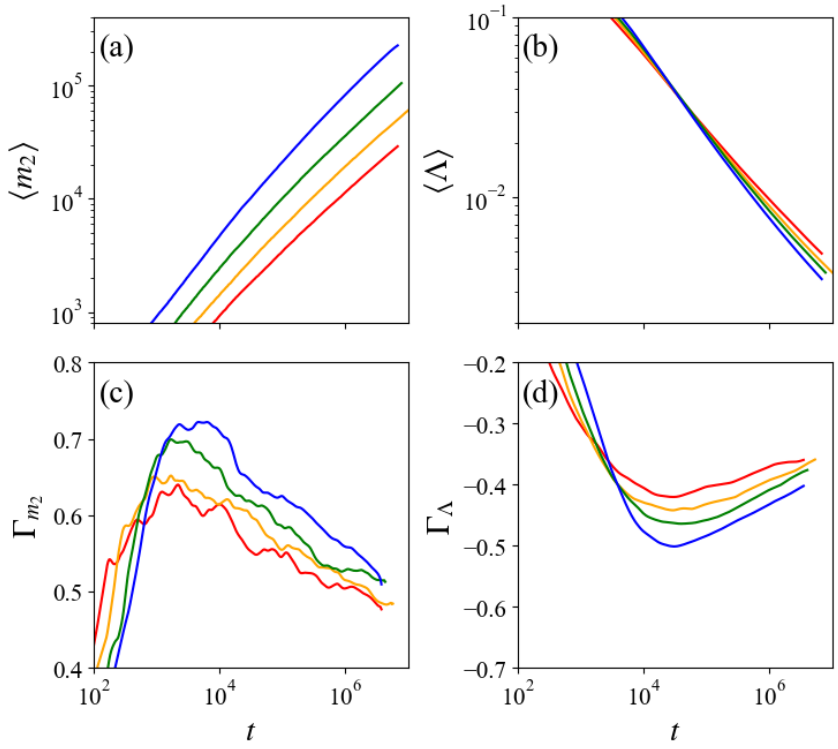

Figure 5.11: Similar to Fig. 5.7 but for the cases $S_{e,3}$ (red curve), $S_{e,4}$ (orange curve), $S_{e,5}$ (green curve), and $S_{e,6}$ (blue curve).

5.4 Dynamics of the disordered system when the flatband is preserved

In Sec. 3.1.1, we discussed a way of placing symmetric onsite energies with disorder such that the FB in Fig. 3.2 is preserved. Results in Sec. 5.2 and Sec. 5.3 involved placing the onsite energies [$\epsilon_n^{(K)}$ in (4.13) with K being subsites A, B or C], on all three subsites, where $\epsilon_n^{(K)}$ was chosen randomly from an uniform disorder distribution in the interval $[-W/2, W/2]$. Let us recall from Sec. 3.1.1, that in order to preserve the FB even in the presence of disorder, onsite energies values (on subsite B and C in Fig. 3.1) need to be symmetrical. In our study, we set $\epsilon_n^{(B)} = \epsilon_n^{(C)} = 0$ and $\epsilon_n^{(A)}$ randomly chosen in the interval $\epsilon_n^{(A)} \in [-W/2, W/2]$ to obtain the frequency spectrum results presented in Fig. 3.6. We take the case $W_{v,2}$, whose results are presented in Fig. 5.1 and Fig. 5.2, and using the particular onsite energy configuration to preserve the FB, we obtain the case $\overline{W}_{v,2}$, which is the $W_{v,2}$ case but with the FB preserved. The case $\overline{W}_{v,2}$ corresponds to the following set of parameters

- $\overline{W}_{v,2}$: $\beta = 0.02$, $W = 2.46$, $L = 12$.

Figures. 5.12 (a) and (b) respectively show the time evolution of $\langle m_2 \rangle$ (5.3) as well as Γ_{m_2} for the $\overline{W}_{v,2}$ case. The rate of change tends to become $\Gamma_{m_2} \approx 0.33$ and is shown in Fig. 5.12 (b) and a power law of $\langle m_2 \rangle \propto t^{0.33}$ is shown to be eventually achieved in Fig. 5.12 (a). Comparing Figs. 5.1 (a) and (b) (results for $W_{v,2}$) to Figs. 5.12 (a) and (b), $\langle m_2 \rangle$ evolves with the same power law of $\langle m_2 \rangle \propto t^{0.33}$. Comparing the spatiotemporal evolution of the ξ_n (5.2) distribution for the $\overline{W}_{v,2}$ case shown in Fig. 5.13 (a) to that of the $W_{v,2}$ case in Fig. 5.2 (a), we notice that in Fig. 5.13 (a), ξ_n extends around 250 lattice sites to the left and right of the excitation block, L, while ξ_n in Fig. 5.2 (a) extends only around 75 lattice sites to the left and right of the initial excitation block.

Figures. 5.12 (c) and (d) show the time evolution of $\langle P \rangle$ (5.4) as well as the related rate of change Γ_P for the $\overline{W}_{v,2}$ case. In Figs. 5.12 (c) and (d), $\langle P \rangle$ evolves with a power law $\langle P \rangle \propto t^{0.2}$, which is different from $\langle P \rangle \propto t^{0.1667}$ observed for $W_{v,2}$ in Figs. 5.1 (c) and (d). As the $\overline{W}_{v,2}$ case has onsite energies only on subsite A, the overall participation number (5.4) will be higher than that of the participation number in $W_{v,2}$ which has onsite energies on subsite A, B, and C. Therefore, the overall effect of the W value is less for $\overline{W}_{v,2}$ which results in a higher participation number (see Fig. 3.7).

Figures. 5.12 (e) and (f) show the time evolution of $\langle \Lambda \rangle$ (5.5) as well as Γ_Λ for the $\overline{W}_{v,2}$ case. The time evolution of the $\langle \Lambda \rangle$ in Fig. 5.12 (e) and (f) shows that $\langle \Lambda \rangle$ evolves with a power law of $\langle \Lambda \rangle \propto t^{-0.25}$, which is the same power law as in

Figs. 5.1 (e) and (f) (for the $W_{v,2}$ case). In Fig. 5.13 (b), the fluctuations of the mean position $\bar{\xi}_n^D$ (the white line) are similar to those found in Fig. 5.2 (b). Comparing the fluctuations of $\bar{\xi}_n^D$ in Fig. 5.13 (b) and in Fig. 5.2 (b), in Fig. 5.13 (b) the fluctuations start earlier at $t \gtrsim 10^{3.5}$ rather than $t \gtrsim 10^4$ of Fig. 5.2 (b). The fluctuations of $\bar{\xi}_n^D$ in Fig. 5.13 (b) also show greater variance than those of Fig. 5.2 (b).

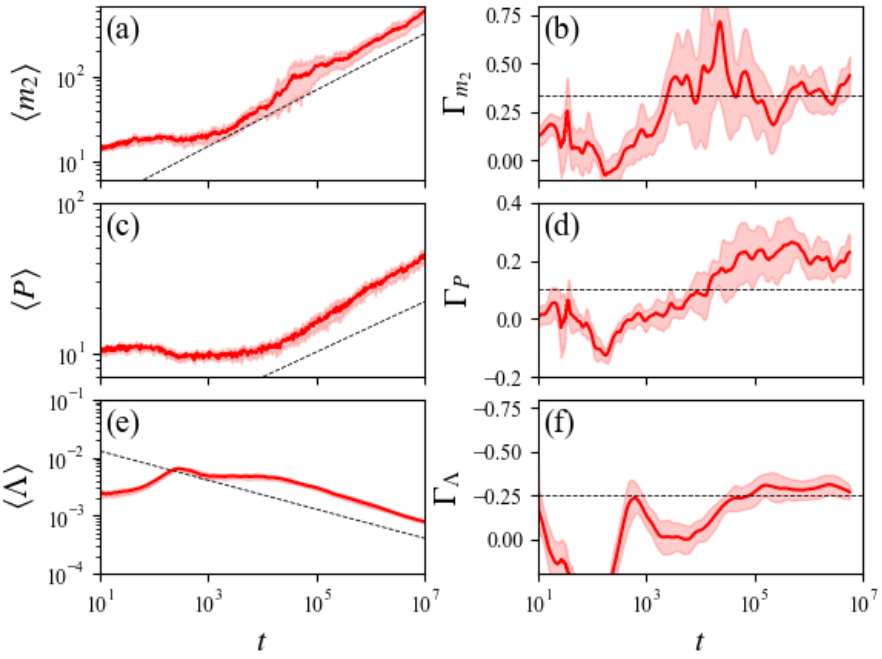

Figure 5.12: Similar to Fig. 5.1 but for the case $\overline{W}_{v,2}$. The dashed line indicate the value $\Gamma_{m_2} = 0.33$ in (a) and (b), $\Gamma_P = 0.1667$ in (c) and (d) and $\Gamma_\Lambda = -0.25$ in (e) and (f).

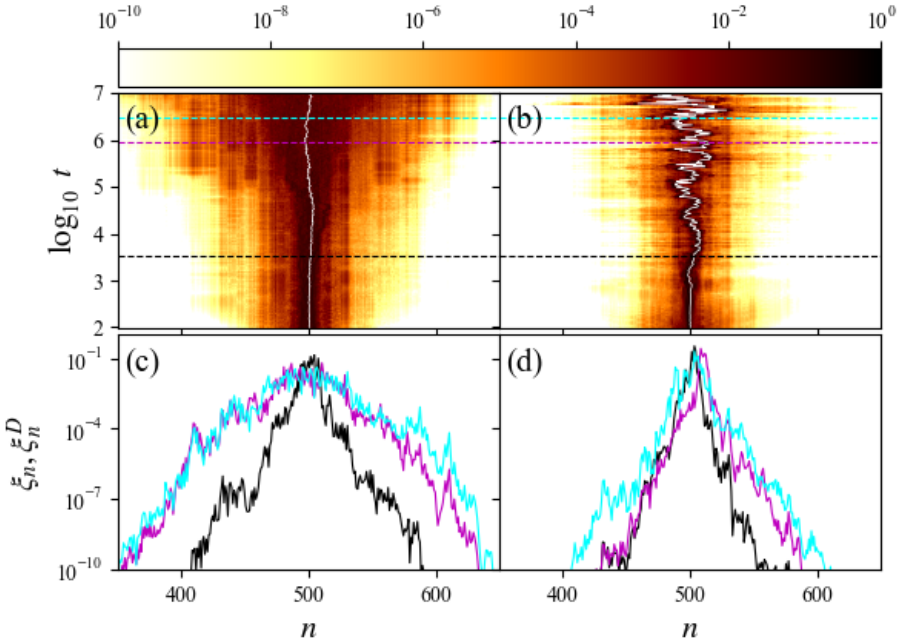

Figure 5.13: Similar to Fig. 5.2 but for the case $\overline{W}_{v,2}$. Snapshots in (c)-(d) are at the same times as in Figs. 5.2 (c) and (d).

5.5 Energy polarisation

In the final part of this chapter we investigate the polarisation of energy among subsites. As the wave packet ξ_n (5.2) spreads [Fig. 5.2 (a) and Fig. 5.4 (a)], more unit cells of the stub lattice are excited. In that context, it is worth checking how ξ_n is distributed among the subsites of the excited unit cells and investigate if the number of inter- and intra-site connections a subsite has will affect the part of ξ_n which is in each subsite. In order to study the distribution of ξ_n within a unit cell of the stub lattice, we use ξ_n (5.2) to determine $\xi_n^{(K)}$, which is the normalised norm distribution at each subsite of a unit cell,

$$\xi_n^{(K)} = \sum_{n=1}^{N} \frac{\left(q_n^{(K)}\right)^2 + \left(p_n^{(K)}\right)^2}{2S}, \tag{5.8}$$

and define the distributions

$$\xi_{LHS}^{(K)} = \sum_{n=1}^{L} (\xi_n^{(K)} / \sum_K \sum_{n=1}^{L} \xi_n^{(K)}),$$
$$\xi_{RHS}^{(K)} = \sum_{n=L}^{N} (\xi_n^{(K)} / \sum_K \sum_{n=L}^{N} \xi_n^{(K)}), \tag{5.9}$$

where K denotes subsites A, B, or C. We calculate the left hand side (LHS) normalised norm distribution ($\xi_{LHS}^{(K)}$) of a subsite, which tells us what proportion of ξ_n will be at subsite K on the LHS of the initial excitation region and in a similar way we define the right hand side (RHS) normalised norm distribution ($\xi_{RHS}^{(K)}$). Both distributions, $\xi_{LHS}^{(K)}$ and $\xi_{RHS}^{(K)}$, are calculated at every time step of our simulation. Fig. 5.14 provides a visual representation of where in the lattice the distribution $\xi_{LHS}^{(K)}$ and $\xi_{RHS}^{(K)}$ are considered. The two representative cases, $W_{v,2}$ and $S_{v,7}$ discussed in Sec. 5.2.1 and Sec. 5.2.2, respectively, are used to determine the time evolution of the polarisation of ξ_n among subsites A, B, and C.

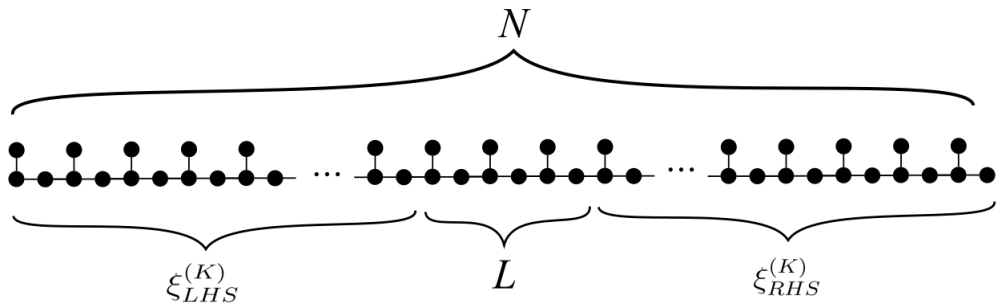

Figure 5.14: A schematic diagram showing which lattice sites are considered for the computation of $\xi_{LHS}^{(K)}$ and $\xi_{RHS}^{(K)}$ (5.9) with L denoting the lattice region where the initial excitation was located.

Firstly, we consider the results of $\xi_{LHS}^{(K)}$ and $\xi_{RHS}^{(K)}$ for the $W_{v,2}$ case (Fig. 5.15). In Fig. 5.15 (a), the evolution of $\xi_{LHS}^{(A)}$, $\xi_{LHS}^{(B)}$, and $\xi_{LHS}^{(C)}$ reach an equilibrium among the subsites towards the end of the integration ($t = 10^7$) with the values of $\xi_{LHS}^{(A)}$, $\xi_{LHS}^{(B)}$, and $\xi_{LHS}^{(C)}$ eventually being around 33% of the total norm ξ_n (5.2). A similar conclusion can be reached from the results in Fig. 5.15 (b) for the RHS part. For the LHS wave packet, initially ξ_n is concentrated on subsites B as for $t \lesssim 10^4$, $\xi_{LHS}^{(B)}$ contains around 40% of ξ_n while each one of $\xi_{LHS}^{(A)}$ and $\xi_{LHS}^{(C)}$ have around 30%. From the results of Fig. 5.15 (b), which shows the RHS parts, we see that for $t \lesssim 10^4$,

the highest part of the norm is concentrated on subsites A, as $\xi^{(A)}_{RHS}$ contains around 40% of the distribution, while $\xi^{(B)}_{RHS}$ and $\xi^{(C)}_{RHS}$ have around 30% each. By comparing Figs. 5.15 (a) and (b), we note that the subsite with the highest percentage of ξ_n within a site is different for the LHS and RHS part. From the schematic of the stub lattice model in Fig. 3.1, we see that the excitation on the LHS will first encounter subsite B of a unit cell, while on the RHS it will first reach subsite A. Therefore, in the initial phases of the evolution when ξ_n starts to spread, $\xi^{(B)}_{LHS}$ and $\xi^{(A)}_{RHS}$ will contain most of the norm. As time evolves and the wave packet propagates further in both the LHS and RHS, the proportions on $\xi^{(K)}_{LHS}$ and $\xi^{(K)}_{RHS}$ start to equalise.

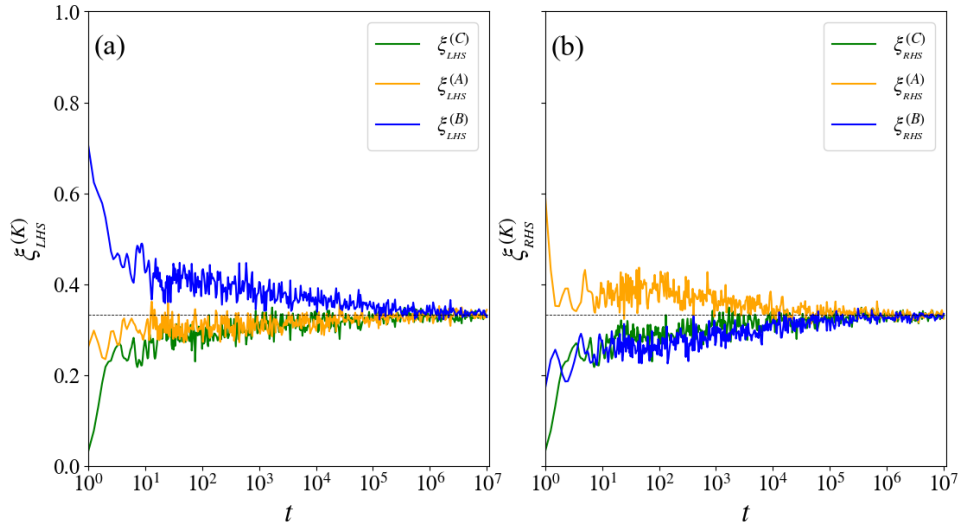

Figure 5.15: Energy polarisation. The evolution of (a) $\xi^{(K)}_{LHS}$ (5.9) and (b) $\xi^{(K)}_{RHS}$ (5.9) for the case $W_{v,2}$, with K representing subsites A, B or C, over a time integration up to $t_f = 10^7$. In (a) we show $\xi^{(A)}_{LHS}$ (orange curve), $\xi^{(B)}_{LHS}$ (blue curve) and $\xi^{(C)}_{LHS}$ (green curve). The same colours are used for plots in (b) but for RHS. Dashed lines in (a) and (b) denote the value 0.33.

In Fig. 5.16, the $\xi^{(K)}_{LHS}$ and $\xi^{(K)}_{RHS}$ for the $S_{v,7}$ case is shown. Much like the behaviour in Figs. 5.15 (a) and (b), in Figs. 5.16 (a) and (b), the evolution of $\xi^{(A)}_{LHS}$, $\xi^{(B)}_{LHS}$, and $\xi^{(C)}_{LHS}$ and $\xi^{(A)}_{RHS}$, $\xi^{(B)}_{RHS}$, and $\xi^{(C)}_{RHS}$ reach equilibrium among the subsites [eventually each being around 33% of the total norm ξ_n (5.2)] towards the end of the integration at $t = 10^7$. Comparing the polarisation of total norm ξ_n on the LHS and RHS in the $S_{v,7}$ case to that of the $W_{v,2}$ case, the equilibrium distribution is reached quicker in

Figs. 5.16 (a) and (b) (at $t \gtrsim 10^3$) than in Figs. 5.15 (a) and (b) (at $t \gtrsim 10^6$). The less time taken to reach equilibrium, is due to the faster wave packet spreading of the $S_{v,7}$ case (discussed in Sec. 5.2.2). In Fig. 5.16 (a), before a state of equilibrium is reached ($t \lesssim 10^3$), $\xi^{(B)}_{LHS}$ contains most of ξ_n (around 40%). A similar pattern emerges for Fig. 5.16 (b), where $\xi^{(C)}_{RHS}$ and $\xi^{(A)}_{RHS}$ each contains most of ξ_n for $t \lesssim 10^3$. Like the $W_{v,2}$ case, the spreading of the wave packet in the $S_{v,7}$ case means that the excitation on the LHS will first encounter subsite B of an unit cell and, therefore, $\xi^{(B)}_{LHS}$ will contain most of the norm in the initial phase ($t \lesssim 10^3$). On the RHS, the excitation will first encounter subsite A first, meaning $\xi^{(A)}_{RHS}$ contains most of the norm when $t \lesssim 10^3$. However, as the wave packet is spreading faster, both $\xi^{(A)}_{RHS}$ and $\xi^{(C)}_{RHS}$ accumulate a high proportion of the norm.

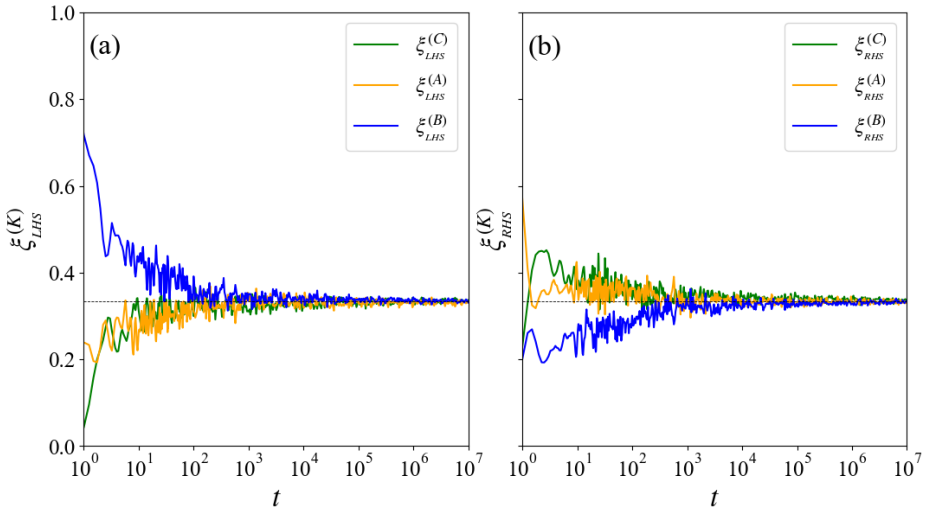

Figure 5.16: Similar plots to Fig. 5.15 but for the case $S_{v,7}$.

Chapter 6

Summary and conclusions

In our study, we numerically investigated the wave packet dynamics and chaotic behaviour of a simple tight-binding lattice model exhibiting FBs, the so-called the stub lattice model. In particular, we investigated how disorder, nonlinearity, and the presence of gaps in the frequency spectrum of the system affect the chaoticity and spreading dynamics of wave packets.

After a general introduction to the topic of the thesis in Chap. 1 and a concise presentation of various aspects of Hamiltonian, and lattice dynamical system, along with the notion of chaos in Chap. 2, we introduced, in Chap. 3, the linear stub lattice model Hamiltonian (3.1), showing that its frequency spectrum consists of a FB ($\omega = 0$) and two dispersive bands ($\omega \pm \sqrt{3 + 2\cos q}$) separated by a bandgap of width α. We also discussed how introducing disorder leads to AL, and the destruction of the FB, with the size of the bandgap shrinking as the disorder strength increased. We also discussed the spreading of initially localised wave packets in the model, and establishing the existence of different dynamical regimes in an appropriately chosen parameter space of the model (i.e., the weak chaos, strong chaos, and self trapping regimes). Then, in Chap. 4, we presented a general overview of the various numerical techniques we use in our study.

The main results of our work are presented in Chap. 5. To explore the wave packet dynamics of the stub lattice model, we use the ABA864 symplectic integrator to integrate the systems EOM and its variational equations. In order to study the wave packet evolution, we compute in Sec. 5.1 the second moment, m_2 (5.3), of the systems norm to quantify the spreading extent, while the degree of localisation is characterised by using the wave packets participation number, P (5.4). The chaoticity of the system was quantified through the computation of the finite-time mLE, Λ (5.5). Using all these quantities, we described in Sec. 5.2 the basic features of

the weak, strong, and self trapping regimes. The strong chaos regime showed faster spreading as $\langle m_2 \rangle$ (averaged results over several disorder realisations) eventually showed a growth described by $\langle m_2 \rangle \propto t^{0.5}$, while for the weak chaos regime, the estimated power law growth was shown to be $\langle m_2 \rangle \propto t^{0.33}$. Additionally, in terms of the system's chaoticity, our results, for both the strong and weak regimes, showed a decaying chaos strength indicated by the power laws $\langle \Lambda \rangle \propto t^{-0.3}$ and $\langle \Lambda \rangle \propto t^{-0.25}$, respectively. Moreover, in Sec. 5.3.1, fixing either the nonlinearity parameter β or the disorder strength W and varying the other parameter, we investigated the transition between different dynamical regimes, which is reflected on the computed values of the various power law exponents, which varied as $0.33 < \Gamma_{m_2} < 0.5$, while $-0.3 < \Gamma_{\Lambda} < -0.25$. Our work shows that wave packet spreading in the stub lattice model is subdiffusive for the weak and strong chaos regimes while no spreading occurs for the self trapping regime. Furthermore, the faster the wave packet spreads, the slower its chaoticity declines. Through a holistic investigation of the system's parameter space, we showed that the increase of nonlinearity results to faster spreading while the increase of the disorder strength is shown to favor the localisation of wave packets.

In Sec. 5.3.2, an analysis of the effect of the bandgap on the spreading of wave packets was performed by varying the values of W for both the weak and strong chaos regimes. Before band gap closure, the weak chaos studied case showed a second moment power law increase $\langle m_2 \rangle \propto t^{0.4}$ and an mLE power law decay according to $\langle \Lambda \rangle \propto t^{-0.25}$. On the other hand, the weak chaos cases exhibited power laws $\langle m_2 \rangle \propto t^{0.4}$ and $\langle \Lambda \rangle \propto t^{-0.25}$ when there was no band gap present. A similar analysis was done in the strong chaos regime, however, due to computational limitations, as longer then $t = 10^7$ simulations were needed, a conclusive asymptotic behaviour of both $\langle m_2 \rangle$ and $\langle \Lambda \rangle$ was not established. Our study shows that the presence of a gap in the frequency spectrum does not affect the spreading dynamics of weak chaos cases for $W > 1.16$.

In Sec. 5.4, particular disorder configurations which preserve the FBs were considered. By comparing two weak chaos cases, one with onsite energies that preserve the FB with another which does not, we showed that the second moment grows as $\langle m_2 \rangle \propto t^{0.33}$, while the finite time mLE decreases as $\langle \Lambda \rangle \propto t^{-0.25}$ in both cases. A difference between the two cases appeared with respect to the wave packets participation number P, which showed a power law increase $\langle P \rangle \propto t^{0.2}$ when the FB was preserved followed by a different power law growth ($\langle P \rangle \propto t^{0.1667}$) when the FB was destroyed. The difference in the exponents of these power laws was possibly due to the way in which we configured our onsite energies to preserve the FB. Thus, our investigation showed that whether the FB is maintained or destroyed, the

wave packets spreading is characterised by the same power law growth of the second moment, i.e., $\langle m_2 \rangle \propto t^{0.33}$, as well as the same evolution of the finite time mLE, $\langle \Lambda \rangle \propto t^{-0.25}$, for the weak chaos regime.

Finally, in Sec. 5.5, the time evolution of the norm distribution, ξ_n (5.2), of the wave packet within subsites of the stub lattice model was discussed. Our results showed that in the weak chaos and strong chaos regimes, the wave packet moving to the left of the initial excitation (encountering subsite B of the next unit cell first), and the part moving to the right (initially encountering subsite A of the next unit cell) exhibited some differences in their behaviour. More specifically, we identified an initial phase of the evolution during which there was an uneven distribution of ξ_n amongst the subsites of the unit cells. In particular, subsite B on the LHS of the initially excited part of the lattice had around 40% of the norm moving left, whereas subsite A and C on the LHS of the initial excitation had, each one of them around 30% of the ξ_n moving left. A similar observation was made for the right moving wave packet, where subsite A on the RHS had around 40% of the ξ_n moving right, while each subsite B and C on the RHS of the initially excited part of the lattice had around 30% of the ξ_n moving right. However, these uneven distributions of the norm reached equilibrium amongst subsites towards the end of the integration. Therefore, our study shows that given enough time, the wave packets norm will become evenly distributed amongst subsites of the stub lattice model.

As a final remark we note that future investigations could consider further numerical studies of the dynamical behaviour of initially localised wave packets in the strong chaos regime when frequency band gaps are present, as our results in Sec. 5.3.2 are rather inconclusive due to the limitations in the available computational resources. Furthermore, a similar analysis to the one performed here can be also done for other lattice models exhibiting a FB, such as the pyrochlore ladder lattice or the diamond lattice.

Bibliography

[1] A. S. Davydov. "Solitons and energy transfer along protein molecules". *J. Theor. Biol.* **66**, 379, 1977.

[2] F. V. Kusmartsev and E. I. Rashba. "Self-Trapping in crystals and nonlinear wave processes: Self-Trapping barrier for plasma caviton". *Zh. Eksp. Teor. Fiz.* **84**, 2064, 1983.

[3] S. L. Mccall and P. M. Pltazman. "Microwave propagation in two-dimensional dielectric lattices". *Phys. Rev. Lett.* **67**, 2017, 1991.

[4] M. I. Molina. "Nonlinear surface impurity in a semi-infinite lattice". *Phys. Rev. B.* **71**, 035404, 2005.

[5] M. Segev, T. Schwartz, G. Bartal, and S. Fishman. "Transport and Anderson localization in disordered two-dimensional photonic lattices". *Nature* **446**, 52, 2007.

[6] M. Inguscio, G. Roati, C. D'Errico, L. Fallani, M. Fattori, C. Fort, M. Zaccanti, G. Modugno, and M. Modugno. "Anderson localization of a non-interacting Bose-Einstein condensate". *Nature* **453**, 895, 2008.

[7] S. Flach and A. V. Gorbach. "Discrete breathers—advances in theory and applications". *Phys. Rep.* **467**, 1, 2008.

[8] Y. V. Kartashov, B. A. Malomed, and L. Torner. "Solitons in nonlinear lattices". *Rev. Mod. Phys.* **83**, 247, 2011.

[9] N. I. Karachalios, P. Kyriazopoulos, and K. Vetas. "The Lefever–Lejeune nonlinear lattice: Convergence dynamics and the structure of equilibrium states". *Phys. D. Nonlinear Phenom.* **409**, 132487, 2020.

[10] I. V. Andrianov, V. V. Danishevskyy, and G. Rogerson. "Vibrations of nonlinear elastic lattices: low-and high-frequency dynamic models, internal resonances and modes coupling". *Proc. R. Soc.* **476**, 20190532, 2020.

[11] J. C. Eilbeck, P. S. Lomdahl, and A. C. Scott. "The discrete self-trapping equation". *Phys. D. Nonlinear Phenom.* **16**, 318, 1985.

[12] L. Proville. "Quantum breathers in a nonlinear Klein Gordon lattice". *Phys. D. Nonlinear Phenom.* **216**, 191, 2006.

[13] E. Michaely and S. Fishman. "Effective noise theory for the nonlinear Schrödinger equation with disorder". *Phys. Rev. E.* **85**, 046218, 2012.

[14] A. A. Ovchinnikov, N. S. Erikhman, and K. A. Pronin. *Vibrational-rotational excitations in nonlinear molecular systems*. Springer Science & Business Media, 2001.

[15] P. G. Kevrekidis. *The discrete nonlinear Schrödinger equation: mathematical analysis, numerical computations and physical perspectives*. Springer Science & Business Media, 2009.

[16] J. M. Luck. "Scaling laws for weakly disordered 1D flat bands". *J. Phys. A. Math.* **52**, 205301, 2019.

[17] P. W. Anderson. "Absence of diffusion in certain random lattices". *Phys. Rev.* **109**, 1492, 1958.

[18] A. Coutant, A. Sivadon, L. Zheng, V. Achilleos, O. Richoux, G. Theocharis, and V. Pagneux. "Acoustic Su-Schrieffer-Heeger lattice: Direct mapping of acoustic waveguides to the Su-Schrieffer-Heeger model". *Phys. Rev. B.* **103**, 224309, 2021.

[19] B. M. Manda, V. Achilleos, O. Richoux, Ch. Skokos, and G. Theocharis. "Wave-packet spreading in the disordered and nonlinear Su-Schrieffer-Heeger chain". *Phys. Rev. B.* **107**, 184313, 2023.

[20] B. Sutherland. "Localization of electronic wave functions due to local topology". *Phys. Rev. B.* **34**, 5208, 1986.

[21] A. Mielke. "Ferromagnetism in the Hubbard model on line graphs and further considerations". *J. Phys.* **24**, 3311, 1991.

[22] H. Tasaki. "Ferromagnetism in the hubbard models with degenerate single-electron ground-states". *Phys. Rev. Lett.* **69**, 1608, 1992.

[23] H. Tasaki. "Stability of ferromagnetism in the Hubbard model". *Phys. Rev. Lett.* **73**, 1158, 1994.

[24] J. Vidal, R. Mosseri, and B. Douçot. "Aharonov-Bohm cages in two-dimensional structures". *Phys. Rev. Lett.* **81**, 5888, 1998.

[25] C. Naud, G. Faini, and D. Mailly. "Aharonov-Bohm cages in 2D normal metal networks". *Phys. Rev. Lett.* **86**, 5104, 2001.

[26] J. Schnack, H. J. Schmidt, J. Richter, and J. Schulenburg. "Independent magnon states on magnetic polytopes". *Eur. Phys. J. B.* **24**, 475, 2001.

[27] J. Schulenburg, A. Honecker, J. Schnack, J. Richter, and H. J. Schmidt. "Macroscopic magnetization jumps due to independent magnons in frustrated quantum spin lattices". *Phys. Rev. Lett.* **88**, 167207, 2002.

[28] J. Richter, J. Schulenburg, A. Honecker, J. Schnack, and H. Schmidt. "Exact eigenstates and macroscopic magnetization jumps in strongly frustrated spin lattices". *J. Condens. Matter Phys.* **16**, S779, 2004.

[29] T. Jacqmin, I. Carusotto, I. Sagnes, M. Abbarchi, D. D. Solnyshkov, G. Malpuech, E. Galopin, A. Lemaitre, J. Bloch, and A. Amo. "Direct observation of Dirac cones and a flatband in a honeycomb lattice for polaritons". *Phys. Rev. Lett.* **112**, 116402, 2014.

[30] F. Baboux, L. Ge, T. Jacqmin, M. Biondi, E. Galopin, A. Lemaitre, L. Le Gratiet, I. Sagnes, S. Schmidt, H. E. Tureci, A. Amo, and J. Bloch. "Bosonic Condensation and Disorder-Induced Localization in a Flat Band". *Phys. Rev. Lett.* **116**, 066402, 2016.

[31] S. Weimann, L. Morales-Inostroza, B. Real, C. Cantillano, A. Szameit, and R. A. Vicencio. "Bulk and edge transport in Sawtooth lattices". *Opt. Lett.* **41**, 2414, 2016.

[32] A. Ramachandran, A. Andreanov, and S. Flach. "Chiral flat bands: Existence, engineering, and stability". *Phys. Rev. B.* **96**, 161104, 2017.

[33] R. A. Vincencio. "Photonic flat band dynamics". *Adv. Phys.: X.* **6**, 1878057, 2021.

[34] F. Diebel, D. Leykam, M. Boguslawski, P. Rose, C. Denz, and A. S. Desyatnikov. "All-optical switching in optically induced nonlinear waveguide couplers". *Appl. Phys. Lett.* **105**, 99901, 2014.

[35] S. Mukherjee, A. Spracklen, D. Choudhury, N. Goldman, P. Öhberg, E. Andersson, and R. R. Thomson. "Observation of a localized flat-band state in a photonic Lieb lattice". *Phys. Rev. Lett.* **114**, 245504, 2015.

[36] E. Travkin, F. Diebel, and C. Denz. "Compact flat band states in optically induced flatland photonic lattices". *Appl. Phys. Lett.* **111**, 2017.

[37] C. Danieli, A. Andreanov, and S. Flach. "Many-body flatband localization". *Phys. Rev. B.* **102**, 041116, 2020.

[38] N. Perchikov and O. V. Gendelman. "Flat bands and compactons in mechanical lattices". *Phys. Rev. E.* **96**, 052208, 2017.

[39] R. Shen, L. B. Shao, B. Wang, and D. Y. Xing. "Single Dirac cone with a flat band touching on line-centered-square optical lattices". *Phys. Rev. B.* **81**, 041410, 2010.

[40] R. A. Vicencio, C. Cantillano, L. Morales-Inostroza, B. Real, C. Mejía-Cortés, S. Weimann, A. Szameit, and M. I. Molina. "Observation of localized states in Lieb photonic lattices". *Phys. Rev. Lett.* **114**, 245503, 2015.

[41] S. Xia, A. Ramachandran, S. Xia, D. Li, X. Liu, L. Tang, Y. Hu, D. Song, J. Xu, D. Leykam, S. Flach, and Z. Chen. "Unconventional flatband line states in photonic Lieb lattices". *J. Opt.* **121**, 263902, 2018.

[42] W. X. Qiu, S. Li, J. H. Gao, Y. Zhou, and F. C. Zhang. "Designing an artificial Lieb lattice on a metal surface". *Phys. Rev. B.* **94**, 241409, 2016.

[43] R. Drost, T. Ojanen, A. Harju, and P. Liljeroth. "Topological states in engineered atomic lattices". *Nature* **13**, 668, 2017.

[44] X. Letartre, C. Seassal, C. Grillet, P. Rojo-Romeo, P. Viktorovitch, M. d'Yerville, D. Cassagne, and C. Jouanin. "Group velocity and propagation losses measurement in a single-line photonic-crystal waveguide on InP membranes". *Appl. Phys. Lett.* **79**, 2312, 2001.

[45] W. Maimaiti. "Flatband generators". PhD thesis. University of Science and Technology, Basic Science, 2019.

[46] M. Röntgen, C. V. Morfonios, and P. Schmelcher. "Compact localized states and flat bands from local symmetry partitioning". *Phys. Rev. B.* **97**, 035161, 2018.

[47] J. D. Bodyfelt, D. Leykam, C. Danieli, X. Yu, and S. Flach. "Flatbands under correlated perturbations". *Phys. Rev. Lett.* **113**, 236403, 2014.

[48] C. Danieli, J. D. Bodyfelt, and S. Flach. "Flatband engineering of mobility edges". *Phys. Rev. B.* **91**, 235134, 2015.

[49] A. R. Kolovsky, A. Ramachandran, and S. Flach. "Topological flat Wannier-Stark bands". *Phys. Rev. B.* **97**, 045120, 2018.

[50] M. Johansson, U. Naether, and R. A. Vicencio. "Compactification tuning for nonlinear localized modes in sawtooth lattices". *Phys. Rev. E.* **92**, 032912, 2015.

[51] P. P. Belicev, G. Gligoric, A. Maluckov, M. Stepic, and M. Johansson. "Quantum sensing close to a dissipative phase transition: Symmetry breaking and criticality as metrological resources". *Phys. Rev. A.* **96**, 013817, 2017.

[52] D. Leykam, J. D. Bodyfelt, A. S. Desyatnikov, and S. Flach. "Localization of weakly disordered flat band states". *Eur. Phys. J. B.* **90**, 1, 2017.

[53] S. Flach, D. Leykam, J. D. Bodyfelt, P. Matthies, and A. S. Desyatnikov. "Detangling flat bands into Fano lattices". *EPL* **105**, 1, 2014.

[54] M. V. Ivanchenko, T. V. Laptyeva, and S. Flach. "Anderson localization or nonlinear waves: a matter of probability". *J. Phys. A. Math.* **47**, 493001, 2014.

[55] D. Leykam, A. Andreanov, and S. Flach. "Artificial flat band systems: From lattice models to experiments". *Adv. Phys.: X.* **3**, 1473052, 2018.

[56] Y. Hatsugai. "Revisiting flat bands and localization". *Ann. Phys.* **435**, 168453, 2021.

[57] L. Perko. *Differential equations and dynamical systems*. Springer, 1996.

[58] M. Brin. *Introduction to dynamical systems*. Cambridge University Press, 2002.

[59] W. Tian. "PETREL19: a new numerical solution of planetary and lunar ephemeris". *Celest. Mech. Dyn. Astron.* **135**, 38, 2023.

[60] B. W. Montague. *Basic Hamiltonian mechanics*. CERN, 1993.

[61] M. Jeffs. *Classical mechanics and symplectic geometry*. Harvard University Press, 2022.

[62] I. M. Gelfand. *Calculus of variations*. Prentice-Hall, 1963.

[63] H. Poincaré. *Les méthodes nouvelles de la mécanique céleste*. Paris, 1892.

[64] E. N. Lorenz. "Deterministic nonperiodic flow". *J. Atmos. Sci.* **20**, 130, 1963.

[65] R. Devaney. *An introduction to chaotic dynamical systems, second edition*. Avalon Publishing, 1989.

[66] R. J. Bell. "The dynamics of disordered lattices". *Rep. Prog. Phys.* **35**, 1315, 1972.

[67] J. Tidholm. *Lattice dynamics: From fundamental research to practical applications*. Linköping University Electronic Press, 2020.

[68] N. Ashcroft and D. Mermin. "Bloch's theorem". *Solid State Phys.*, 133, 1976.

[69] D. S. Wiersma, P. Bartolini, A. Lagendijk, and R. Righini. "Localization of light in a disordered medium". *Nature* **390**, 671, 1997.

[70] R. L. Weaver. "Localization of ultrasound in a three-dimensional elastic network". *Wave Motion* **12**, 129, 1990.

[71] C. Dembowski, H. Gräf, H. L. Harney, A. Heine, W. D. Heiss, H. Rehfeld, and A. Richter. "Experimental observation of the topological structure of exceptional points". *Phys. Rev. Lett.* **86**, 787, 2001.

[72] Y. Lahini, A. Avidan, F. Pozzi, M. Sorel, R. Morandotti, D. N. Christodoulides, and Y. Silberberg. "Anderson localization and nonlinearity in one-dimensional disordered photonic lattices". *Phys. Rev. Lett.* **100**, 013906, 2008.

[73] J. Billy, V. Josse, Z. Zuo, A. Bernard, B. Hambrecht, P. Lugan, D. Clément, L. Sanchez-Palencia, P. Bouyer, and A. Aspect. "Direct observation of Anderson localization of matter waves in a controlled disorder". *Nature* **453**, 891, 2008.

[74] S. Flach, D. O. Krimer, and Ch. Skokos. "Universal spreading of wave packets in disordered nonlinear systems". *Phys. Rev. Lett.* **102**, 024101, 2009.

[75] A. S. Pikovsky and D. L. Shepelyansky. "Destruction of Anderson localization by a weak nonlinearity". *Phys. Rev. Lett.* **100**, 094101, 2008.

[76] G. Kopidakis, S. Komineas, S. Flach, and S. Aubry. "Absence of wave packet diffusion in disordered nonlinear systems". *Phys. Rev. Lett.* **100**, 084103, 2008.

[77] F. Evers and A. D. Mirlin. "Anderson transitions". *Rev. Mod. Phys.* **80**, 1355, 2008.

[78] Ch. Skokos, D. O. Krimer, S. Komineas, and S. Flach. "Delocalization of wave packets in disordered nonlinear chains". *Phys. Rev. E.* **79**, 056211, 2009.

[79] T. V. Laptyeva, J. D. Bodyfelt, D. O. Krimer, Ch. Skokos, and S. Flach. "The crossover from strong to weak chaos for nonlinear waves in disordered systems". *EPL* **91**, 30001, 2010.

[80] Ch. Skokos and S. Flach. "Spreading of wave packets in disordered systems with tunable nonlinearity". *Phys. Rev. E.* **82**, 016208, 2010.

[81] Ch. Skokos, I. Gkolias, and S. Flach. "Nonequilibrium chaos of disordered nonlinear waves". *Phys. Rev. Lett.* **111**, 064101, 2013.

[82] B. Senyange, B. Many Manda, and Ch. Skokos. "Characteristics of chaos evolution in one-dimensional disordered nonlinear lattices". *Phys. Rev. E.* **98**, 052229, 2018.

[83] B. M. Manda. "Nonlinear dynamics and chaos in multidimensional disordered Hamiltonian systems". PhD thesis. University of Cape Town, Department of Mathematics and Applied Mathematics, 2021.

[84] B. Kramer and A. MacKinnon. "Localization: theory and experiment". *Rep. Prog. Phys.* **56**, 1469, 1993.

[85] I. Gkolias. "Chaos in 1-dimensional nonlinear disordered lattices". MA thesis. Aristotle University of Thessaloniki, School of Science, Physics Department, 2013.

[86] T. V. Laptyeva, J. D. Bodyfelt, and S. Flach. "Subdiffusion of nonlinear waves in two-dimensional disordered lattices". *EPL* **98**, 60002, 2012.

[87] D. O. Krimer and S. Flach. "Statistics of wave interactions in nonlinear disordered systems". *Phys. Rev. E.* **82**, 046221, 2010.

[88] B. Senyange. "Chaotic behaviour of disordered nonlinear lattices". PhD thesis. University of Cape Town, Department of Mathematics, 2021.

[89] J. Sanz-Serna. "Symplectic integrators for Hamiltonian problems: An overview". *Acta. Numer.* **1**, 243, 1992.

[90] H. A. Luther. "An explicit sixth-order Runge-Kutta formula". *Math. Comput.* **22**, 434, 1968.

[91] B. A. Shadwick, J. C. Bowman, and PJ. Morrison. "Exactly conservative integrators". *SIAM. Rev. Soc. Ind. Appl. Math.* **59**, 1112, 1998.

[92] B. Senyange and Ch. Skokos. "Computational efficiency of symplectic integration schemes: application to multidimensional disordered Klein-Gordon lattices". *Eur. Phys. J.: Spec. Top.* **227**, 625, 2018.

[93] H. Yoshida. "Construction of higher order symplectic integrators". *Phys. Lett. A.* **150**, 262, 1990.

[94] Ch. Skokos and E. Gerlach. "Numerical integration of variational equations". *Phys. Rev. E.* **82**, 036704, 2010.

[95] Ch. Skokos, G. Gottwald, and J. Laskar. "Chaos detection and predictability". *Lect. Notes Phys., Vol. 915*, 2016.

[96] Ch. Skokos. "The Lyapunov Characteristic Exponents and their computation". *Lect. Notes Phys., Vol. 790*, 2010.

[97] V. D. Pechuk, T. S. Krasnopolskaya, and E. D. Pechuk. *Maximum Lyapunov Exponent Calculation*. Springer International Publishing, 2022.

[98] D. Lai and G. Chen. "Statistical analysis of Lyapunov exponents from time series: A Jacobian approach". *Math. and Comp. Model.* **27**, 1, 1998.

[99] G. Benettin, L. Galgani, A. Giorgilli, and J. M. Strelcyn. "Lyapunov characteristic exponents for smooth dynamical systems and for Hamiltonian systems - A method for computing all of them." *Meccanica* **15**, 1, 1980.

[100] J. D. Bodyfelt, T. V. Laptyeva, Ch. Skokos, D. O. Krimer, and S. Flach. "Nonlinear waves in disordered chains: Probing the limits of chaos and spreading". *Phys. Rev. E.* **84**, 016205, 2011.

[101] C. Danieli, B. M. Manda, M. Thudiyangal, and Ch. Skokos. "Computational efficiency of numerical integration methods for the tangent dynamics of many-body Hamiltonian systems in one and two spatial dimensions". *Math. eng.* **1**, 447, 2018.

[102] E. Gerlach, J. Meichsner, and Ch. Skokos. "On the symplectic integration of the discrete nonlinear Schrödinger equation with disorder". *Eur. Phys. J.: Spec. Top.* **225**, 1103, 2016.

[103] Ch. Skokos, E. Gerlach, J. D. Bodyfelt, G. Papamikos, and S. Eggl. "High order three part split symplectic integrators: Efficient techniques for the long time simulation of the disordered discrete nonlinear Schrödinger equation". *Phys. Lett. A.* **378**, 1809, 2014.

[104] J. Laskar and P. Robutel. "High order symplectic integrators for perturbed Hamiltonian systems". *Celest. Mech. Dyn. Astron.* **80**, 39, 2001.

[105] A. Farrés, J. Laskar, S. Blanes, F. Casas, J. Makazaga, and A. Murua. "High precision symplectic integrators for the Solar System". *Celest. Mech. Dyn. Astron.* **116**, 141, 2013.

[106] URL: https://www.chpc.ac.za/.

[107] W. S. Cleveland. "Robust locally weighted regression and smoothing scatterplots". *JASA* **74**, 829, 1979.

[108] S. L. Shepelyanskyd. "Delocalization of quantum chaos by weak nonlinearity". *Phys. Rev. Lett.* **70**, 1787, 1993.

[109] S. Flach. "Spreading of waves in nonlinear disordered media". *Chem. Phys.* **375**, 548, 2010.

[110] E. H. Lieb. "Two theorems on the Hubbard model". *Phys. Rev. Lett.* **62**, 1201, 1989.

[111] F. V. Kusmartsev and E. I. Rashba. "Self-trapping of excitons and lattice defect production in solid rare gases". *Czechoslov. J. Phys.* **32**, 54, 1982.

[112] M. I. Molina. "Transport of localized and extended excitations in a nonlinear Anderson model". *Phys. Rev. B.* **58**, 12547, 1998.

[113] M. I. Molina and G. P. Tsironis. "Nonlinear impurities in a linear chain". *Phys. Rev. B.* **47**, 15330, 1993.

[114] M. Hillebrand, S. Zimper, A. Ngapasare, M. Katsanikas, S. Wiggins, and Ch. Skokos. "Quantifying chaos using Lagrangian descriptors". *Chaos* **32**, 123122, 2022.

[115] M. Hermanns. *Parallel programming in Fortran 95 Using OpenMP*. OpenMP.org, 2002.

[116] S. Blanes, F. Casas, A. Farrés, J. Laskar, J. Makazaga, and A. Murua. "New families of symplectic splitting methods for numerical integration in dynamical astronomy". *Appl. Numer. Math.* **68**, 58, 2013.

[117] M. Hillebrand, G. Kalosakas, A. Schwellnus, and Ch. Skokos. "Heterogeneity and chaos in the Peyrard-Bishop-Dauxois DNA model". *Phys. Rev. E.* **99**, 022213, 2019.

[118] A. Ngapasare, G. Theocharis, O. Richoux, Ch. Skokos, and V. Achilleos. "Chaos and Anderson localization in disordered classical chains: Hertzian versus Fermi-Pasta-Ulam-Tsingou models". *Phys. Rev. E.* **99**, 032211, 2019.

[119] Y. Kati, X. Yu, and S. Flach. "Density resolved wave packet spreading in disordered Gross-Pitaevskii lattices". *SciPost Phys.* **3**, 006, 2020.

[120] D. Leykam, S. Flach, O. Bahat-Treidel, and A. S. Desyatnikov. "Flat band states: Disorder and nonlinearity". *Phys. Rev. B.* **88**, 224203, 2013.